Czech Technical University in Prague

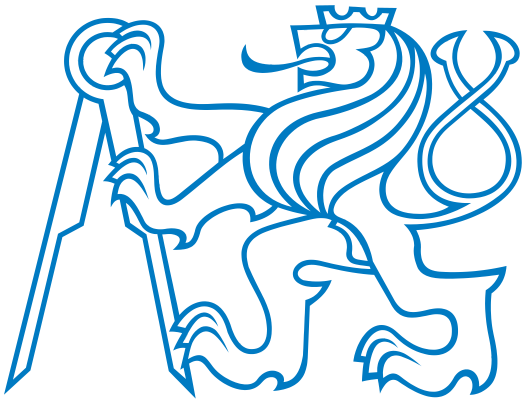

Dissertation Thesis

Czech Technical University in Prague
Faculty of Nuclear Sciences and Physical Engineering
Department of Physics

**Antonín Krása**

# Neutron Emission in Spallation Reactions of 0.7 – 2.0 GeV Protons on Thick, Lead Target Surrounded by Uranium Blanket

Dissertation Thesis

Prague, 2008

# Declaration

I confirm that this dissertation thesis was done in the internal and combined forms of postgradual study at the Department of Physics at the Faculty of Nuclear Sciences and Physical Engineering at Czech Technical University in Prague. This thesis is the result of my own work unless explicit references are made to the work of others; it has not been submitted for another qualification to this or any other university.

Aspirant: **Mgr. Antonín Krása**

Postgradual study program: Application of Natural Sciences

Study field: Nuclear Engineering

Supervisor: **RNDr. Vladimír Wagner, CSc.**
Affiliation: Department of Nuclear Spectroscopy
Nuclear Physics Institute
Academy of Sciences of the Czech Republic
public research institution
250 68 Řež near Prague

# Acknowledgments

My special thanks go to:

- my excellent supervisor RNDr. Vladimír Wagner, CSc., for his patience and permanent support of my work;
- the head of the Department of Nuclear Spectroscopy at NPI Řež RNDr. Andrej Kugler, CSc., for his confidence, valuable suggestions and new visual angles on the topic;
- my colleague Mitja Majerle, graduated physicist, for his huge work on simulations and sharing his knowledge;
- my colleagues Mgr. Filip Křížek, ing. Ondřej Svoboda, ing. Karel Katovský, ing. Marek Fikrle, ing. Orlin Jordanov for inspiring comments and hot discussions;
- Mgr. Vladimír Henzl, PhD., and Mgr. Daniela Henzlová, PhD., for their brilliant ideas;
- IAESTE students Ines Hartwig, Peter Rechberger, Gaël de Cargouet for fair cooperation and lot of questions that made me to think about my work and words again and helped me to better understanding.

I am grateful to all of them and to all colleagues of the E+T collaboration for careful cooperation during experiments (irradiations or measurements), sharing their geniuses and attainments.

My deep thanks belong also to Jaroslav Frána, CSc., for the possibility of using the $\gamma$-spectrometer for long-lived isotopes measurements and his DEIMOS code for spectra analysis; the directorate of the LHE JINR for the possibility of using the Nuclotron accelerator; METACentrum for offering computers for the calculations.

Last but not least I would like to thank my wife for her pure, unconditional love.

This work was carried out under support of the Grant Agency of the Czech Republic (grant No. 202/03/H043) and under support of the Grant Agency of the Academy of Sciences of the Czech Republic (grant No. K2067107).

# Abstract

"Energy plus Transmutation" is an international project for the study of spallation reactions, neutron production and transport, and the transmutation of fission products and higher actinides by spallation neutrons. The "Energy plus Transmutation" setup consists of a thick, lead target with a subcritical, natural uranium blanket surrounded by polyethylene shielding. A detailed study of the spatial distribution of the neutron field produced in four separate irradiations with protons with kinetic energies of 0.7, 1.0, 1.5, and 2.0 GeV is presented. The neutron field was measured by means of activation detectors.

The experimental results are compared with Monte-Carlo calculations, performed with the MCNPX 2.6.C code. The simulated quantities are spatial distributions and energy spectra of neutrons and protons produced in the setup, yields of radioactive isotopes produced in activation detectors, and the integral numbers of neutrons produced in the whole setup per one incident proton. The theoretical description by MCNPX agrees qualitatively well with the experimental results; the exception is in the case of bigger proton beam energies, where the high-energy neutron production is underestimated for backward angles.



**Key words:** spallation reactions, neutron production and transport, neutron activation analysis method, $\gamma$-spectroscopy, the Energy plus Transmutation setup, the MCNPX code

# Abstrakt

"Energie plus Transmutace" je mezinárodní projekt, který se zabývá studiem tříštivých reakcí, produkce neutronů a jejich transportu, dále transmutace štěpných produktů a vyšších aktinidů. Experimentální sestava se skládá z tlustého olověného terče s podkritickou obálkou z přírodního uranu. Jako stínění je použit polyetylén. V této disertační práci jsou popsány výsledky měření neutronového pole produkovaného při ozařování sestavy protonovým svazkem o energiích 0,7 – 2,0 GeV. Neutronové pole bylo měřeno pomocí aktivačních detektorů.

Experimentální výsledky byly porovnány se simulacemi Monte Carlo provedenými programem MCNPX verze 2.6.C. Simulovanými veličinami jsou prostorová a energetická rozložení neutronů a protonů, dále výtežky radioizotopů produkovaných v aktivačních vzorcích a jako globální charakteristika celkový počet neutronů produkovaných v sestavě. Výsledky simulací jsou v dobré kvalitativní shodě s experimentem, MCNPX pouze podceňuje produkci vysokoenergetických neutronů do zpětných úhlů v případě experimentů s vyššími energiemi protonového svazku.

**Klíčová slova:** spalační reakce, produkce a transport neutronů, metoda neutronové aktivační analýzy, spektroskopie záření gamma, sestava Energie plus transmutace, program MCNPX

# Contents

# Introduction

Transmutations of long-lived actinides and fission products from nuclear waste, plutonium from nuclear weapons, or thorium (as an energy source) are being investigated with increasing interest in the last two decades. Different concepts of transmutation involve also the Accelerator Driven Systems (ADS) [1, 2] based on a subcritical nuclear reactor driven by an external spallation neutron source (chapter 1).

This work is a part of a complex research of ADS carried out within the frame of the "Energy plus Transmutation" project that concerns the study of spallation reactions, neutron production and transport, and transmutation of fission products and actinides by spallation neutrons. This thesis describes measurement of the high-energy neutron field produced in the experiments performed on the proton beams with kinetic energies of 0.7, 1.0, 1.5, and 2.0 GeV. While investigations of high-energy neutron domain ($E_{\mathrm{n}} > 10.5$ MeV) were not of high interest in the past, because of its minor importance for classical light-water nuclear reactors, they will be important for ADS and spallation neutron sources as well as for radio-isotope protection issues in future high-energy facilities, or radiation damage in space. Reliable predictions of the relevant physics processes strongly depend on the accuracy of available nuclear data.

The experiments have been performed using the Nuclotron accelerator at the Veksler and Baldin Laboratory of High Energies at the Joint Institute for Nuclear Research (JINR) in Dubna, Russian Federation (chapter 3). Relativistic protons interacting with a thick, lead target induced spallation reactions and intense neutron fluxes were created. Emitted neutrons were multiplied by fission inside the blanket (a competitive process that can occur in the blanket is neutron capture). The spatial and energetic distributions of the produced neutron field were measured by means of activation reactions in mono-isotopic activation samples. Their activities were measured with the HPGe spectrometers at the Dzhelepov Laboratory of Nuclear Problems at JINR Dubna (of short-lived radioisotopes) and at the Department of Nuclear Spectroscopy at the Nuclear Physics Institute of the Academy of

Sciences of the Czech Republic (NPI AS CR PRI) in Řež (of long-lived radioisotopes). The yields of the radioactive nuclei produced in these samples were determined with the respect to all necessary spectroscopic corrections (chapter 4).

Experimental results (chapter 5) were compared with MCNPX simulations (chapter 6) with the aim to test its applicability to describe physics processes occurring in such a setup, the accuracy of the model descriptions and the cross-section libraries included in MCNPX and to check the differences between various MCNPX configurations.

# Chapter 1

# Accelerator Driven Systems (ADS)

## 1.1 Transmutation

Nuclear **transmutation**[1] is a process in which the structure of an atomic nucleus changes. When changing the number of neutrons, the nucleus' physics properties change (e.g., half-life, activity, radiation energy), in the case of the change in the number of protons, the nucleus obtains also different chemical properties (e.g., reaction rate, chemical coupling). Apparently, appropriately induced transmutations could be used to decrease the half-lives of long-lived radioisotopes (**Table 1.1**) included in the high level waste that is being produced during the nuclear fuel burnup in nuclear reactors. Radioactive nuclei are being produced during the operation of nuclear reactors in two ways.

- **Fission products** are being generated by the fission of $^{235}$U or $^{239}$Pu in classical or fast nuclear reactors. Fission products are mostly slightly above the line of $\beta$-stability. To transmute them to stable nuclides, they should capture one or more neutrons and then undergo $\beta$-decay.
- **Higher actinides** or transuranic elements, representing about 1% of spent fuel, are being generated by the neutron capture within nuclei of $^{235}$U, $^{238}$U, or $^{239}$Pu and their resultant $\beta$-decays. To transmute higher actinides to stable nuclides, they should undergo neutron capture and consecutive fission, which is a process that produces energy and makes the transmutation attractive from the point of view of energetics.

[1] Historical note: In 1919, E. Rutherford [3], as the first, demonstrated transmutation on example of $^{14}\mathrm{N} + \alpha \rightarrow {}^{17}\mathrm{O}$. In 1932, J. D. Cockroft and E. T. S. Walton [4] demonstrated the first accelerator-driven transmutation. They bombarded Li-target with 125-500 keV protons (from linear accelerator) and "transmuted" Li-nucleus into two $\alpha$-particles.

Table 1.1: Fission products and higher actinides contained in nuclear burned up fuel, which are expected for transmutation. The amounts are annual waste production (after ten years of decay) from a typical commercial reactor (3 GW power, with fuel burned to 33 GWdays per ton with the annual removal of 33 metric tons uranium equivalent of spent fuel per year) [6]).

| Fission product | Half-life [years] | Amount [$10^{23}$ atoms] | Activity [Bq] |
|---|---|---|---|
| $^{79}$Se | $1 \times 10^6$ | 13 | $3 \times 10^{10}$ |
| $^{90}$Sr | 30 | 900 | $7 \times 10^{16}$ |
| $^{93}$Zr | $2 \times 10^6$ | 1500 | $2 \times 10^{12}$ |
| $^{99}$Tc | $2 \times 10^5$ | 1500 | $2 \times 10^{13}$ |
| $^{126}$Sn | $1 \times 10^5$ | 46 | $1 \times 10^{12}$ |
| $^{129}$I | $2 \times 10^7$ | 270 | $4 \times 10^{10}$ |
| $^{137}$Cs | 30 | 1400 | $1 \times 10^{17}$ |
| Higher actinide | Half-life [years] | Amount [$10^{23}$ atoms] | Activity [Bq] |
| $^{237}$Np | $2 \times 10^6$ | 366 | $4 \times 10^{11}$ |
| $^{241}$Am | 400 | 413 | $2 \times 10^{15}$ |
| $^{243}$Am | $7 \times 10^3$ | 73 | $2 \times 10^{13}$ |
| $^{244}$Cm | 20 | 13 | $2 \times 10^{15}$ |
| $^{238}$Pu | 90 | 113 | $3 \times 10^{15}$ |
| $^{239}$Pu | $2 \times 10^4$ | 4160 | $4 \times 10^{14}$ |
| $^{240}$Pu | $7 \times 10^3$ | 1920 | $6 \times 10^{14}$ |
| $^{241}$Pu | 10 | 640 | $1 \times 10^{17}$ |
| $^{242}$Pu | $4 \times 10^5$ | 390 | $2 \times 10^{12}$ |

As follows from the previous paragraph, we use the concept of "transmutation" in the meaning of a conversion of radioisotopes with long half-lives to short-lived or stable ones. The transmutation can be effectively done by means of the placement into an intensive neutron field[2]. Even large neutron flux densities in a classical nuclear reactor (typically $\phi \sim 10^{14}$ neutrons$\cdot$cm$^{-2}\cdot$s$^{-1}$) are not efficient enough for transmutation purposes. Required flux for ADS should be at least two orders bigger [6] to enable conversion of nuclei with low absorption cross-sections and a few-step capture process in the case of higher actinides. To meet such requirements, the spallation reactions on a thick target can be used as an intensive source of neutrons[3]. Spallation neutron sources are already being used for material research and industry [10] or in medicine for radiotherapy [11].

[2]The use of photons or charged particles is being examined as well, but the use of neutrons appears the most practical [5].

[3]Other possibilities to produce intensive neutron fluxes for ADS purposes are for example: the electron induced neutron production (via bremsstrahlung photons) [7, 8] or the fusion of deuterium and tritium catalyzed by a negative muon [9].

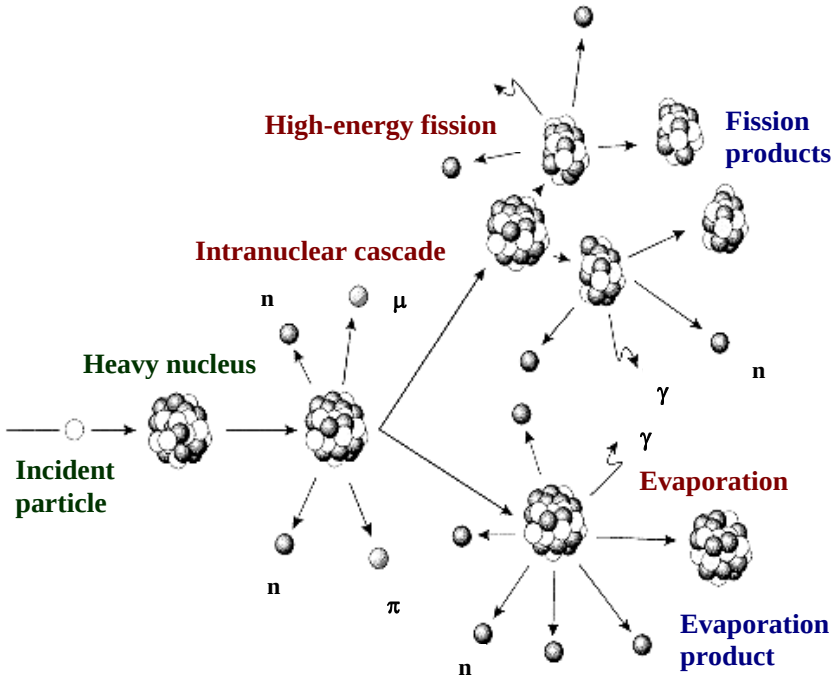


Figure 1.1: The scheme of a spallation reaction (according to [17]).

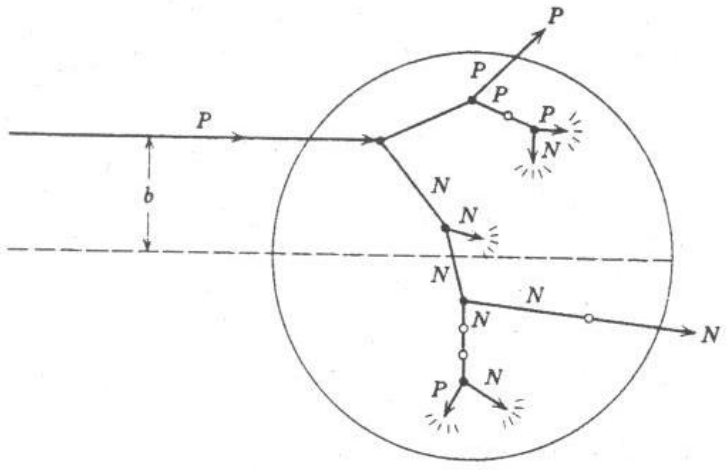


Figure 1.2: The scheme of an intra-nuclear cascade generated by a proton in a heavy nucleus with the impact parameter $b$. The solid circles represent the positions of collisions, the open circles represent the positions forbidden by the Pauli exclusion principle. The short arrows indicate "captured" nucleons, which contribute to the excitation of the nucleus (taken from [18]).

## 1.2 Spallation

**The spallation reaction**[4] is a process in which a light projectile (proton, neutron, or light nucleus) with kinetic energy from several hundreds of MeV to several GeV interacts with a heavy nucleus (e.g., lead) and causes emission of a large number of hadrons (mostly neutrons) or fragments. Spallation has three stages [19]: intra-nuclear cascade, pre-equilibrium stage, and evaporation or fission, see **Fig. 1.1**.

The **intra-nuclear cascade (INC)** is a fast direct stage ($\sim 10^{-22}$ s), see **Fig. 1.2**. As the de Broglie wavelength of the $\sim$ 1 GeV projectile is $\sim$ 1 fm, it interacts with individual nucleons in the target nucleus (instead of creating a compound nucleus). The projectile shares its kinetic energy with target nucleons by elastic collisions and a cascade of nucleon-nucleon collisions proceeds.

At low projectile energies ($\sim$ 100 MeV), all interactions occur just between nucleons and the process is called nucleon cascade. Gradually, with growing incident particle energy, the threshold energies for particle production in nucleon-nucleon collisions are being exceeded. Initially, pions come up (at energies of about hundreds of MeV), at bigger energies ($\sim 2 - 10$ GeV) heavier hadrons are being produced. They can also participate in the intra-nuclear cascade and interact between each other, what is called hadron cascade. Particles that obtained energy high enough to escape from the nucleus are being emitted mainly *in the direction of the incident particle*. The rest of the energy is equally distributed among nucleons in the nucleus which is left in a highly excited state.

The intra-nuclear cascade is not sharply separated from the equilibrium decay. In a pre-compound stage ($< 10^{-18}$ s), the **pre-equilibrium emission** can happen[5]. In the course of this stage, fast particles or fragments may be emitted after each interaction between the incident or other cascade particle and a nucleon inside the nucleus. The energies of pre-equilibrium particles are greater than energies of particles emitted during the equilibrium decay.

Finally, the equilibrium stage comes up. Energy is equally distributed throughout the nucleus that is in a highly excited state with small angular

[4]Historical note: The observations of particle cascades in cosmic rays interactions have been done already in 1930's [12]. (The thermal neutron flux density induced by cosmic-ray-protons is $\sim 10^{-4} - 10^{-3}$ neutrons cm$^{-2}$ s$^{-1}$ at the Earth's surface [13].) The first accelerator-driven spallation reactions have been discovered by B. B. Cunningham at Berkeley [14] in 1947. Theoretical description was given soon after by Serber [15]. W. H. Sullivan and G. T. Seaborg made up the term "spallation" in the same year [16].

[5]For bigger beam energies and especially in heavy-ion collisions [20], multi-fragmentation (production of many fragments of relatively small charges) or breakup into individual particles are possible as well.

momentum. The nucleus loses its energy by **evaporation** of neutrons or light charged fragments (e.g., deuterons, $\alpha$-particles) with energies up to $\approx 40$ MeV (which is the nuclear potential well depth [21]). The particles are emitted *isotropically* (in contrast to INC, see **Fig. 1.3**).

Competitive process to evaporation is **fission** (into two fragments similar in proton number). Fission products also undergo evaporation (depending on their excitation energy). When the nucleus does not have energy enough to emit neutrons (its excitation energy becomes smaller than the binding energy), it deexcites by $\beta$-and $\gamma$-transitions.

Two aspects of major importance in spallation reactions are residual nuclei (or spallation products) and emitted neutrons (or spallation neutrons).

### 1.2.1 Spallation products

The spallation products spread out in two regions of the chart of the nuclides, see **Fig. 1.4**. The upper right part corresponds to the heavy proton-rich residues produced from evaporation (spallation-evaporation products), the central part corresponds to the medium-mass residues produced from fission (spallation-fission products).

The spallation products can be measured using two methods: direct [23, 24] or inverse kinematics [25].

In **direct kinematics**, a relativistic light projectile hits a heavy target. The spallation products, which stop in the target, can be detected using $\gamma$-spectroscopy and mass spectrometry. This method has the possibility to measure the yields of the meta-stable states of residual nuclei, it can use radioactive targets, and it consumes less beam time. On the other hand, it is impossible to measure the yields of very long-lived, stable, and very short-lived nuclei, and the off-line yields measurements are more time consuming.

In the case of **inverse kinematics**, a relativistic heavy nucleus hit a light target. The spallation products leave the target in forward direction and using the appropriate technique (e.g., the magnetic spectrometer FRS (FRagment Separator) [26] equipped with an energy degrader, two position scintillator detectors, multiple-sampling ionisation chambers, multiwire-proportional counters) can be identified immediately in flight.

### 1.2.2 Spallation neutrons

The neutrons produced in spallation reactions can be characterized by their energy and spatial distributions and multiplicity.

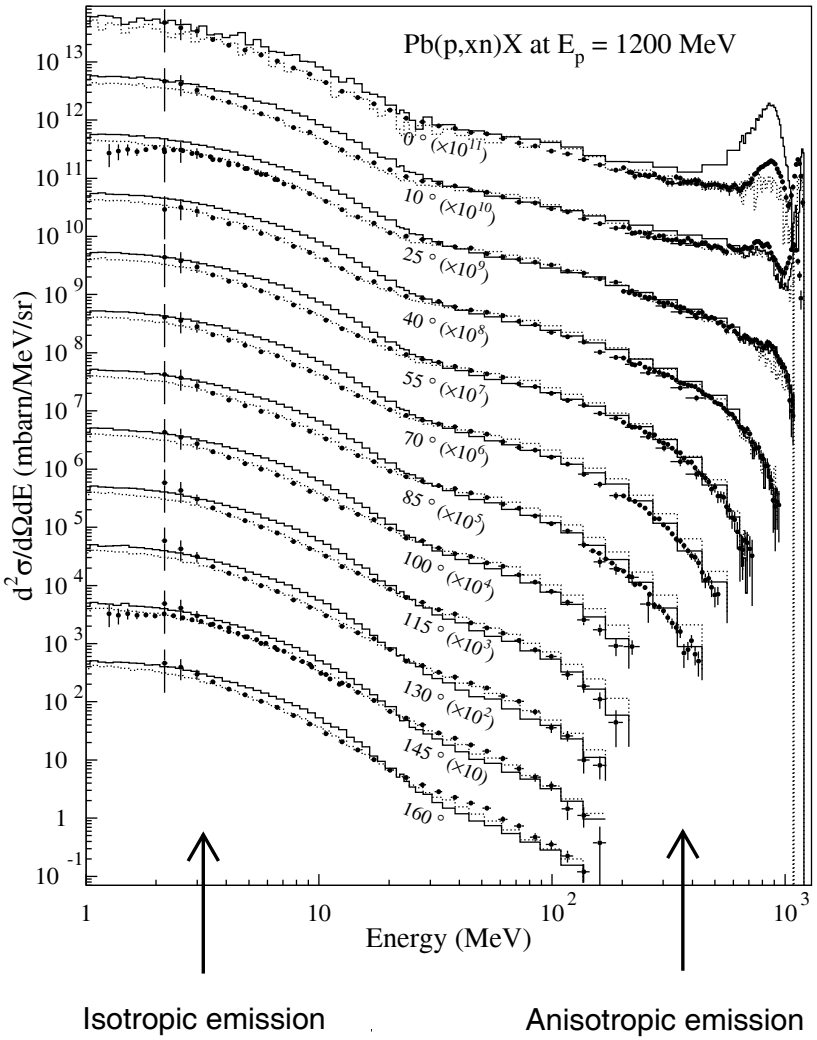


Figure 1.3: Neutron production double-differential cross-sections in reactions of 1.2 GeV protons on a thin Pb target (thickness of 2 cm). Each successive curve (from 160 °) is scaled by a factor of 10 with decreasing angle. Points are experimental values (measured at the SATURNE accelerator), histograms represent Bertini INC calculations (full lines) or INCL calculations (dotted lines). In order to obtain enough statistics, the emission angle in simulations was taken as ±2.5 °, while the experimental aperture was ±0.43 ° for $E_{\mathrm{n}} > 200$ MeV and between ±0.71 ° and ±0.81 ° for lower neutron energies (according to [22]).

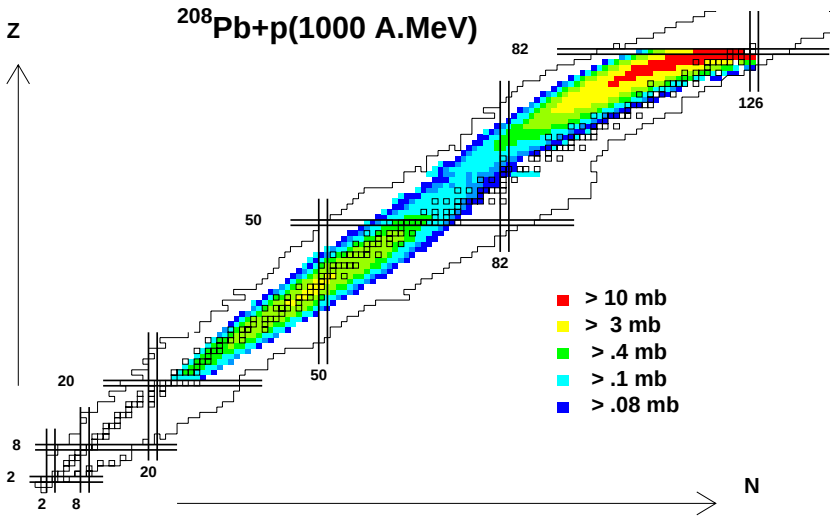


Figure 1.4: The cross-sections for residual nuclei production in the $^{208}$Pb (1 $A$GeV) + p reaction. The distribution of the isotopes produced is shown on a chart of the nuclides, where black open squares represent stable nuclei, the magic proton and neutron numbers are indicated. Spallation-evaporation products and spallation-fission products are separated by a minimum of cross-sections at $Z = 58 \pm 3$. About 900 isotopes were identified, the total reaction cross-section amounts to $\sigma_{\rm tot} = (1.87 \pm 0.23)$ b (according to [25, 27]).

**Neutron spectra**[6] can be decomposed into four components, each of which represents a single physics process leading to neutron production [28] (see **Fig. 1.5**):

$$\frac{\mathrm{d}^2\sigma}{\mathrm{d}\Omega \mathrm{d}E} = A_1 \exp\Big(-\frac{E}{E_1}\Big) + \sum_{i=2}^{3} A_i \exp\Big(-\frac{E}{E_i}\Big) + \\ + A_{\rm el} \exp\Big[-\Big(\frac{E-E_{\rm el}}{W_{\rm el}}\Big)^2\Big] + A_{\rm inel} \exp\Big[-\Big(\frac{E-E_{\rm inel}}{W_{\rm inel}}\Big)^2\Big], \quad (1.1)$$

where the evaporation component, cascade component, quasi-elastic component (correspond to peripheral collisions when neutron is ejected after one elastic collision), and quasi-inelastic component (the same as the latter, but leaving the partner nucleon excited to the $\Delta$-resonance) stand in this

[6]The double differential cross-section $\frac{\mathrm{d}^2\sigma}{\mathrm{d}\Omega \mathrm{d}E}$ is defined as the number of neutrons that are scattered into the solid angle interval ($\Omega$, $\Omega + d\Omega$) and into the energy interval ($E$, $E + dE$). It is normalized to $d\Omega$, $dE$.

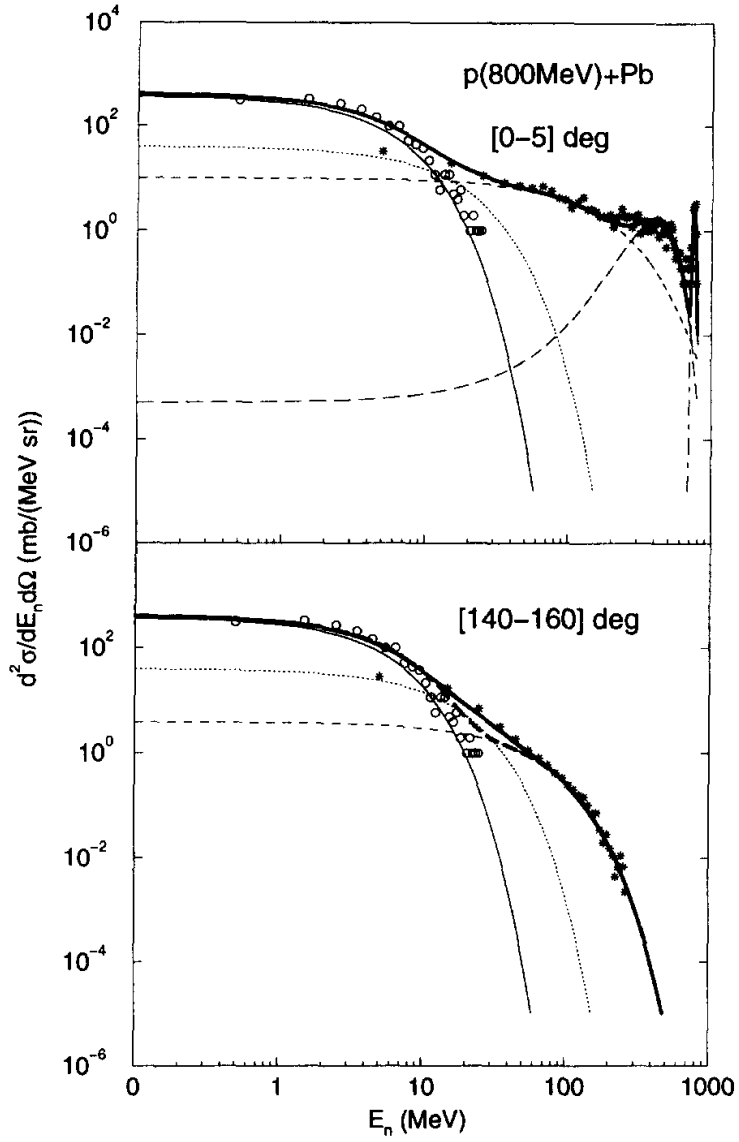


Figure 1.5: Neutron production double-differential cross-section in reactions of 0.8 GeV protons on a thin Pb-target. The upper part is averaged over angles $0-5^{o}$, lower part is averaged over angles $140-160^{o}$. The symbols give the results of INCL+Dresner simulation: stars stand for cascade component, open circles for evaporation. The thick curve represents the fit of the results by formula (1.1), thin curves represent various components: full curve – evaporation, dotted and small-dashed curve – cascade, long-dashed curve – quasi-inelastic, and dot-and-dashed curve – quasi-elastic components. The thick dashed curve (in the lower part) represents the fit when only one exponential in the cascade component of formula (1.1) is leaved in (taken from [28]).

sequence. Of course, the quasi-elastic and quasi-inelastic components are inconspicuous at backward angles (see the lower part of **Fig. 1.5**).

The quantity $E_{\rm el}$ ($E_{\rm inel}$) is the average energy of the neutrons that are ejected after a single (in)elastic collision induced by the incident proton. The quantity $E_{\rm inel}(0^{\rm o})$ differs from the incident energy because of the Fermi motion of the struck nucleon (and the influence of the Pauli blocking, which may inhibit the collision). The quantity $W_{\rm el}$ reflects the "width" of this Fermi motion (with the influence of the Pauli blocking). The width $W_{\rm inel}$ is dominated by the width of the produced $\Delta$-particle, which is much larger than the width of the Fermi sea. The physics meaning of the width parameters $E_{1,2,3}$ is not obvious. The parameters $E_i$ and amplitudes $A_i$ depend on the target mass (in the case of U-target, it is necessary to take into account also extra neutrons emitted by the excited fission products).

The fact that the cascade component cannot be fitted by one exponential function (which is indicated in the lower part of **Fig. 1.5**) reflects the process complexity. On the other hand, it can be perceived as a surprise that the multiple collision part of the cascade could be simply described by two exponentials.

The experimental results of energy and spatial distributions of the neutrons produced in spallation reactions show the same trends, see **Fig. 1.3**. The quasi-elastic and quasi-inelastic contributions disappear above 25 °. Neutrons with energies from 3 to 400 MeV have been detected by the time-of-flight technique (the time difference between the incident proton, tagged by a plastic scintillator, and a signal from a neutron-sensitive liquid scintillator) [29]. Neutrons with energies bigger than 200 MeV (where the TOF resolution is poor) have been detected using (n,p)-scattering on a liquid hydrogen converter and reconstruction of the proton trajectory in a magnetic spectrometer [30]. The angular distribution of neutrons have been measured by an additional collimation system.

It is also interesting to compare the neutron spectra when different beam projectiles are being used (at the same energy per nucleon), because the cascade initiated by two nucleons are not additive [28]. The yields of high-energy neutrons ($E_{\rm n} > 500$ MeV for $E_{\rm beam} = 800$ $A$MeV) are significantly larger in deuteron-induced reactions than proton-induced ones, see **Fig. 1.6**. This is because of the stripping process, which involves a strong interaction between deuteron and target nucleus and dissociation of deuteron, when only one of the two particles making up the deuteron interacts directly with the target nucleus [31] (contrary to the deuteron breakup – dissociation of deuteron due to the Coulomb field of a target nucleus [32]). Neutrons with lower energies are slightly less abundant in deuteron-induced reactions than twice in proton-induced ones.

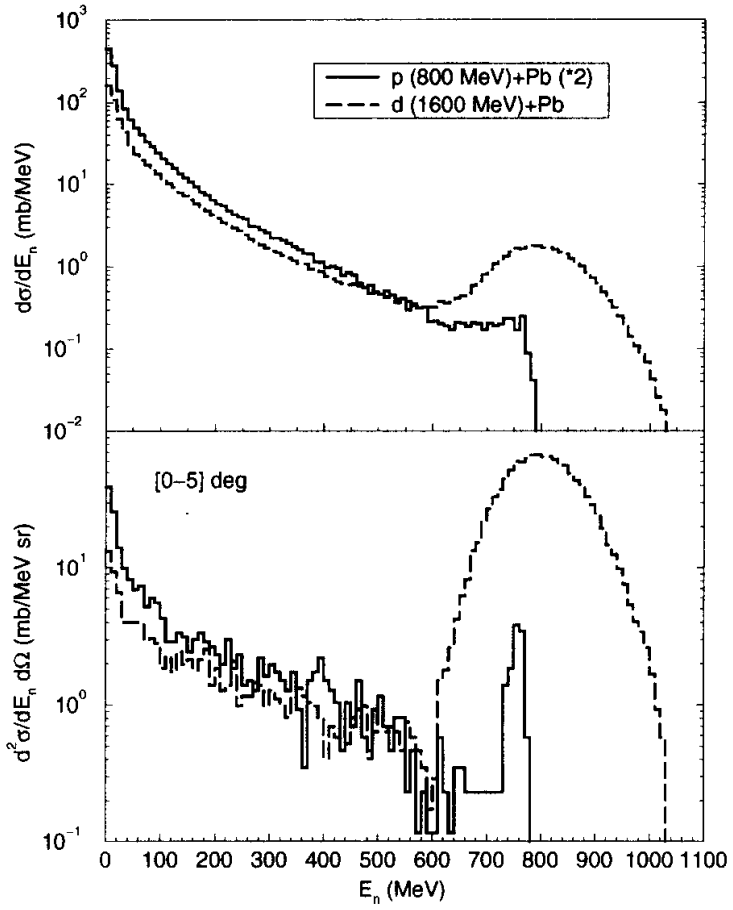


Figure 1.6: Neutron production double-differential cross-section in reactions of 0.8 GeV protons (full line; multiplied by a factor of 2) and 1.6 GeV deuterons (dashed line) on a thin Pb-target. The upper part is integrated over all angles, the lower part is averaged over angles $0 - 5^{\mathrm{o}}$ (the contribution of the stripping process is even more remarkable for forward angles). Results of INCL+Dresner simulation (taken from [28]).

The integral number of neutrons produced per one incident particle is called **multiplicity**. Neutron multiplicity as a function of the beam energy and target material shows roughly linear dependence on the target mass number (in the range $12 < A < 238$) and slow increase with incident proton energy (in the range $0.2 < E_{\mathrm{p}} < 2$ GeV). The semi-empirical formula [28]:

$$M_{\mathrm{n}}(E_{\mathrm{p}}[\mathrm{GeV}], A) = (0.0803 + 0.0336 \ln(E_{\mathrm{p}}))A \qquad (1.2)$$

gives better than 10% accuracy for $A > 40$, see **Fig. 1.7**.

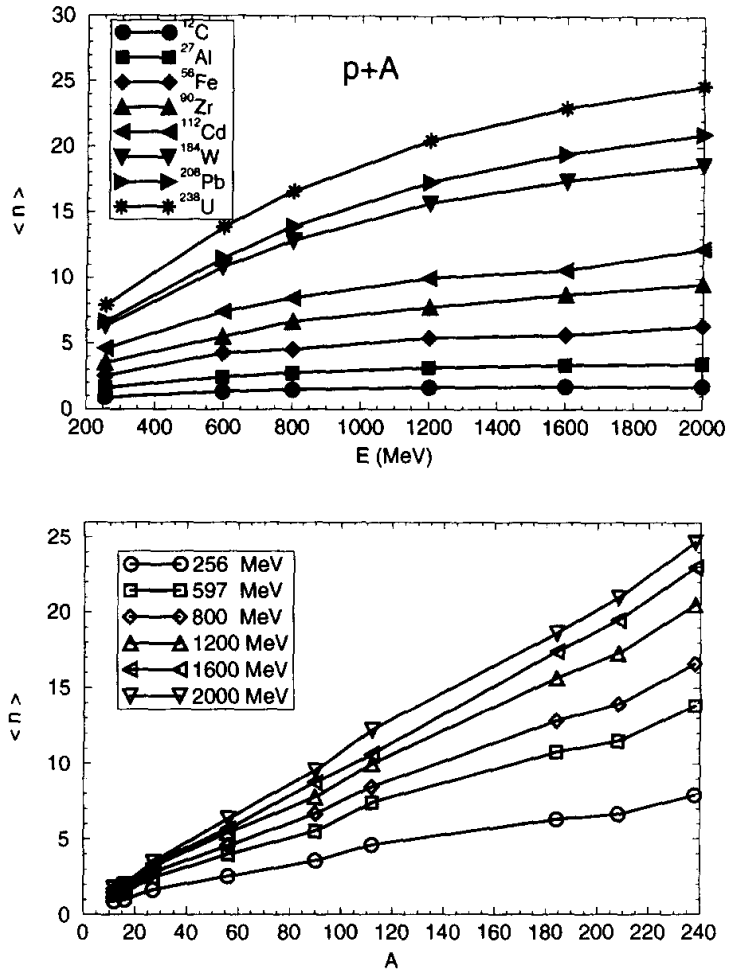


Figure 1.7: Neutron multiplicity per incident proton as a function of beam energy (upper part) and (thin) target material (lower part). Results of INCL+Dresner simulation (taken from [28]).

It is also interesting to compare the share of cascade and evaporation neutron components. Broadly speaking, the evaporation contribution is more important than the cascade one (by a factor of 2 for $E_p > 1$ GeV; its importance is reduced at lower energies) [28]. The cascade component is roughly a linear function of target mass number and only weakly depend on proton energy, see upper part of **Fig. 1.8**. The evaporation component is also almost a linear function of target mass number but it depends much more on proton energy, see lower part of **Fig. 1.8**. This is connected with the excitation energy left in the target nucleus after INC, which increases (slightly less than linearly) with the incident energy [28], see **Fig. 1.9**.

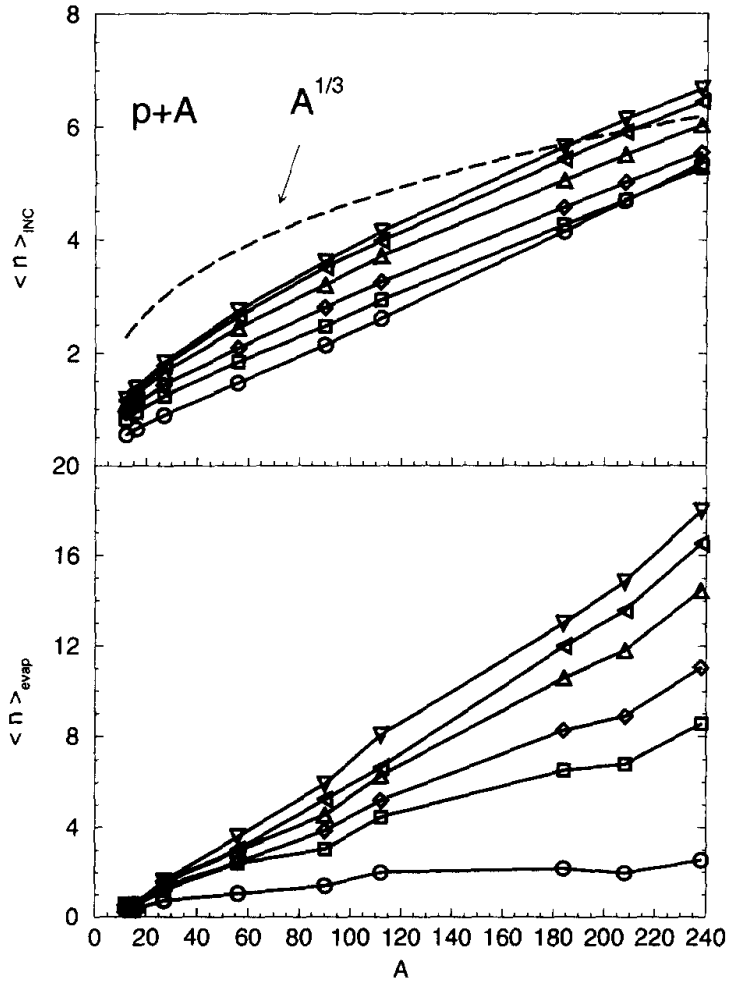


Figure 1.8: Neutron multiplicity as a function of (thin) target material. Split into cascade (upper part) and evaporation components (lower part). Open symbols refer to the values of the incident energy, with the same convention as in the previous figure. Results of INCL+Dresner simulation (taken from [28]).

### 1.2.3 Spallation reactions on thick targets

In the case of a thick target, high-energy particles escaping from the nucleus in the course of INC can induce further spallation reactions and generate **inter-nuclear cascade**. It relates mainly to neutrons because they do not lose their energy by ionization losses. Thus, among all emitted particles, they penetrate deepest into the target material. For some target materials, low-energy spallation neutrons (i.e., low-energy cascade plus evaporation neutrons) can enlarge neutron production by **(n,*x*n)-reactions**.

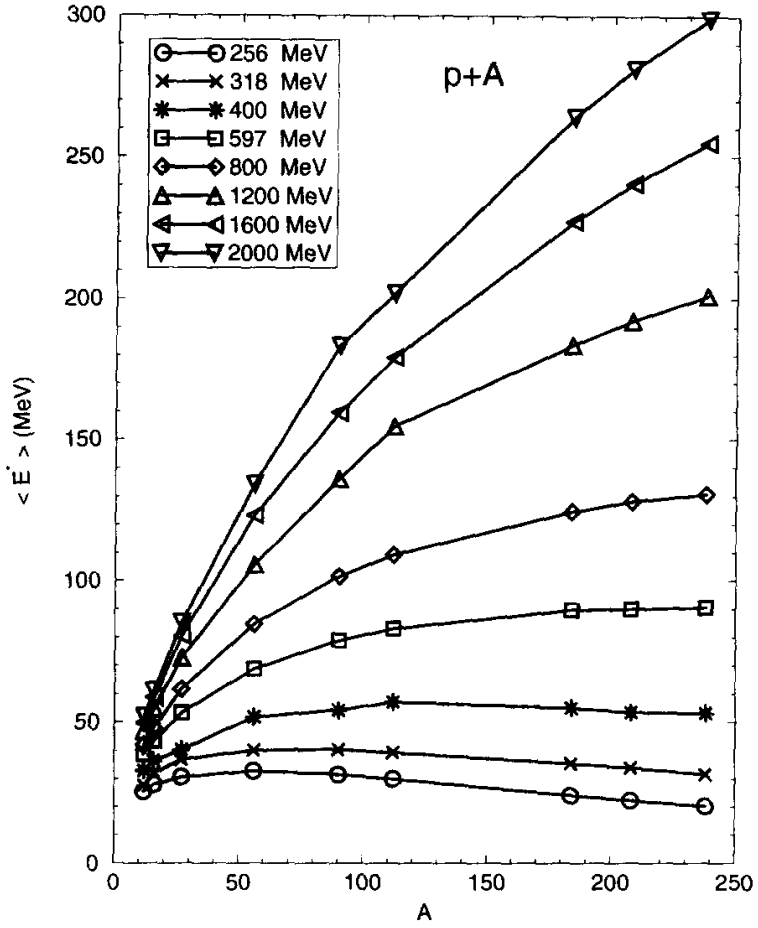


Figure 1.9: The excitation energy left in the target nucleus after INC in proton-induced reactions at several incident energies as a function of target mass (taken from [28]).

Globally, the incident proton induces the production of a large amount of neutrons (**Fig. 1.13**) with wide energy spectra (**Fig. 2.1**). These neutrons can be used for transmutation of relevant nuclei. The neutron multiplicity for thick targets depends on the projectile-target combination.

Besides protons, other light nuclei or hadrons beams have been investigated. The deuteron-induced spallation reactions on thick targets were explored theoretically [33] using the LAHET+MCNP codes. Neutron production in deuteron-induced reactions is bigger than in proton-induced ones by a factor of 1.3-2.5 for light targets and small beam energies, but it is more or less the same (within 10%) for heavy targets and bigger beam energies (**Fig. 1.10**), which are considered for ADS purposes.

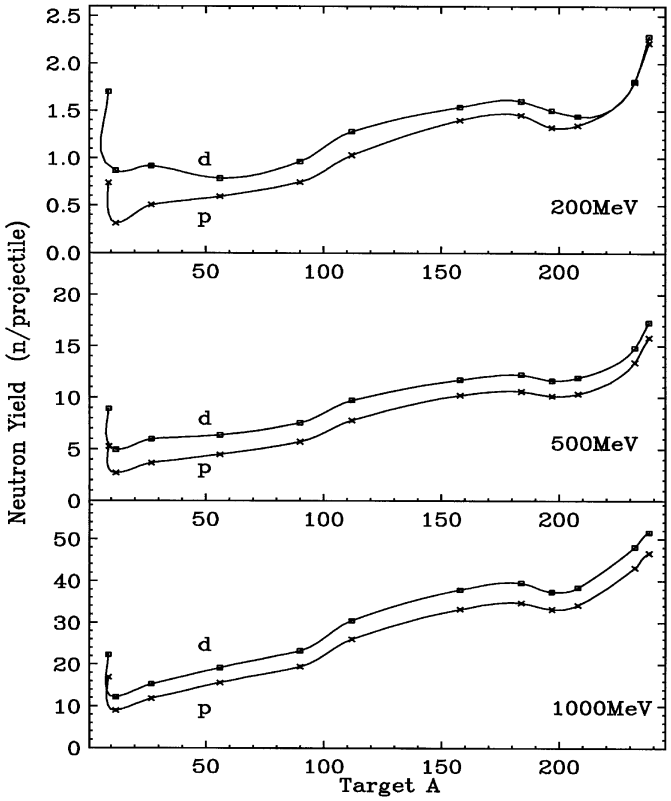


Figure 1.10: Neutron multiplicity as a function of target material for 200, 500, 1000 MeV protons and deuterons. A thick target (cylinder with equal length and diameter given by two ranges for protons depending on incident energy) was used for LAHET+MCNP simulation (taken from [33]).

A set of experiments with 3.65 *A*GeV light nuclei beams was carried out at JINR Dubna [34] in 1980's with conclusion that the number of neutrons produced per one incident proton as well as the power consumption for neutron generation are slightly preferable for light nuclei ($^2$H, $^4$He) to protons, while neutron production for heavier projectiles ($^{12}$C) decrease because of higher Coulomb potential. But this is valid for beam energies $\gtrsim$ 3 *A*GeV only; the ionization losses of ions increase significantly for beam energies around 1 GeV, which is expected optimal energy region for future ADS.

Recent experiments carried out at CERN [35] show that the proton-, antiproton-, charged pion-, positive kaon-, and deuteron-induced reactions in the energy range of 1-6 GeV result in very similar neutron multiplicities, see **Fig. 1.11**. So, the neutron multiplicity is relatively independent of the incident hadron species.

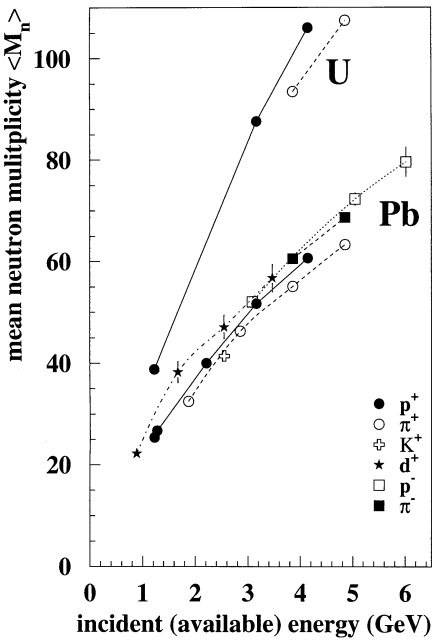


Figure 1.11: Neutron multiplicity as a function of beam energy (for different beam particles) on thick lead (length of 35 cm, diamater of 15 cm) and uranium (length of 40 cm, diamater of 8 cm) targets. The curves connect the data points (taken from [35]).

Regarding target parameters, its material and size are those which determine the neutron multiplicity. In principle, the heavier target nucleus the larger amount of neutrons is being produced. The gain factor between heavy and light targets is around a factor of five [27], however, the radiotoxicity induced in the spallation target could be significantly reduced when using lighter targets [33]. Neutron multiplicity can be increased by using of a fissile material. In addition, important parameters of target material are thermal conductivity, caloric receptivity, melting and boiling points [37].

Moreover, the target should have such a size – typically cylinder with diameter of 10 cm and thickness of tens of cm (e.g., range of 1 GeV protons in thick tungsten target is about 30 cm, in lead target about 55 cm, see **Fig. 1.12**) that at once it incepts the main part of the high-energy cascade, and let spallation neutrons escape (see author's simulations in section 6.3.3).

Neutron multiplicities can be investigated using a liquid-scintillator detector with large angular acceptance, e.g., the $4\pi$ BNB (Berlin Neutron Ball) detector [39] and the ORION detector [40] consist of a spherical shell filled with liquid scintillator (which slow the produced neutrons by scattering with

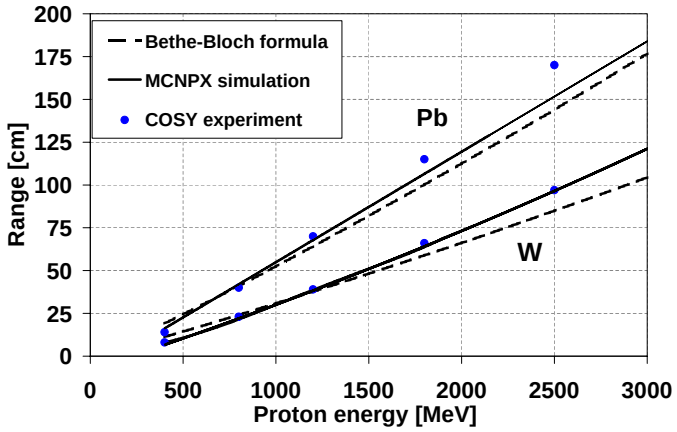


Figure 1.12: Range of protons in tungsten and lead. Various sources: Bethe-Bloch formula [38], MCNPX simulation (author's simulations), experiments of the NESSI collaboration [39].

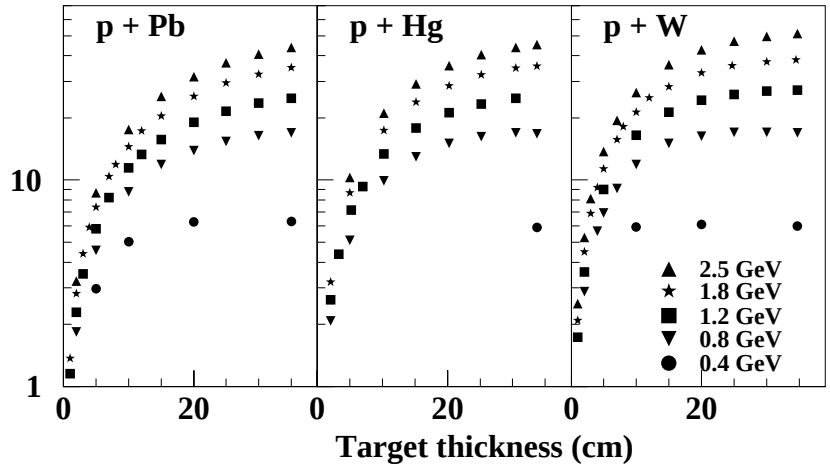


Figure 1.13: Neutron multiplicity as a function of target thickness and beam energy for Pb, Hg, W target materials. All targets were 15 cm in diameter (taken from [39]).

H and C nuclei) loaded with Gd that capture the moderated neutrons. The scintillator light is being registered with a set of photomultipliers distributed on the surface of the shell. Experiments with different target materials and sizes show that neutron multiplicity saturates at a given target thickness, which increases with the proton energy, see **Fig. 1.13** (compare with author's simulations in section 6.3.2).

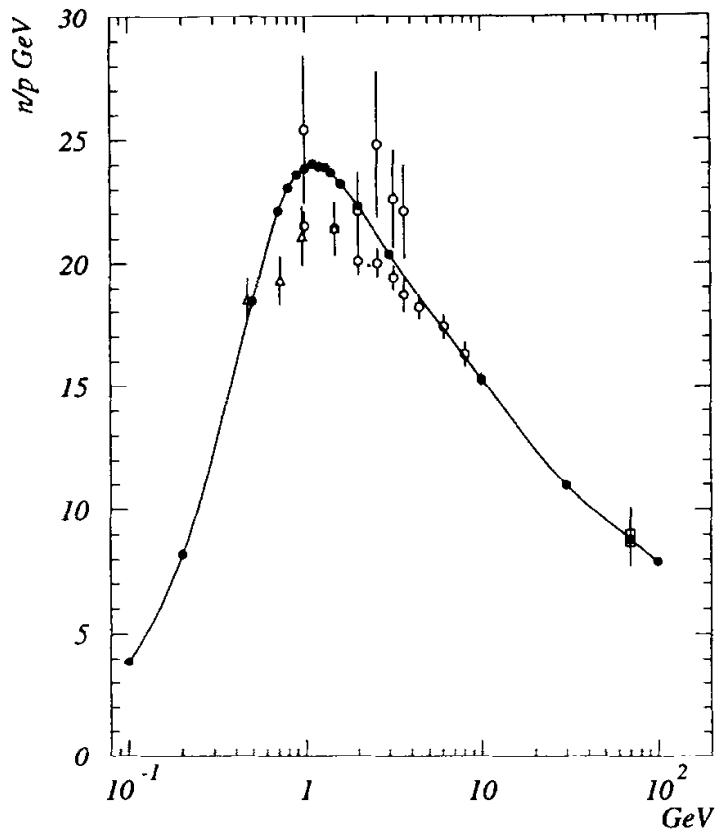


Figure 1.14: Numbers of neutrons with $E_{\mathrm{n}} < 10.5$ MeV (normalized per one incident proton and per unit of proton energy) escaping from the whole surface of the cylindric Pb-target (radius = 10 cm, length = 60 cm) in dependence on the incident proton energy (given in logarithmic scale): full circles represent Monte-Carlo calculations [36], the curve is drawn through the points to guide an eye; open symbols stand for experimental data: triangle [41], circle [42], square [43] - recounted from W to Pb (taken from [36]).

Besides multiplicity, an important quantity is the **neutron cost**, i.e., the number of produced neutrons normalized per one incident particle and per unit of its energy. Monte-Carlo simulations of neutron cost on thick, lead target as well as various experimental data show that the optimal proton energy for maximum neutron yield favourable for ADS purposes can be reached around 1 GeV [36], see **Fig. 1.14** (compare with author's investigation in section 6.3.3).

## 1.3 Transmutation concepts

The ADS principle based on a subcritical nuclear reactor driven by an external spallation neutron source was designed to produce fissile material and has already been suggested in the late 1940's.

The production of large amounts of neutrons by high-power accelerators became possible after the Lawrence's invention of a cyclotron in 1929. After participating the Manhattan Project, E. O. Lawrence brought in the idea of the accelerator as a neutron source with the intention to produce fissionable material. His MTA project (Materials Testing Accelerator) began at the Lawrence Livermore National Laboratory in California in 1950 [44]. He proposed to irradiate various thick targets (U, Be, Li) by protons and deuterons to measure the cross-sections, neutron yields, and the feasibility of converting the fertile (depleted uranium or thorium) to fissile material ($^{239}$Pu, $^{233}$U). This was the first motivation, because the USA were dependent on foreign uranium sources. The MTA project was closed a few years later when rich domestic uranium ores were found in the Colorado plateau.

During next decades, investigations important for the estimation of efficiencies of various modes of transmutation were performed. For example, neutron yields and spectra in lead and uranium targets irradiated by relativistic protons [34, 45] and nuclei [46] and neutron cross-sections for a number of isotopes have been measured in JINR Dubna.

The first quite conceptual and complex study of the radioactive waste transmutation has started at the end of 1980's at JAERI (Japan Atomic Energy Research Institute). A long-term program for research and development on nuclide partitioning and transmutation technology was called OMEGA [47] (Option Making Extra Gains from Actinides and Fission Products). This program initiated the global interest in transmutation topic that started from the beginning of 1990's.

At that time, two main projects have been published. C. Bowman from LANL (Los Alamos National Laboratory) created a detailed concept of the **Accelerator Transmutation of Waste** (ATW) [6] using *thermal* neutrons. He suggested the use of a linear accelerator with a high-intensive proton current ($\sim$ 250 mA) of 1.6 GeV energy.

C. Rubbia from CERN (Conseil Européen pour la Recherche Nucléaire = European Council for Nuclear Research) proposed a basic concept of the **Energy Amplifier** [48], also called **Accelerator Driven Energy Production** (ADEP). As the name implies, it does not pay interest to the disposal of radioactive waste directly. The motivation for ADEP is similar as for

the MTA project. This idea is based on the use of $^{232}$Th[7] as a fuel for the production of fissile $^{233}$U:

$$\mathrm{n} + {}^{232}\mathrm{Th} \longrightarrow {}^{233}\mathrm{Th} \xrightarrow[22\,\mathrm{m}]{\beta^-} {}^{233}\mathrm{Pa} \xrightarrow[27\,\mathrm{d}]{\beta^-} {}^{233}\mathrm{U}.$$

It reckons with a use of a 1 GeV cyclotron with smaller beam current than in LANL (12.5 mA) for transmutation by *fast* neutrons. In the case of using the Energy Amplifier for waste transmutation, the fast neutrons could fission all higher actinides, while the thermal neutrons in a classical nuclear reactor do not fission many of them.

Another idea of using waste as the fuel is called the **Accelerator Based Conversion of plutonium** (ABC). It is a proposal of burning $^{239}$Pu from struck nuclear warhead [51].

## 1.4 Advantages and disadvantages of ADS

Besides the elimination of the nuclear waste and energy generation, another advantage of ADS is its safety. The fissile material in ADS will have a composition such that a chain reaction could not run there and neutrons will be generated from an external source (i.e., from spallation reactions in the target). Therefore, a nuclear accident caused by an uncontrolled chain reaction will be foreclosed. In any case, transmutations will not be the final solution of nuclear waste problem. We will not be able to transmute completely all long-lived radioactive waste, so permanent storage in deep, underground, geologically-stable repositories will be necessary anyway. Nevertheless, the ADS could significantly decrease the volume of radioactive waste.

The main project problem of the accelerator driven facility is its size and high technologic requirements to run it. It is not possible to build a small, functional facility that could verify our assumptions. There exists a number of possibilities of how a real accelerator driven facility could look. However, the properties of eventual project will considerably influence its efficiency. If the facility were poorly designed, it would lead to a significant loss. Therefore, we must be able to describe the transmutation and related processes with a very high level of confidence. We should be able to describe as perfectly as possible the course of the spallation reactions between protons and target nuclei, the spatial and energetic distributions of the produced neutron

[7] Thorium is about three times more abundant element in the earth's crust than uranium. Particularly, India and Australia, thanks to their large reserves of thorium, plan to base their nuclear power programs on thorium [50].

field, the transport of neutrons (through various materials) which follows the spallation, and the probabilities of individual isotope transmutations.

## 1.5 Main experiments concerning ADS

Therefore, lot of projects all around the world have been established to carry out experiments for nuclear data acquisition, complement of the cross-section libraries, testing the accuracy of models describing spallation and transmutation reactions. The aim of such investigations is to design the optimal parameters of accelerator, beam, target, and blanket.

In European scale, several projects to verify the fundamental physics principle of ADS were established, e.g., n_TOF [52], FEAT (First Energy Amplifier Test) [53], and TARC (Transmutation by Adiabatic Resonance Crossing) [54] in CERN; SATURNE [55] and MUSE (MUltiplication Source Externe) [56] in France; TRADE (TRiga Accelerator Driven Experiment) [57] and TRASCO (TRAsmutazione SCOrie) [58] in Italy; MYRRHA (Multi-purpose hYbrid Research Reactor for High-tech Applications) [59] in Belgium; SPALADIN in Germany [60]; YALINA [61] in Belorussia; the HINDAS project (High and Intermediate energy Nuclear Data for Accelerator-driven Systems) [62] using six facilities throughout the Europe.

One of such places, where the investigation of ADS has been intensively carried out is also JINR Dubna. Currently, several directions of this research are being evolved there, see next four sections.

### 1.5.1 The Gamma project

The Gamma project is an instrument to study spallation neutron production by GeV protons on a thick, heavy target and the influence of moderator on the produced neutron field [63]. The setup consists of a thick target (Pb, U) of the diameter $d = 8$ cm and the length $l = 20$ cm surrounded by moderator. Until now, several experiments have been carried out with the paraffine moderator of the thickness of 6 cm (Gamma-2 setup). It is the best possible moderator, but technically useless because of low melting point and flammability.

The first experiment on the new setup called Gamma-MD (M stands for Minsk, D stands for Dubna) with the Pb-target of the length $l = 60$ cm and graphite moderator (technologically usable) of a cubic size ($110 \times 110 \times 60$ cm$^3$) was carried out in March 2007 with 2.33 $A$GeV deuteron beam.

The low-energy neutron spatial distribution is being measured by the activation sensors of $^{139}$La with (n,$\gamma$)-reaction. Transmutation of higher ac-

tinides and fission products in moderated neutron field is also being studied [64]. Thanks to the simple setup geometry, the experimental results from Gamma-2 and Gamma-MD experiments are useful for testing the accuracy of high-energy codes (see section 2).

### 1.5.2 The cross-sections measurements

The Phasotron accelerator is being used to study the cross-sections of the proton reactions ($E_p = 660$ MeV) on thin targets of fission products ($^{129}$I), natural uranium [65], and higher actinides ($^{237}$Np, $^{241}$Am [66], $^{239}$Pu). Thanks to the usage of direct kinematics technique (see section 1.2.1), many isotopes produced with wide spectrum of half-lives (from minutes until years) have been observed. The comparisons with computer codes have been performed [67] to check the theoretical models. The plan is to continue in the cross-section measurements and to carry out experiments with $^{232}$Th, $^{238}$Pu, $^{235}$U.

### 1.5.3 The SAD project

The SAD project [68] is a plan to construct the facility consisting of a replaceable spallation target (Pb, W) with a subcritical MOX blanket ($UO_2$ + $PuO_2$), using also the Phasotron accelerator. The motivation is to study the neutron production in such a setup (spectral and angular flux distributions), prompt neutrons life-time, effective fraction of the delayed neutrons, spallation product yields, power release, fission rates of actinides, transmutation rates of fission products, shielding efficiency, and accuracy of the computer codes and the nuclear databases used for calculations of the ADS characteristics. Final design is not given yet, preparation of equipments and theoretical calculations of the setup parameters are in progress [69]. The technical realization of the project was held up when Sweden withdrawed from the contract.

### 1.5.4 Energy plus Transmutation

"Energy plus Transmutation" (E+T) is a wide international collaboration (scientists from Armenia, Australia, Belorussia, the Czech Republic, Germany, Greece, India, Mongolia, Poland, Russia, Serbia, Ukraine) under the leadership of M. I. Krivopustov at LHE JINR. It uses the setup of the same name (**Fig. 1.15, 1.16**) consisting of a 28.66 kg thick lead target with a 206.4 kg deep-subcritical ($k_{\text{eff}} = 0.202$ [97]) natural uranium blanket surrounded by a polyethylene shielding (the whole assembly mass is 950 kg),

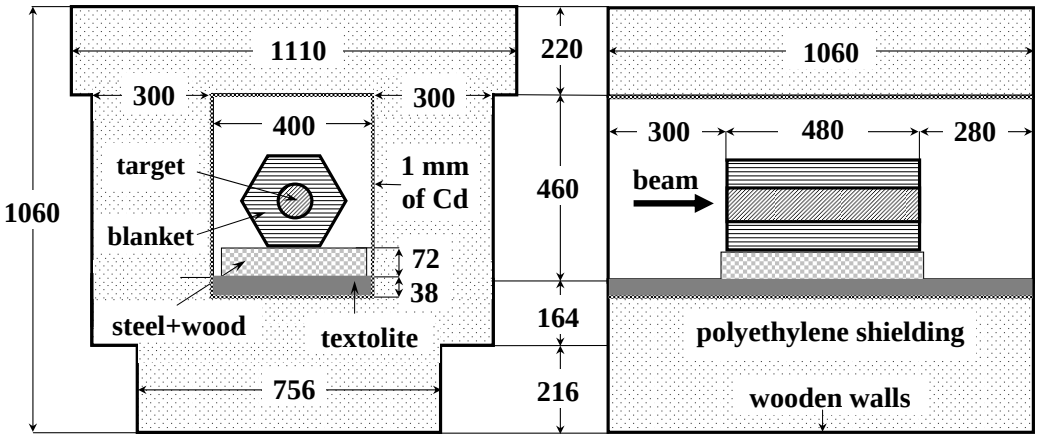


Figure 1.15: Front view (left) and cross-sectional side view (right) of the "Energy plus Transmutation" setup. Dimensions are in millimeters.

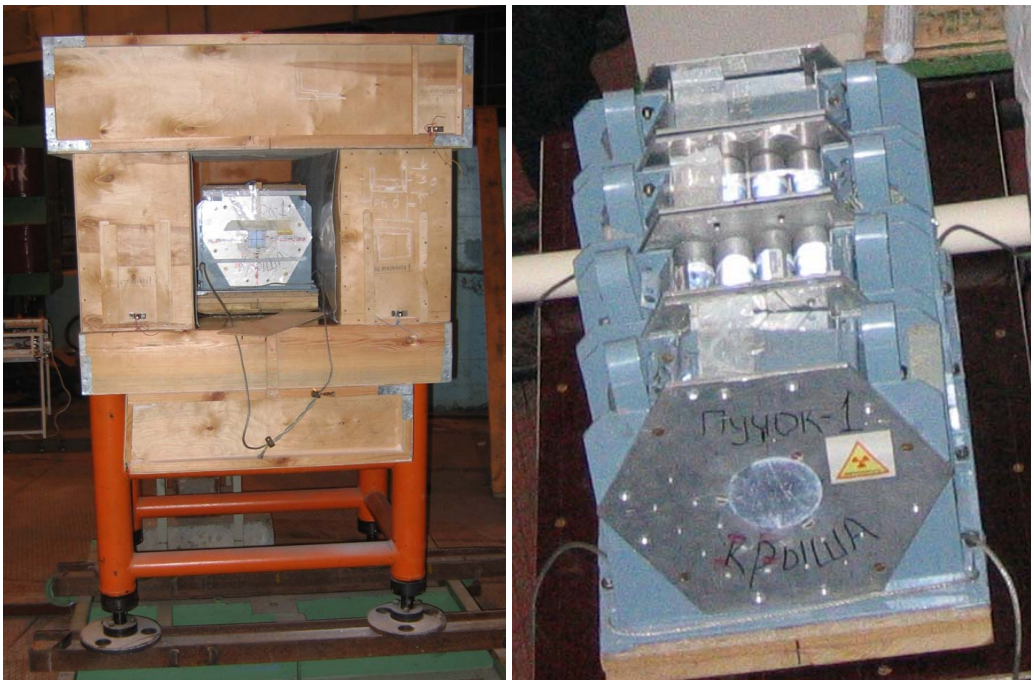

Figure 1.16: Photos of the "Energy plus Transmutation" setup (left) and the Pb/U–target/blanket assembly (right).

for details see section 3.2. The complex investigation within the frame of the E+T project pursues:

- transmutation of fission products and higher actinides (refined from burned-up nuclear fuel) by spallation neutrons [70-73, 81-83]
- the spatial and energetic distributions of spallation neutrons by the activation analysis method using Al, Au, Bi, Co, Cu, Dy, Fe, In, La, Lu, Mn, Nb, Ni, Ta, Ti, and Y sensors (neutron capture for thermal, epithermal, and resonance component, threshold reactions for fast component of neutron spectra) [85, 88, 91, 93, 96], solid state nuclear track detectors [74, 75, 76], nuclear emulsion techniques [77], and He-3 proportional counters [78];
- tests of the accuracy of the computer codes for calculation of neutron spectra and transmutation yields [87, 92, 95].

Before the E+T setup was completed, several experiments with simpler setups made of a lead or tungsten target (**Table 1.2**) optionally surrounded by a moderator (**Table 1.3**) were carried out using proton beams.

Six irradiations of the full E+T setup have been performed until now, on the proton beam with energies of 0.7, 1.0, 1.5, 2.0 GeV (**Table 1.4**) and deuteron beam with energies of 0.8 *A*GeV and 1.26 *A*GeV (**Table 1.5**).

This thesis describes measurements of spatial distribution of neutron field produced in the E+T proton experiments. Personally, the author participated (prepared the experiment and participated in irradiations and measurements) in the 0.7, 1.0, 2.0 GeV proton and 0.8, 1.26 *A*GeV deuteron experiments using the E+T setup, and the 660 MeV proton experiment at the bare Pb-target.

The author analysed fully the 885 MeV proton experiment on the Pb-target surrounded by moderator, the 1.0 and 2.0 GeV experiments using the E+T setup. The 0.7 GeV experiment was analysed mainly by O. Svoboda [98] (the author was a consultant of his diploma thesis), the 1.5 GeV experiment was analysed mainly by F. Křížek [99] (the author recalculated his results using additional correction factors). The author has done the systematics of the E+T proton experiments and compared the experimental results with MCNPX simulations. The author studied the influence of precision in a setup description on neutron production in the experiments with thick targets surrounded by a moderator [84]. A detailed study of the influence of individual components of the E+T setup was performed by M. Majerle [97].

Table 1.2: Proton experiments with a bare target.

| Proton energy [GeV] | 1.5 | 1.3 | 2.5 | 0.66 |
|---|---|---|---|---|
| Date [dd-mm-yy] | 25-06-98 | 21-06-00 | | 14-12-03 |
| Irradiation time [h:m] | 8:35 | 3:17 | 2:02 | 0:10 |
| Proton flux [$10^{13}$] | 0.186 | 2.77 | 4.07 | 158 |
| Target material | W | Pb | | Pb |
| diameter [cm] | 2.0 | 9.6 | | 9.6 |
| length [cm] | 60 | 48.6 | | 45.2 |
| Accelerator | Synchrophasotron | | | Phasotron |
| Published | [79, 80] | [83] | | [86, 90] |
| Range [cm] (from [159]) | 53 | 79 | 172 | 30 |

Table 1.3: Proton experiments with a target surrounded by a moderator.

| Proton energy [GeV] | 1.5 | 0.885 |
|---|---|---|
| Date [dd-mm-yy] | 24-06-98 | 05-11-99 |
| Irradiation time [h:m] | 3:56 | 2:03 |
| Proton flux [$10^{13}$] | 8.9 | 3.46 |
| Target material | Pb | Pb |
| diameter [cm] | 9.6 | 9.6 |
| length [cm] | 50 | 50 |
| Moderator material | polyethylene | polyethylene |
| dimensions [$cm^3$] | $106 \times 106 \times 111$ | $106 \times 106 \times 111$ |
| Accelerator | Synchrophasotron | Synchrophasotron |
| Published | [80] | [84, 88] |
| Range [cm] (from [159]) | 93 | 47 |

Table 1.4: Proton experiments with the E+T setup.

| Beam energy [GeV] | 0.7 | 1.0 | 1.5 | 2.0 |
|---|---|---|---|---|
| Date [dd-mm-yy] | 27-06-04 | 30-11-03 | 11-12-01 | 27-06-03 |
| Irradiation time [h:m] | 8:51 | 6:03 | 12:03 | 7:43 |
| Proton flux [$10^{13}$] | 1.52 | 3.30 | 1.14 | 1.25 |
| Range [cm] (from [159]) | 33 | 55 | 93 | 132 |
| Published | [98] | [96] | [93] | |

Table 1.5: Deuteron experiments with the E+T setup.

| Beam energy [$A$GeV] | 1.26 | 0.8 |
|---|---|---|
| Date [dd-mm-yy] | 30-11-05 | 18-12-06 |
| Irradiation time [h:m] | 8:00 | 6:47 |
| Deuteron flux [$10^{13}$] | 0.61 | 2.45 |
| Published | [153] | [154] |

### 1.5.5 Plans for future

Usual frequency of the E+T experiments is one or two times per year. Goals for future are to repeat one of the already performed experiments (i.e., the same energy and beam particle) to test if we get the same results and the setup can really provide worthwhile data, carry out experiments with bigger deuteron beam energies (up to 2.0 $A$GeV), carry out experiment without moderator, carry out experiment with the E+T setup with extended Pb-target and U-blanket [71] or a Pb+Bi eutectic (an alloy of 44.5% of lead and 55.5% of bismuth) as a target. Another proposal is suggested in section 6.2.2.

Further plans are connected with a helium-jet transport system [100] of fission-products. Such a system has capability to quickly transfer short-lived isotopes, with help of a helium flux, from their source to a detector. Uranium foils (with a thickness of 6 mg.cm$^{-2}$) in a cell on the target surface will be irradiated by spallation neutrons. The fission products (beside Xe, Kr) will be caught up by a chemical filter on the exit of the cell. The flux of helium will transport Xe and Kr from the cell into a Cu-pipe cooled in liquid nitrogen ($T_{\mathrm{boil}} = 77$ K), where Xe ($T_{\mathrm{boil}} = 165$ K) and Kr ($T_{\mathrm{boil}} = 120$ K) will be frost. The aim is to measure the production of Xe and Kr isotopes, their daughter's products, and fission products from the chemical filter.

# Chapter 2

# Simulations of high-energy nuclear reactions

As mentioned above, there is a strong need of simulation codes for ADS assembly projection. Several simulation codes and combinations of these codes (e.g., LAHET [101] and MCNP [102], MCNPX [103], FLUKA (FLUktuirende KAskade) [105], HETC (High Energy Transport Code) [106], NMTC (Nucleon Meson Transport Code) [107], NUCLEUS [142], INCL (Liège INC) [108], SHIELD [109], CASCADE [110], CEM (Cascade-Exciton Model) [111], LAQGSM (Los Alamos Quark-Gluon String Model) [112], GEM (Generalized Evaporation Model) [113], GEANT4 [114], JAM (Jet AA Microscopic Transport Model) [115], MARS [116], TIERCE [117], BRIEFF [118]) exist, which describe spallation reactions, interactions of secondary particles, and the following neutron transport through the target material. They are based on the *mathematical* Monte-Carlo method and they use various *physics* models of spallation reactions and cross-section libraries of neutron-induced reactions.

## 2.1 The Monte-Carlo method

The Monte-Carlo method [119] is a numerical technique used for simulating the behavior of various systems (from economics to particle physics) more complex than we otherwise can. In contrast to deterministic algorithms (used by other codes, section 2.3), it is a stochastic method. It is based on an executing of many random experiments (with a model of a system). The essential point is to have a high-quality generator of pseudo-random numbers (it is not necessary to use really random numbers). The result is a probability of some effect.

In particle reaction and transport tasks, individual particles trajectories are being simulated. To determine if an event occurs, the probabilities of possible physics processes (i.e., cross-sections) are used and random numbers are generated depending on the probability distributions for every case. The result of the particle life (so-called history) is being stored for the following assessment of average particle behaviour.

The statistical accuracy of results depends on the number of trials given to the simulation. The statistical error approximately matches inverse square root of the number of histories. That means, to reduce the error by a factor of two, the number of histories must quadruplicate. Accurate enough results for complex ADS systems are achievable in reasonable time thanks to the use of fast parallel computers, which can generate many events simultaneously [89].

## 2.2 The MCNPX code

Formerly, our group used a combination of the LAHET plus MCNP codes. LAHET (Los Alamos High Energy Transport Code) [101] can model spallation reactions and transport of nucleons, pions, muons, antinucleons with the energy $E \geq 20$ MeV. LAHET generates cross-sections for individual processes. MCNP (Monte Carlo N-Particle Transport Code) [102] is able to model the transport of neutrons (and photons and electrons) in an energy range $10^{-11}$ MeV $\leq E \leq 20$ MeV. It uses libraries of evaluated data as a source of the cross-sections.

Currently, I use the MCNPX (MCNP eXtended) code [103] and our whole group is a member of the MCNPX $\beta$-tester team. MCNPX improves and links the advantages of both LAHET and MCNP. MCNPX has been under continuous development since 1994 and it was first released to the public in 1999 as version 2.1.5 [120]. MCNPX supports 34 particle types, the ability to calculate interaction probabilities directly with physics models for energies where tabular data are not available.

MCNPX simulation of spallation reaction consists of three stages (see also section 1.2) and for each of them a special model is used. The first stage is the Intra-Nuclear Cascade (INC) on which a pre-equilibrium stage concurs. This is followed by an equilibrium evaporation that competes with a fission channel (fission fragments undergo an evaporation stage that depends on their excitation energy). After evaporation, a de-excitation of the residual nucleus follows, generating gammas. MCNPX enables to choose different models for description of individual stages of the spallation reaction.

### 2.2.1 Intra-nuclear cascade models

INC models (Bertini [121], Isabel [122], CEM [111], INCL4 [123]) describe interactions between an impinging particle and target nucleons during intra-nuclear cascade as a sequence of binary collisions (valid if the incident particle wavelength is smaller than a mean distance between nucleons of the target nucleus, thereto, a mean free path of the incident particle in the target nucleus is greater than the inter-nucleon lengths) separated in space and time. The trajectory between collisions is assumed to be linear.

The collisions proceed until a certain degree of equilibrium is reached. The criterion used in the INC model of Cugnon (INCL4) is an empirical time of equilibrium (so-called cutoff time $t_{\mathrm{cut}} \approx 30$ fm/c [124] that allows five sequential nucleon-nucleon interactions on the average), which was deduced from a clear change of the calculated quantities (like the integral number of emitted particles, their total kinetic energy or the excitation energy of the residual nucleus).

In the Bertini-type model (Bertini, Isabel) the equilibrium criterion is deduced from the energy of the fastest particle remaining in the nucleus (so-called cutoff energy $T_{\mathrm{cut}}$), which should be smaller than the nuclear potential well depth ($\approx 40$ MeV [21]).

The CEM code uses a criterion for the escape of a primary particle from the cascade stage via the effective local optical potential $W_{\mathrm{opt.mod}}(r)$ determined from the local interaction cross-sections, including the blocking effects due to the Pauli exclusion principle. This imaginary potential is compared with "experimental" potential $W_{\mathrm{opt.exp}}(r)$ determined in terms of the phenomenological global optical model by using data on elastic scattering by a nucleus. The convergence degree of imaginary potentials is determined via the parameter $P = |(W_{\mathrm{opt.mod}}(r) - W_{\mathrm{opt.exp}}(r))/W_{\mathrm{opt.exp}}(r)|$. If P exceeds an empirically selected value ($\approx 0.3$), the particle escapes from the cascade stage, becoming an exciton. With the selected P-value, the cascade part of the code becomes shorter than in other cascade models [125].

The nuclear density distribution is approximated by a step-function distribution (as a function of target radius), where the densities in regions with constant density (three for Bertini, seven for CEM03, 16 for Isabel) are fitted to the folded Saxon-Woods shape. In INCL4, the Saxon-Woods density distribution is used and cut at the radius described with a diffuseness parameter. Fermi motion of the nucleons and the quantum effects of Pauli blocking are taken into account. High-energy parts above the range of INC physics usability are taken from FLUKA [105].

### 2.2.2 Pre-equilibrium models

Pre-equilibrium models (Multistage Preequilibrium Exciton Model [126], Modified Exciton Model [127]) describe the process of energy equalization as a sequence of two-particle interactions, whereas the nucleus is, in each phase (i.e., after each interaction), defined as the number of particles and vacancies. This description of a nucleus is called the exciton model (an exciton is either a nucleon excited above the Fermi level or a vacancy under the Fermi level).

The exciton model solves the master equation[1] describing the equilibration of the excited residual nucleus that remains after the cascade reaction stage. While, the master equation of MPM neglects angular distributions of pre-equilibrium particles, MEM includes momentum and angular momentum conservations of the nuclear system at the pre-equilibrium and equilibrium evaporation stages. MPM considers only nuclear transitions in the direction of equilibration (change of $\Delta n = +2$ in the exciton number). MEM takes into account all possible nuclear transitions ($\Delta n = +2, -2, 0$), considering all possible positions of particlehole pairs with respect to the Fermi level ($\Delta n = 0$).

The nucleus comes near to the equilibrium particle-whole configuration with each interaction of incident or cascade particle with other nucleons. When the equilibrium state is reached, the pre-equilibrium model is replaced by evaporation model.

### 2.2.3 Evaporation and fission models

Evaporation models (Dresner [128], ABLA [129]) describe the equilibrium decay of an equilibrium nucleus with the excitation energy reached at the end of the pre-equilibrium stage. The probability of the nucleus decay into a certain channel depends on level densities in a final channel and on the probability of a passage through the energy barrier.

As a competitive process to equilibrium decay, high-energy fission can happen. MCNPX includes two models of residual nuclei fission: ORNL (Oak Ridge National Laboratory) model [130] for actinides with $Z \geq 91$ and RAL (Rutherford Appleton Laboratory) model [131] which covers fission of actinides and subactinides with $Z \geq 71$.

[1] A master equation is a phenomenological set of first-order differential equations describing the time evolution of the probability of a system to occupy each one of a discrete set of states.

### 2.2.4 Data libraries

MCNPX exploits the LA150 data library [132] of evaluated neutron and proton cross-sections up to 150 MeV, which have been developed at Los Alamos National Laboratory using experimental data as well as nuclear reaction models in the GNASH code [145].

New cross-section library NRG-2003 [133] up to 200 MeV (also in the ENDF-6 format [134]) has been evaluated at the Nuclear Research and Consultancy Group, the Netherlands, using mainly the TALYS code [144].

Presently, these nuclear data libraries include evaluations for the major isotopes of structural, shielding, and target-blanket importance (H, Li, C, N, O, Al, Si, P, Ca, Fe, Ni, Cr, Cu, Nb, W, Hg, Pb, Bi in LA150 [135]; Ca, Sc, Ti, Fe, Ni, Pb, Bi in NRG-2003 [136]).

The performed simulations confirm that both LA150 and NRG-2003 data libraries give the same yields (within few percent) when simulating the E+T experiments [97].

### 2.2.5 MCNPX input file

The MCNPX input file containing all information about the task has three main parts called cards, separated by white lines.

- The Cell Card contains information about the material in the cells, their densities, and the geometry of the cells defined using surfaces.
- The Surface Card defines coordinates of the surfaces in the setup.
- The Data Card contains other parameters of simulation like the cells materials, cross-section libraries, source definition (particle, energy, position, direction, shape), number of the particles to be simulated, and so-called tally cards that specify what type of information the user wants to gain. Tallies are normalized to be per source particle. MCNPX is able to simulate (to tally) current over a surface, flux at a point or over a surface or a cell, energy deposition over a cell, criticality etc.

The example of a MCNPX input file I used in MCNPX simulations can be found in Appendix A.

## 2.3 The TALYS code

TALYS [144] is a deterministic nuclear reaction code created at NRG Petten, the Netherlands, and CEA Bruyères-le-Châtel, France. It is new "all-in-one"

code (as GNASH [145], ALICE/ASH [146], STAPRE [147], EMPIRE [148], MEND [149]).

TALYS is able to simulate nuclear reactions in the 1 keV – 250 MeV energy range involving neutrons, protons, deuterons, tritons, helions, $\alpha$, and $\gamma$ (as projectiles and ejectiles), and targets with mass numbers between 12 and 339. It incorporates nuclear models for the optical model, level densities, direct, compound, pre-equilibrium, and fission reactions, and a large nuclear structure database. It calculates total and partial cross-sections, energy spectra, angular distributions, double-differential spectra, residual production cross sections, and recoils [150]. It has been tested with experimental data with very good results [151].

I use the TALYS code for calculation of (n,$x$n) and (p,$x$np)-reactions cross-sections, where the current status of usual nuclear data libraries is poor (section 6.2.2). An input file of TALYS consists of keywords and their associated values. The example of a TALYS input file I used can be found in Appendix D.

## 2.4 Validation of high-energy nuclear models

The state-of-the-art of the predicting capabilities of high-energy nuclear models is being studied by the comparisons between models and experimental data.

The total neutron production, which is of major importance for applications, can be predicted with a precision of $10 - 15\%$ [137] with any combination of INC and evaporation models used in MCNPX. General trends of energy, angular or geometry dependence are also well understood, although, local discrepancies, particularly in the $20 - 80$ MeV region, may be as large as a factor of 2 or so in extreme cases [137, 138, 139, 140, 141], see examples in **Fig. 1.3, 2.1**.

It is not always easy to determine whether the reason of the observed discrepancies comes from a lack of reliability of data or from faults in models and which part of model could be responsible for that. To solve these problems, more experiments are needed to be carried out for better understanding of the reaction mechanisms.

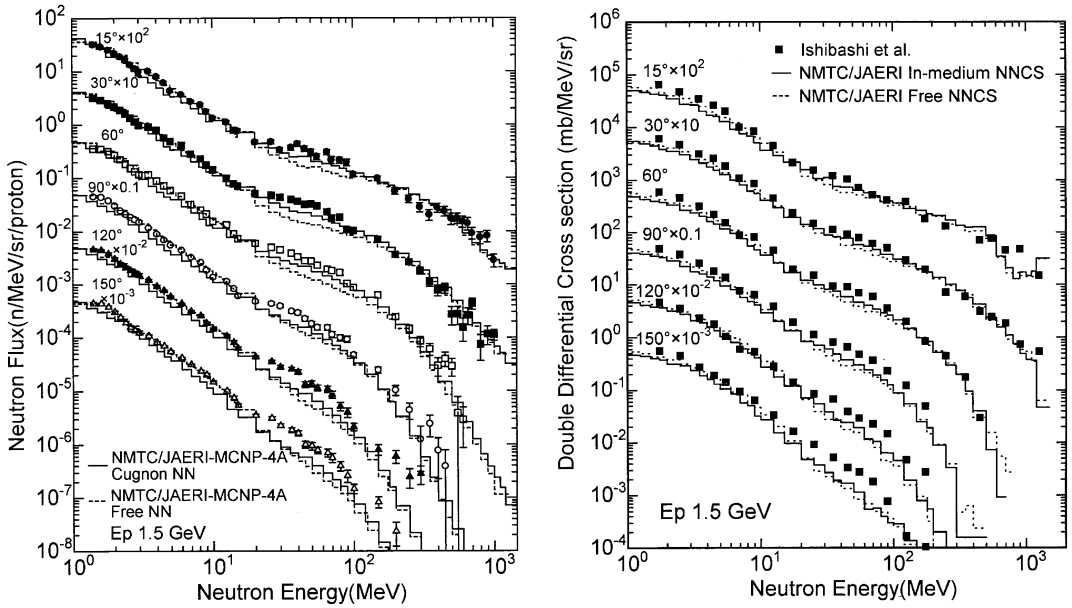


Figure 2.1: Neutron production in reactions of 1.5 GeV protons on a thick (left) and thin (right) Pb-target. Each successive curve is scaled by a factor of 10 with decreasing angle. Symbols indicate experimental data ([140] - left, [139] - right), dashed and solid lines show results of simulations [140].
The simulations underestimate (in comparison with the experiments) the neutron emission at deeper angles. Some studies [142, 143] suggested that the inclusion of the pre-equilibrium process or the refraction and reflection processes improved the backward neutron emission (taken from [140]).

# Chapter 3

# Experimental instruments

In this section, the description of the used experimental apparatus is given, i.e., type and parameters of accelerator, setup description, irradiation data, and description of the measurement methodology.

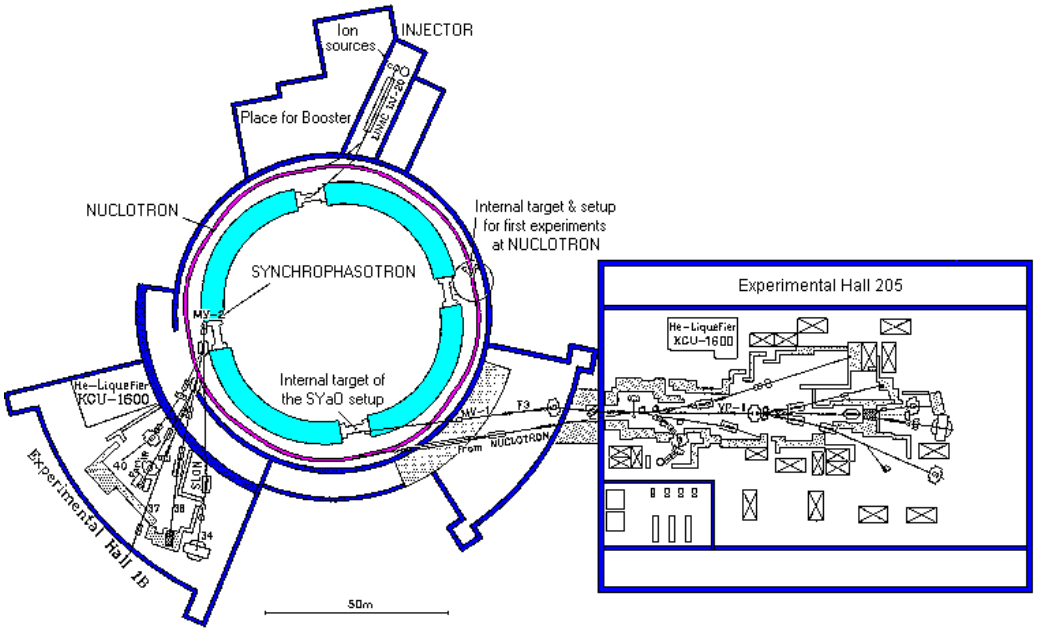


Figure 3.1: Accelerator complex of the Laboratory of High Energies, JINR Dubna (taken from [155]).

Figure 3.2: Nuclotron ring (left) and operating console of the Nuclotron (right) (taken from [155]).

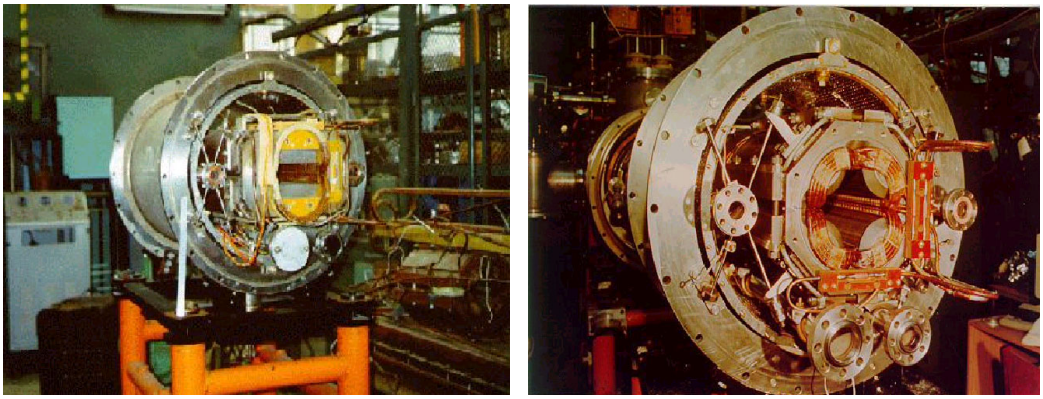

Figure 3.3: Nuclotron superconducting magnets. Dipole magnet (left) is anchored in the vacuum shell of the cryostat by eight parts of a stainless steel ($m = 500$ kg, $l = 1462$ mm, $B = 2$ T). Quadrupole magnet (right), $m = 200$ kg, $l = 450$ mm, grad $B = 33.4$ T/m (taken from [155]).

## 3.1 Nuclotron

Principal research instrument in JINR Dubna used for investigations in the transmutation field is the Nuclotron accelerator at the Veksler and Baldin Laboratory of High Energies (LHE) (**Fig. 3.1**). Nuclotron is a superconducting (SC), strong focusing (**Fig. 3.2, 3.3**) synchrotron. It was built under the leadership of A. M. Baldin during years 1987-1992 and it has worked since March 1993. The Nuclotron ring (with circumference of 251.5 m) is installed in the tunnel under the old Synchrophasotron accelerator, whereas the Nuclotron median plane is 3.7 m below the Synchrophasotron one. The total cold mass of its magnets is 80 tons. In total, it has 96 SC dipoles and

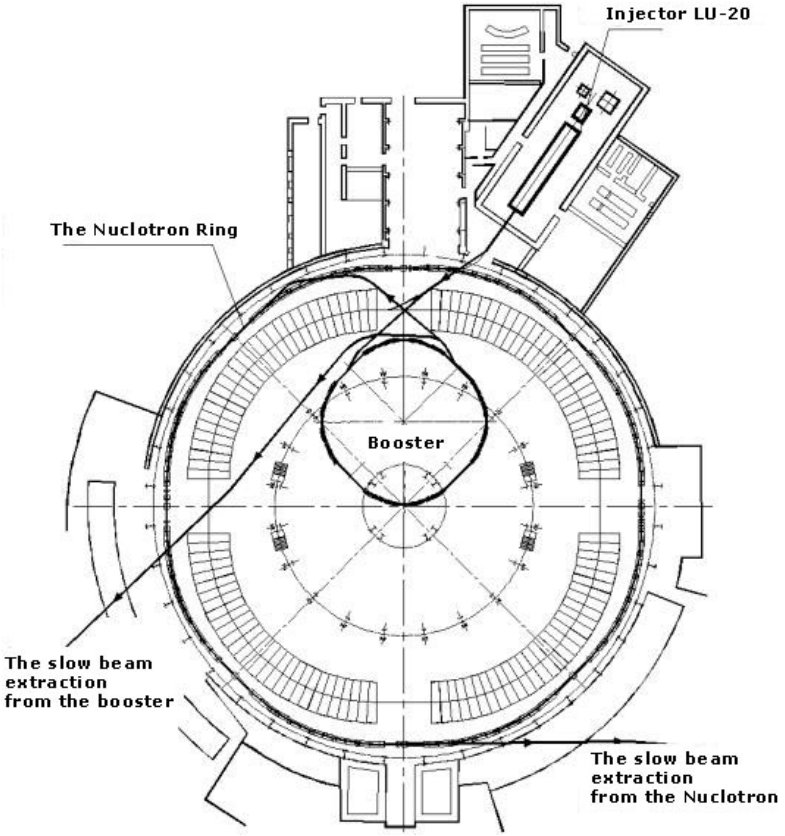


Figure 3.4: A design of the Nuclotron booster ring (taken from [156]).

64 SC quadrupoles. The designed maximal energies of accelerated particles are $E = 12.8$ GeV for protons and $E = 6$ $A$GeV for nuclei (up to $^{238}$U) with $\frac{Z}{A} = \frac{1}{2}$, however, the obtained parameters are about two times lower so far.

Basic research proceedings at Nuclotron regards investigation in the fields of a pre-asymptotic manifestation of quark and gluon degrees of freedom in nuclei, the study of the spin structure of the lightest nuclei, the search for hypernuclei, the study of polarization phenomena using polarized deuteron beams. There is also a number of projects being implemented in the frame of an applied research - radiobiology and space biomedicine, the impact of nuclear beams on the microelectronic components, the use of a carbon beam in cancer therapy, and transmutation of radioactive waste associated with the electro-nuclear energy generation method [157].

Lately, Nuclotron has suffered from adversities as a leakage of helium (December 2004) and an outage of electricity (owing to the storm in June 2005) and after-pollution of the vacuum tube. The projected construction of the

booster (**Fig. 3.4**) could enable to increase the intensity of the accelerated beams from the present value $3 \cdot 10^{10}$ particles per cycle by a few orders of magnitude. It will be the first stage of a new project of the Nuclotron-based Ion Collider fAcility (NICA) and Multi-Purpose Detector (MPD) [158] for the experimental study of hot and dense strongly interacting QCD matter.

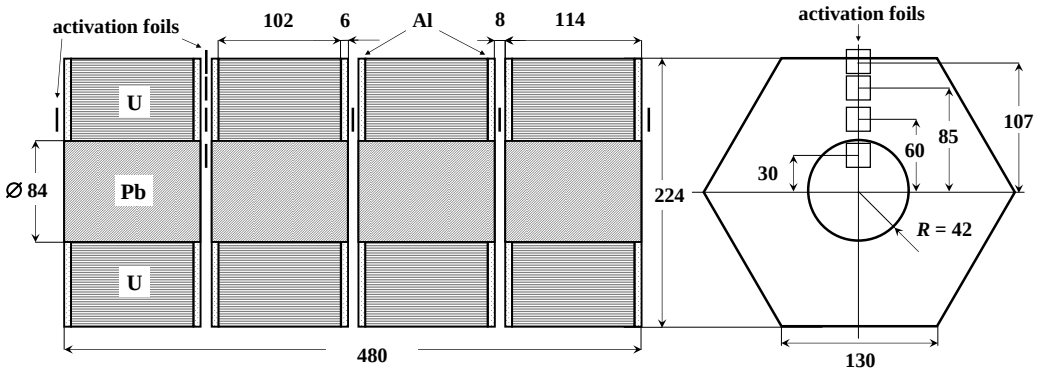


Figure 3.5: A typical placement of activation samples: side view (left), cross-sectional view in the first gap (right). Dimensions are in millimeters.

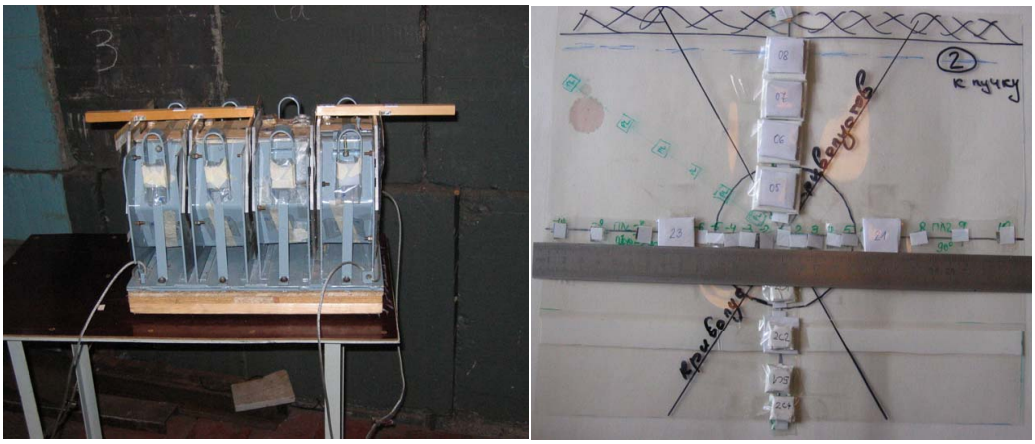

Figure 3.6: Photos of a side view of Pb/U assembly on a wooden-metal rack (left) and activation samples packed in paper (right).

## 3.2 The "Energy plus Transmutation" setup

The E+T setup (for general information see section 1.5.4) is divided into four sections of 114 mm in length separated by 8 mm gaps, totally 480 mm. Each section is composed of a cylindrical Pb-target (diameter of 84 mm) and a natural uranium blanket with a hexagonal cross-section (side length of 130 mm). Each blanket section contains 30 uranium rods (diameter of 36 mm, length of 102 mm). The front and back ends of every blanket section are closed by aluminium plates of 6 mm in thickness (**Fig. 3.5**). The Pb-target and the U-rods are sealed in an aluminium cover of 2.0 mm and 1.27 mm in thickness, respectively (not pointed in **Fig. 3.5**).

This Pb/U-assembly is fixed on a wooden-metal rack ($362 \times 505 \times 72$ mm$^3$) and a textolite[1] plate ($400 \times 1060 \times 38$ mm$^3$), see **Fig. 3.6**. The whole installation is placed inside a polyethylene shielding (granulated $(CH_2)_n$, $\rho =$ 0.802 g.cm$^{-3}$; the admixture of boron was tested with the result less than 5 ppm) of approximately cubic size ($1060 \times 1060 \times 1110$ mm$^3$) with walls of wood (thickness of 10 mm; the ribs of the box are made from wood bars with cross-section $50 \times 50$ mm$^2$), see **Fig. 1.15**. The inner walls of this container are coated with a Cd layer (thickness of 1 mm) used for absorption of thermal neutrons. The front and the back ends of the setup are without shielding.

The influence of individual setup components on the produced neutron field was studied by Monte-Carlo simulations [97]. While low-energy neutron field inside the setup is strongly influenced by the polyethylene shielding and the Cd-layer, the influence of these components on high-energy neutrons inside the setup is negligible, see **Fig. 3.7**.

## 3.3 Beam monitoring

The E+T setup was irradiated by proton beams with energies $E_p = 0.7$, 1.0, 1.5, 2.0 GeV (**Table 1.4**) and deuteron beams with energies $E_d = 0.8$ and 1.26 $A$GeV (**Table 1.5**). The courses of proton irradiations are shown in **Fig. 3.8**. The accuracy of the beam energy is estimated at the level of 0.5%.

In this section, measurement of the proton beam intensity and monitoring of the beam geometry (shape, location, direction) is described in general as it was done for all E+T experiments. As an example, the 1 GeV experiment is discussed in detail. The author measured beam intensity as well as geometry, compared them with results of other groups of the E+T collaboration

[1] Textolite (Latin textus – a cloth, and Greek lithos – stone) is a material consisting of several layers of fabric (filler); it is soaked by a synthetic resin.

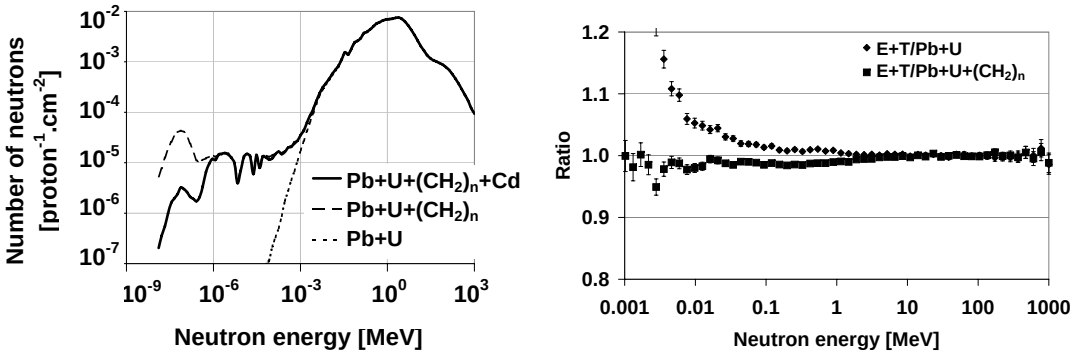


Figure 3.7: The influence of the polyethylene shielding and the Cd-layer on the produced neutron field. MCNPX simulation of the 1 GeV proton irradiation of the full E+T setup (Pb+U+Cd+$(CH_2)_n$) and two simplified setups. Oscillations in the region between $5 \times 10^{-6}$ and $5 \times 10^{-4}$ MeV are caused by resonances in the cross-section of neutron capture in $^{238}$U (**Fig. 6.19**) inside the blanket (left). Ratios of neutron fluxes from high-energy region of the left figure (right).

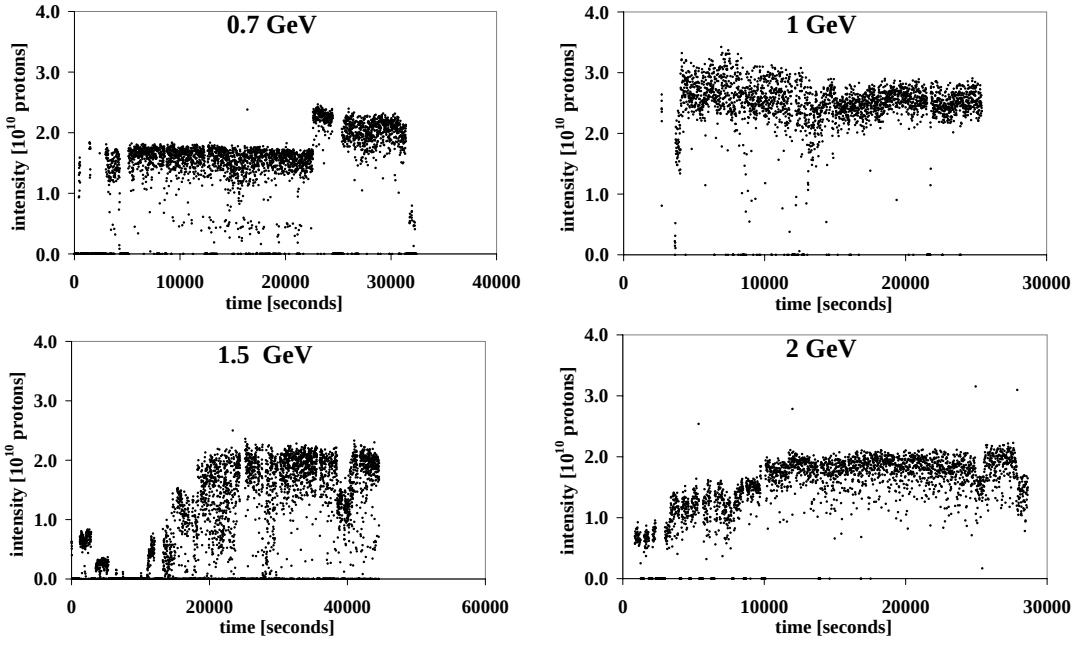


Figure 3.8: Proton beam intensities with the E+T experiments. Each point represents one proton spill (of duration about 10 s). Measured by a proportional chamber.

and calculated the final values used for other analysis by the whole E+T collaboration.

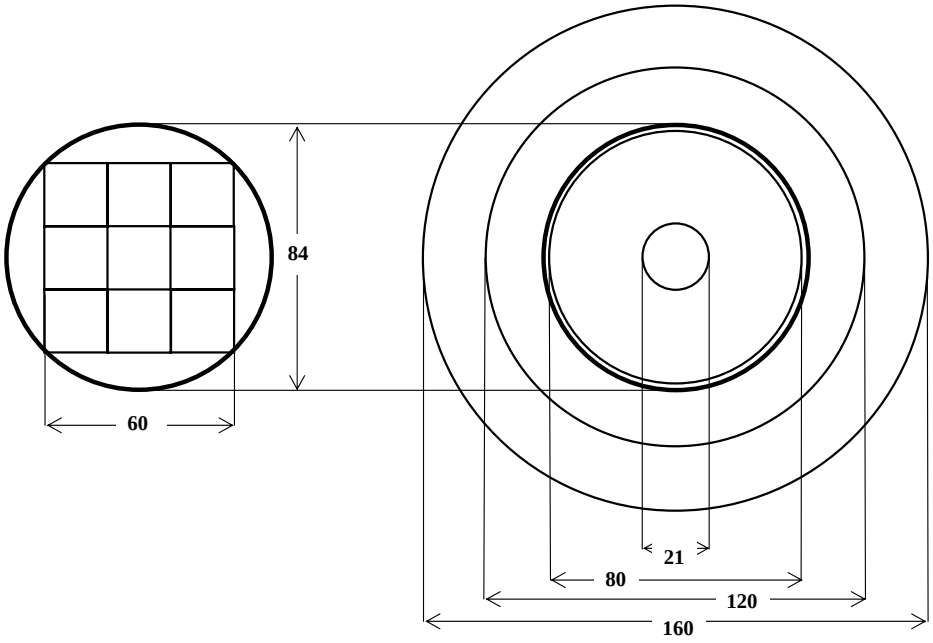


Figure 3.9: The position of a 6×6 cm$^2$ Cu-foil (non-separated yet) closely in front of the target (left). The position of concentric Al-foils 100 cm in front of the target (right). Dimensions are in millimeters.

### 3.3.1 Beam intensity

The total number of beam particles hit the target was determined by a proportional chamber, which suffers from a significant systematic uncertainty that can reach tens of per cent. However, the determination of a relative change of the beam intensity during a short time period (as our irradiations) is accurate enough, with uncertainty about 1%. The total beam flux was measured independently by two groups of the E+T collaboration, each of them using different types of beam monitor:

- I used a 8×8 cm$^2$ square $^{nat}$Cu-foil (69.17% $^{63}$Cu, 30.83% $^{65}$Cu) with a thickness of 25 $\mu$m placed closely in front of the target;
- W. Westmeier used a circular $^{27}$Al monitor (with thickness of 30 $\mu$m) cut into an inner circle with diameter of 21 mm, and three concentric rings with external diameters of 80, 120, 160 mm (**Fig. 3.9**) placed 100 cm in front of the target, what is sufficient to avoid interactions of backscattered neutrons with the Al-foils [160].

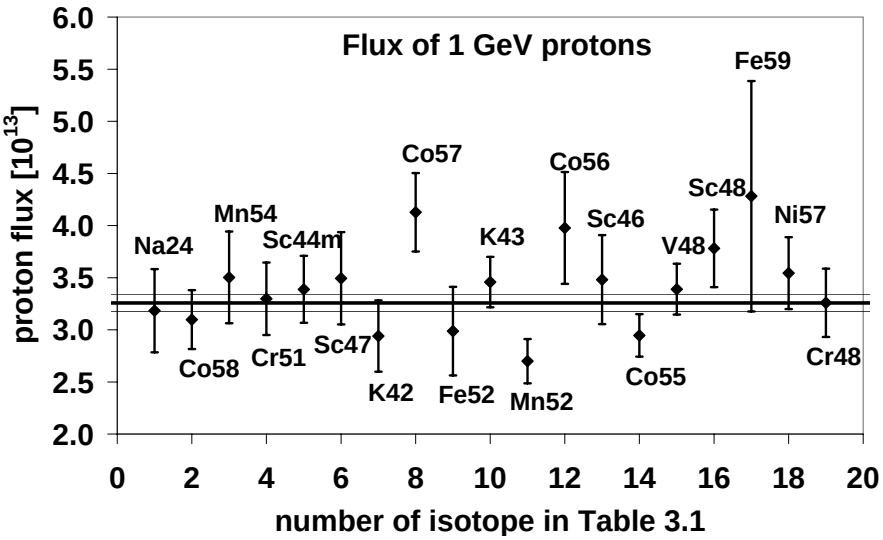


Figure 3.10: Values of the integral proton flux determined according to the yields of the identified isotopes in the Cu-monitor. The central thick line represents the weighted average, the thinner lines represent its error. Example of the 1 GeV experiment.

In the process of irradiation, the $^{27}$Al nuclei were transmuted by (p,3pn)-reaction into $^{24}$Na. In Cu-foils many products of $^{\mathrm{nat}}$Cu(p,X)-reactions were measured and the following isotopes were identified: $^{24}$Na, $^{58,57,56,55}$Co, $^{54,52}$Mn, $^{59,52}$Fe, $^{51,48}$Cr, $^{48,47,46,44m}$Sc, $^{57}$Ni, $^{48}$V, $^{43,42}$K, $^{61}$Cu. They have well known cross-sections with weak energetic dependence in our energy region.

After the irradiation, I measured its activity with the HPGe spectrometer a few times in order to identify the products of (p,X)-reactions with different half-lives. The number of nuclei of a $\beta$-radioactive isotope $^{A}_{Z}$Res produced during the whole period of the irradiation

$$N(^{A}_{Z}\mathrm{Res}) = I_{\mathrm{p}} n_j \sigma \tag{3.1}$$

is proportional to the number of beam protons $I_{\mathrm{p}}$, the probability $\sigma$ of (p,X)$^{A}_{Z}$Res-reaction, and the number of target nuclei per unit area:

$$n_j = \frac{1}{S}\frac{m}{\frac{M_m}{N_A}}, \tag{3.2}$$

where $M_m$ is the molar mass of a chemical element from which the foil monitor is made, $m = V\varrho = S\Delta x\varrho$ is mass of the foil with surface $S$, thickness $\Delta x$, and density $\varrho$, Avogadro's number $N_A = 6.022 \times 10^{23}$ mol$^{-1}$.

Table 3.1: The values of the integral proton flux calculated from yields of the identified isotopes in the Cu-monitor, the cross-sections of the corresponding $^{nat}$Cu(p,X)-reactions [163]. Example of the 1 GeV experiment.

| | isotope | $T_{1/2}$ [d] | $\sigma$ [mb] | $\Delta\ \sigma$ [mb] | $\Delta\ \sigma/\sigma$ [%] | $I_p$ [$10^{13}$] | $\Delta I_p$ [$10^{13}$] |
|---|---|---|---|---|---|---|---|
| 1 | $^{24}$Na | 0.623 | 1.02 | 0.10 | 10 | 3.2 | 0.4 |
| 2 | $^{58}$Co | 70.9 | 30 | 2 | 7 | 3.1 | 0.3 |
| 3 | $^{54}$Mn | 312 | 19.4 | 0.8 | 4 | 3.5 | 0.4 |
| 4 | $^{51}$Cr | 27.7 | 25.4 | 1.1 | 4 | 3.3 | 0.3 |
| 5 | $^{44m}$Sc | 2.44 | 5.6 | 0.4 | 7 | 3.4 | 0.3 |
| 6 | $^{47}$Sc | 3.35 | 2.84 | 0.28 | 10 | 3.5 | 0.4 |
| 7 | $^{42}$K | 0.515 | 3.3 | 0.2 | 6 | 3.0 | 0.3 |
| 8 | $^{57}$Co | 273 | 23.7 | 1.3 | 5 | 4.1 | 0.4 |
| 9 | $^{52}$Fe | 0.345 | 0.20 | 0.01 | 5 | 3.0 | 0.4 |
| 10 | $^{43}$K | 0.929 | 1.25 | 0.06 | 5 | 3.5 | 0.2 |
| 11 | $^{52}$Mn | 5.59 | 9.6 | 0.7 | 7 | 2.7 | 0.2 |
| 12 | $^{56}$Co | 77.3 | 9.2 | 0.6 | 7 | 4.0 | 0.5 |
| 13 | $^{46}$Sc | 83.8 | 6.69 | 0.33 | 5 | 3.5 | 0.4 |
| 14 | $^{55}$Co | 0.730 | 1.38 | 0.06 | 4 | 3.0 | 0.2 |
| 15 | $^{48}$V | 16.0 | 13.3 | 0.8 | 6 | 3.4 | 0.2 |
| 16 | $^{48}$Sc | 1.82 | 0.61 | 0.03 | 5 | 3.8 | 0.4 |
| 17 | $^{59}$Fe | 44.5 | 1.66 | 0.14 | 8 | 4.3 | 1.1 |
| 18 | $^{57}$Ni | 0.0247 | 0.81 | 0.05 | 6 | 3.6 | 0.3 |
| 19 | $^{48}$Cr | 0.898 | 0.40 | 0.02 | 5 | 3.3 | 0.3 |

I calculated the values of the integral proton flux (using eq. (3.1), (3.2)) for all observed isotopes as

$$I_p = \frac{N(^A_Z\mathrm{Res})}{\varrho \Delta x \frac{N_A}{M_m}\sigma}, \tag{3.3}$$

see example of results in **Tables 3.1, 3.2** and **Fig. 3.10**.

- The weighted average value of the integral 1 GeV proton flux determined by activation of the Cu-foil is $I_p = (3.26 \pm 0.08) \times 10^{13}$ with $\chi^2 = 1.3$. The error of the integral proton flux includes statistical errors and inaccuracies of determination of the corresponding cross-sections, which were acquired by interpolation using EXFOR/CSISRS data base values (mostly [161], [162]).

- The 1 GeV proton beam integral determined by activation of the Al-foil is (using the fitted value of [161] $\sigma = 10.53(11)$ mb for $^{27}$Al(p,3pn)$^{24}$Na) $I_p = (3.14 \pm 0.14) \times 10^{13}$, see the last line of **Table 3.2**.

Table 3.2: Results of the beam intensity measurement with the big segmented Al-monitor and the Gaussian fit of the beam profile. Example of the 1 GeV experiment.

| Foil | inner circle | 1st ring | 2nd ring | 3rd ring |
|---|---|---|---|---|
| Inner diameter [cm] | 0 | 2.1 | 8.0 | 12.0 |
| Outer diameter [cm] | 2.1 | 8.0 | 12.0 | 16.0 |
| $^{24}$Na activity [Bq] | $121 \pm 5$ | $495 \pm 22$ | $39.0 \pm 1.9$ | $6.7 \pm 0.5$ |
| Gaussian fit [Bq] | 116.9 | 501.7 | 37.1 | 1.1 |
| Proton beam [$10^{13}$] | $0.58 \pm 0.02$ | $2.35 \pm 0.11$ | $0.186 \pm 0.009$ | $0.032 \pm 0.002$ |

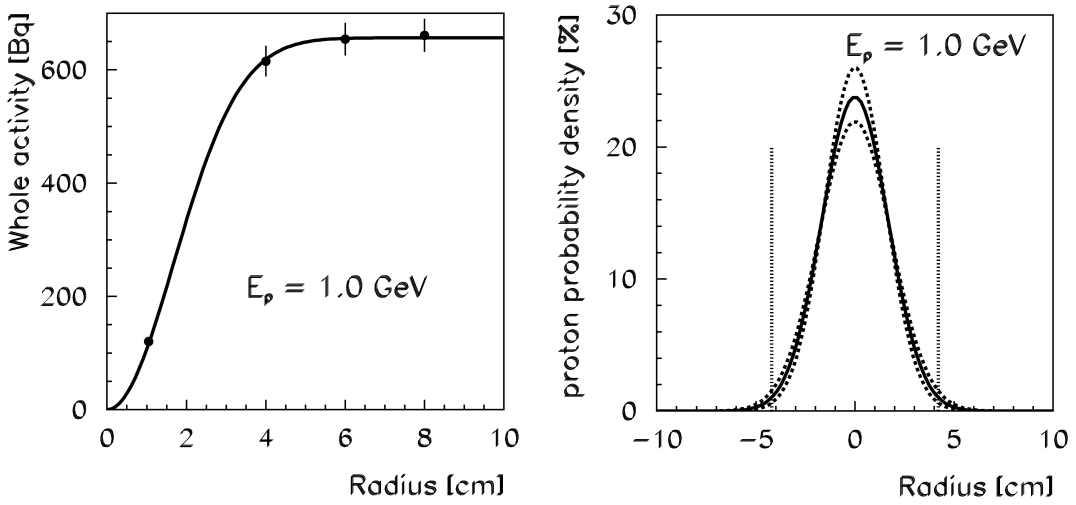


Figure 3.11: Description of the 1 GeV beam profile 100 cm in front of the target. The dependence of the foil activity on the radius of the circle (left), the fitted beam profile (right).

Assuming that the shift of the beam centroid from the center of the monitor was negligible, the data were fitted with a Gaussian distribution

$$P(x) = \frac{\exp\left(-\frac{(x-\mu)^2}{2\sigma^2}\right)}{\sigma\sqrt{2\pi}}. \tag{3.4}$$

This approximation is good for the central part of the beam, but not for its tails. The obtained parameter of the mean-root-square error is $\sigma = 1.68(14)$ cm that means FWHM = 3.96(33) cm. The fit accuracy can be seen in **Table 3.2**, where experimental and fitted data are compared and in **Fig. 3.11** (left), where the measured activities are shown as

a function of the monitor radius and compared with the experimental data. Using the obtained beam profile, it is possible to calculate that 4.4% of the beam is out of the target (diameter of 8.4 cm) at this distance. The profile with errors are shown in **Fig. 3.11** (right).

The ratio between the 1 GeV proton integral obtained with the whole Al-monitor (diameter of 16 cm) and the proton integral obtained with the Cu-monitor (8×8 cm) is possible to calculate using the beam profile obtained using the segmented Al-monitor and track detectors. I used a simplifying assumption that the beam profile is circular and it has FWHM = 4.0 cm. The ratio (the whole integral to the integral on 8×8 cm) is 1.038 and the full proton integral calculated from the 8×8 cm Cu-monitor is $I_{\mathrm{p}} = (3.38 \pm 0.10) \times 10^{13}$. The weighted average of both values is $(\mathbf{3.30 \pm 0.08}) \times \mathbf{10^{13}}$, which is the final value used for all other analyses by the whole E+T collaboration.

The results of beam integral measurement of all E+T proton experiments are summarized in **Table 3.6**.

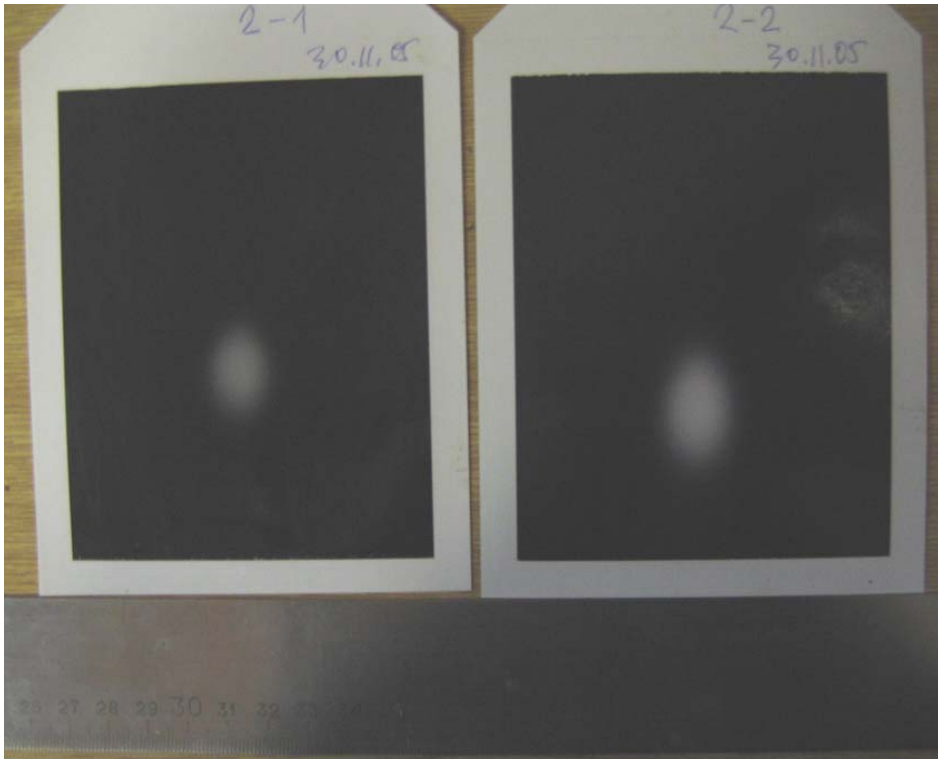


Figure 3.12: The traces of one bunch of beam particles on Polaroid foils placed in front of the target (left) and behind it (right). Photo from the d+Pb at 1.26 $A$GeV experiment.

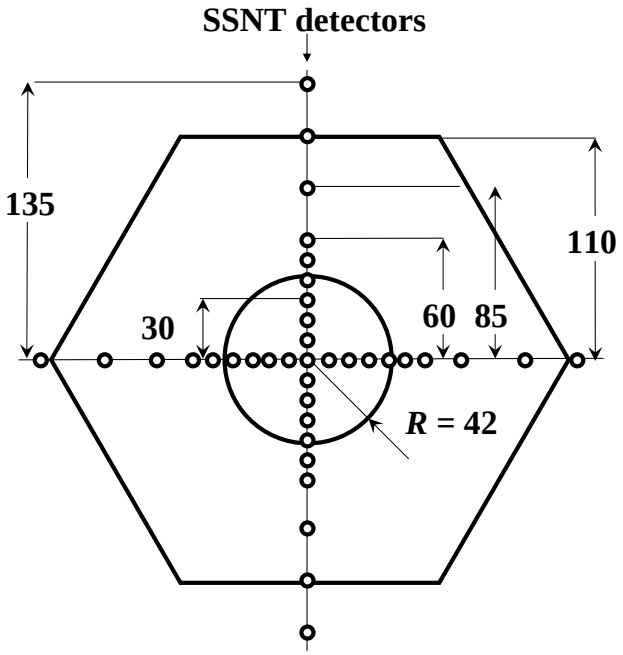


Figure 3.13: Typical placement of the solid state nuclear track detectors used for beam monitoring. Dimensions are in millimeters.

### 3.3.2 Beam geometry

The beam geometry was also studied independently by two groups of the E+T collaboration. First, before the beginning of the proper irradiation, one spill of protons was sent to Polaroid foils (placed at the front and the end of the target) in order to check the shape, location, and direction of the beam, see **Fig. 3.12**. After the check that the beam

- is more or less centred on the forehead of the target,
- goes approximately in a parallel way with the target axis,
- has an ellipse shape close to a circle and sufficiently small half-axes,

two sets of monitors were placed into the setup to measure the beam profile.

- I used a 6×6 cm$^2$ square Cu-foil with a thickness of 50 $\mu$m placed closely in front of the target. After irradiation I cut this foil into nine pieces (see **Fig. 3.9**) and measured activities of each of these 2×2 cm$^2$ foils separately. I used this technique in order to avoid void spaces between a group of nine foils as it was problem in previous experiments.

Table 3.3: Ratios of the yields of $^{nat}$Cu(p,X)-reactions in the central foil to other foils (weighted averages over all observed isotopes). Example of the 1 GeV experiment, where the group of five foils in the form of a cross was used for the Cu-monitor; the above mentioned group of nine foils in the form of a square has been used in recent experiments.

| | ratio | error |
|---|---|---|
| centre/left | 0.15 | 0.03 |
| centre/down | 0.29 | 0.02 |
| centre/right | 0.24 | 0.01 |
| centre/up | 0.65 | 0.01 |

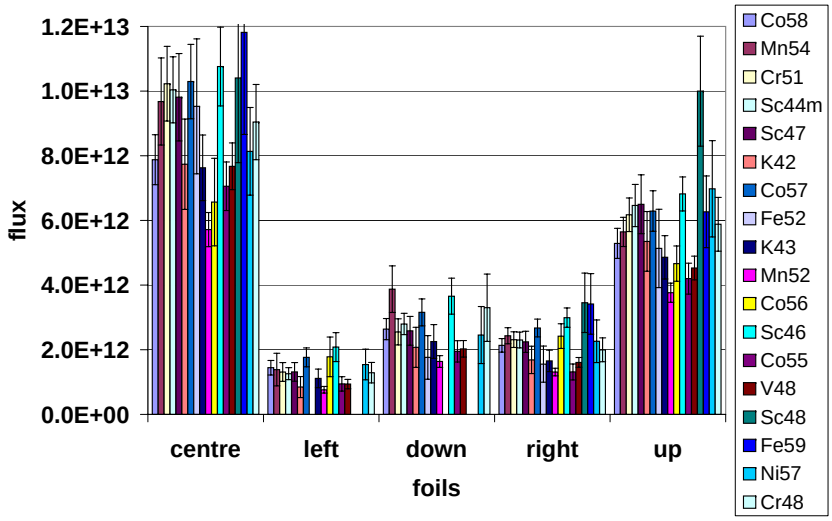


Figure 3.14: Fluxes through the set of five Cu-foils determined from all observed isotopes. Example of the 1 GeV experiment.

I observed the same products of $^{nat}$Cu(p,X)-reactions as in the case of a beam intensity monitor, see section 3.3.1.

I compared the yields of these isotopes in different foils (see examples in **Table 3.3** or **Fig. 3.14** for comparison of fluxes through foils showing also the consistency of spectrum analysis) and concluded that the 1 GeV proton flux in front of the target had approximately an ellipse shape and determined the shift of the beam centre (0.5(3) cm upwards, 0.2(3) cm to the right) and the sizes of the half-axes (the major axis in vertical direction of 4.0(3) cm and the minor axis in horizontal direction of 2.7(3) cm.

Table 3.4: Data from the track detectors - in front of the target. 1 GeV experiment.

| Distance from the center [cm] | bottom – top [$10^3$ tracks] | relative error [%] | left – right [$10^3$ tracks] | relative error [%] |
|---|---|---|---|---|
| -13.5 | 2.39 | 10 | 0.516 | 10 |
| -11.0 | 4.43 | 10 | 0.951 | 10 |
| -8.5 | 8.13 | 3 | 1.62 | 3 |
| -6.0 | 43.6 | 3 | 2.39 | 3 |
| -5.0 | 99.7 | 3 | 5.90 | 3 |
| -4.0 | 370 | 3 | 22.6 | 3 |
| -3.0 | 1670 | 3 | 176 | 3 |
| -2.0 | 2300 | 5 | 740 | 5 |
| -1.0 | 5230 | 5 | 2190 | 5 |
| 0.0 | 5830 | 5 | 5830 | 5 |
| 1.0 | 5530 | 5 | 4670 | 5 |
| 2.0 | 2640 | 5 | 1600 | 5 |
| 3.0 | 1670 | 3 | 278 | 3 |
| 4.0 | 476 | 3 | 25.5 | 3 |
| 5.0 | 111 | 3 | 6.74 | 3 |
| 6.0 | 51.7 | 3 | 3.43 | 3 |
| 8.5 | 10.7 | 3 | 2.12 | 3 |
| 11.0 | 1.17 | 10 | 5.59 | 10 |
| 13.5 | 0.571 | 10 | 3.04 | 10 |

- I. Zhuk used solid state nuclear track (SSNT) detectors [74]. This method is based on the measurement of distributions of natural lead induced fission rates. Two subsets (each of 19 lead samples) were placed just in front of the target in two directions: from left to right and from bottom to top, see **Fig. 3.13**. The same sets were placed also between the first and second target/blanket sections to check the parallelism between the beam and the target axes and to measure the defocusing of the beam while passing through the target. The numbers of the observed tracks in all samples for the 1 GeV beam are in **Tables 3.4, 3.5**. The experimental data were fitted by the Gaussian distribution, see example in **Fig. 3.15**.

  The fitting in front of the target gives the shift of the 1 GeV proton beam center in both directions (0.1(2) cm upwards, 0.3(2) cm to the right side) and the ellipse shape of the beam with major axis in vertical direction FWHM = 4.1(3) cm (i.e., $\sigma$ = 1.76(14) cm) and the minor axis in horizontal direction FWHM = 2.3(3) cm (i.e., $\sigma$ = 1.00(19) cm).

Table 3.5: Data from the track detectors – between the first and second target sections. 1 GeV experiment. In this case two sensors were situated in the point [0;0]. Difference between their values appears from the uncertainty in 1-2 mm of sensor position (difference is significant if gradient is strong) and the statistic uncertainty (the values are in the errors interval).

| Distance from the center [cm] | bottom - top [$10^3$ tracks] | relative error [%] | left - right [$10^3$ tracks] | relative error [%] |
|---|---|---|---|---|
| -13.5 | 4.47 | 10 | 3.40 | 10 |
| -11.0 | 7.31 | 10 | 1.71 | 10 |
| -8.5 | 12.2 | 10 | 10.4 | 10 |
| -6.0 | 42.2 | 10 | 27.6 | 10 |
| -5.0 | 87.2 | 10 | 48.2 | 10 |
| -4.0 | 318 | 10 | 88.4 | 10 |
| -3.0 | 721 | 10 | 96.2 | 10 |
| -2.0 | 1610 | 10 | 374 | 10 |
| -1.0 | 2540 | 10 | 2660 | 10 |
| 0.0 | 2530 | 10 | 2760 | 10 |
| 1.0 | 2380 | 10 | 2410 | 10 |
| 2.0 | 1810 | 10 | 1540 | 10 |
| 3.0 | 651 | 10 | 413 | 10 |
| 4.0 | 226 | 10 | 47.9 | 10 |
| 5.0 | 83.3 | 10 | 37.0 | 10 |
| 6.0 | 42.0 | 10 | 20.7 | 10 |
| 8.5 | 13.9 | 10 | 6.20 | 10 |
| 11.0 | 8.27 | 10 | 2.88 | 10 |
| 13.5 | 4.73 | 10 | 1.66 | 10 |

The beam between the first and second target sections had very similar ellipse shape as in front of the target. The beam profile is only a little broader with major axis in vertical direction FWHM = 4.5(2) cm (i.e., $\sigma$ = 1.88(10) cm), and the minor axis in horizontal direction FWHM = 3.0(4) cm ($\sigma$ = 1.29(15) cm). The center of the ellipse was shifted 0.1(1) cm downwards, 0.4(2) cm to the right.

These results agree within the error bars with the results for the beam centre position and beam size determined with the Cu-monitors. Also the result of the Al-monitor analysis (FWHM = 3.96(33) cm 100 cm in front of the target) is in very good agreement. For further purposes, the weighted averages of the Cu-monitor and the SSNT detectors were used: the 1 GeV proton beam had an ellipse shape with half-axes of **4.1(2) cm** in vertical

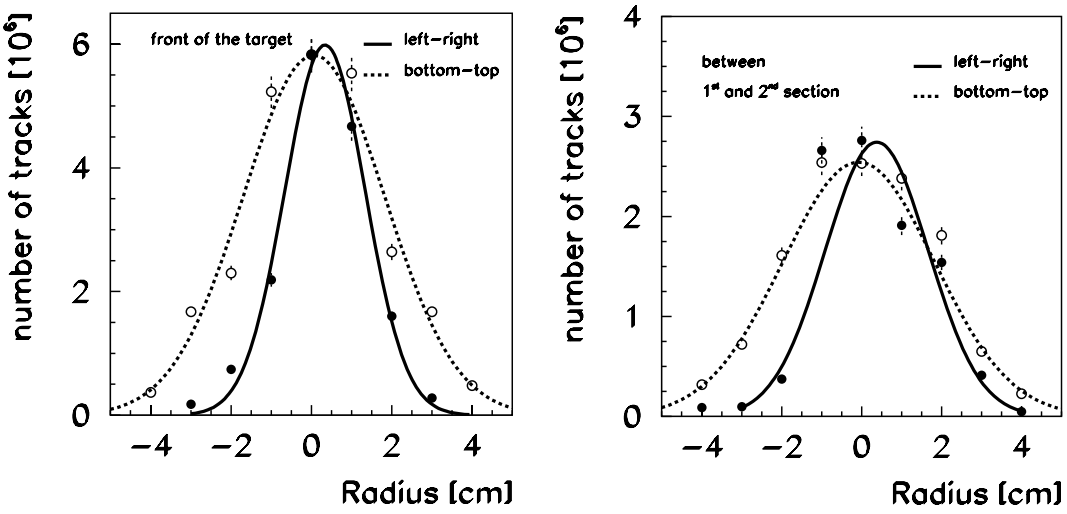


Figure 3.15: Profile of the 1 GeV beam in front of the target (left) and in the first gap between target sections (right) fitted with a Gaussian curve (measured by SSNT detectors).

Table 3.6: Parameters of irradiations (FWHM = $2.35\sigma$ for the Gaussian curve).

| Proton energy [GeV] | 0.7 | 1.0 | 1.5 | 2.0 |
|---|---|---|---|---|
| Beam integral [$10^{13}$] | 1.52(11) | 3.30(8) | 1.14(6) | 1.25(6) |
| Vertical half-axis [cm] | 5.9(2) | 4.1(2) | 3.7(5) | 5.4(3) |
| Horizontal half-axis [cm] | 5.9(2) | 2.5(2) | 2.4(5) | 3.8(3) |
| Position vertical [cm] | 0.5(3) | 0.2(2) | 0.1(2) | 0.3(2) |
| Position horizontal [cm] | 0.1(2) | 0.3(2) | 0.3(2) | -1.4(2) |

direction, **2.5(2) cm** in horizontal direction and it was shifted **0.2(2) cm** up, **0.3(2) cm** right.

For average beam parameters obtained independently by above mentioned methods see **Table 3.6**. The errors include statistical errors and inaccuracies of determination of the corresponding cross-sections of (p,X)-reactions, which were acquired by interpolation using EXFOR/CSISRS data base values [163].

We found out from simulations [97] that the accuracy of experimental data is not much influenced by the uncertainties of the beam profile width, but it strongly depends on the uncertainties in the beam position. The uncertainty of the beam position is around 3 mm, what means uncertainties in the neutron field up to 15%.

## 3.4 Neutron Activation Analysis

The spatial distribution of the produced neutron field was measured by the activation analysis method [164] that is based on the nuclear activation of the stable isotopes, presented in the irradiated samples, into unstable nuclides with appropriate half-lives. Detecting of the emitted radiation provides quantification of the amount of the newly formed radioactive nuclei. Usually, this technique is being used for the precise determination of a number of main-components and trace elements in different types of unknown samples by means of a well-known neutron source. We use neutron activation analysis "upside down" as we use pure mono-isotopic samples and investigate the unknown neutron field inductive of sample activation.

The rate of nuclear reactions

$$R = n_j \int_0^\infty \phi(E_\mathrm{n})\sigma(E_\mathrm{n})\mathrm{d}E_\mathrm{n} \tag{3.5}$$

is given by the incident neutron flux $\phi(E_\mathrm{n})$, the activation cross-section $\sigma(E_\mathrm{n})$ (the probability of the reaction between neutron of energy $E_\mathrm{n}$ and a target nucleus), and the number of the target nuclei per unit of area $n_j$ (compare eq. (3.5) for "white spectrum" with eq. (3.1) for mono-energetic beam).

Used activation samples were packed into sandwiches compound of $^{27}$Al, $^{197}$Au, $^{209}$Bi, $^{59}$Co (**Fig. 3.16**) and placed in the gaps between sections of the Pb/U-assembly (**Fig. 3.5**). Al-samples had square size of 20×20 mm$^2$ with thickness of 0.4 mm (of ≈ 0.5 g weight), Au-samples had square size of 20×20 mm$^2$ with thickness of 0.04 mm (of ≈ 0.3 g weight), Bi-samples had square size of 25×25 mm$^2$ with thickness of 1 mm (of ≈ 6 g weight), Co-samples had circular size with diameter of 10 mm with thickness of 0.4 mm (of ≈ 3 g weight).

A typical[2] placement of the activation samples is shown in **Fig. 3.5**. The first set of sandwiches was placed at the radial distance $R = 6$ cm from the target axis at five *longitudinal* distances $X = 0.0, 11.8, 24.0, 36.2, 48.4$ cm from the target front (i.e., in front of the target, behind it, and in the gaps between blanket sections). The second set was placed in the gap between the first and second blanket sections (i.e., at the longitudinal distance $X = 11.8$ cm from the target front) at four *radial* distances $R = 3.0, 6.0, 8.5, 10.7$ cm from the target axis. In sum, there were eight sandwiches (one sandwich belongs to both sets).

[2]One can find exceptions, e.g., in the case of 1.5 GeV experiment, the last sandwich of the radial set was placed not at radial distance $R = 10.7$ cm, but at $R = 13.5$ cm; Co-samples were used for 1.5 GeV experiment only; in the case of 2.0 GeV experiment, no samples were placed at $X = 0.0$ cm and $R = 3.0$ etc.

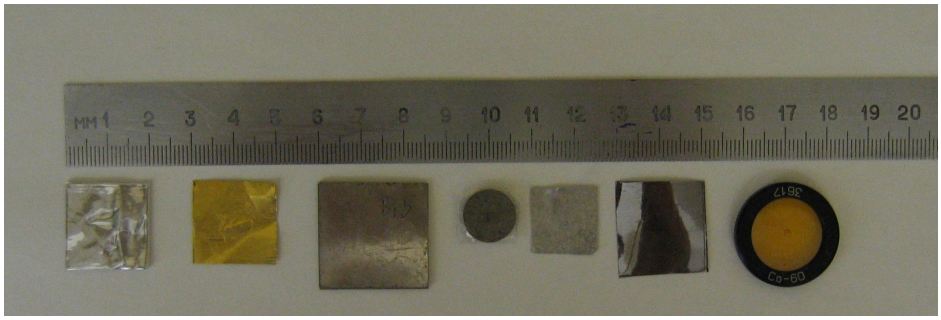


Figure 3.16: Photo of samples used for activation analysis method, from left to right: Al, Au, Bi, Co, In, Ta, and the calibration point-like source of $^{60}$Co.

Neutrons emitted in the course of spallation process in the target caused in the samples non-threshold (n,$\gamma$)-reaction and threshold (n,$\alpha$)-, (n,$x$n)-reactions. We observed the products of threshold reactions with $E_{thresh}$ from 5 to 60 MeV, which correspond to $x$ from 2 up to 9 (**Tables 3.7, 3.8, 3.9**, and **Fig. 3.17, 3.18, 3.19**). The threshold energies were calculated as the difference between outgoing and incoming particles masses (using mass excesses values from [165]). In the case of the $^{27}$Al(n,$\alpha$)$^{24}$Na reaction, the nuclear Coulomb barrier was taken into account and this $E_{thresh}$ was estimated from [166].

The produced isotopes were mainly $\beta$-radioactive. The daughter nucleus of a $\beta$-decay is usually also unstable. To reach a ground state, it has to de-excite by $\gamma$-radiation and electron conversion. Every isotope has characteristic structure of energetic levels. Detecting $\gamma$-transitions between them, it is possible to determine isotope abundance in a sample.

The activities of the irradiated samples were measured off-line by HPGe $\gamma$-spectrometers by Ortec and Canberra companies (Ortec was used for most of the measurements). Our Ortec is a coaxial detector with relative efficiency 28.3% and energy resolution (FWHM of $^{60}$Co at 1.33 MeV) 1.90 keV, Canberra is also coaxial with relative efficiency 18% and energy resolution 1.90 keV. Each sample was measured a few times in order to identify isotopes with different half-lives. The spectrometers were surrounded with robust lead shielding for the reduction of background (**Fig. 3.20**).

Each measured sample was placed to one of eight position (12, 24, 41, 65, 99, 147, 216, 311 mm) from the detector endcap to reach the dead time smaller than 10% (**Fig. 3.21**). The beryllium window is 0.5 mm thick and the distance from the window to the crystal is 3 mm.

Table 3.7: List of threshold and non-threshold reactions observed in Au-samples.

| Reaction | Threshold energy [MeV] | Half-life of product |
|---|---|---|
| $^{197}$Au(n,$\gamma$)$^{198}$Au | - | 2.69517 d |
| $^{197}$Au(n,2n)$^{196}$Au | 8.1 | 6.183 d |
| $^{197}$Au(n,3n)$^{195}$Au | 14.8 | 186.10 d |
| $^{197}$Au(n,4n)$^{194}$Au | 23.2 | 1.584 d |
| $^{197}$Au(n,5n)$^{193}$Au | 30.2 | 17.65 h |
| $^{197}$Au(n,6n)$^{192}$Au | 38.9 | 4.94 h |
| $^{197}$Au(n,7n)$^{191}$Au | 45.7 | 3.18 h |

Table 3.8: List of threshold reactions observed in Bi-samples.

| Reaction | Threshold energy [MeV] | Half-life of product |
|---|---|---|
| $^{209}$Bi(n,4n)$^{206}$Bi | 22.6 | 6.243 d |
| $^{209}$Bi(n,5n)$^{205}$Bi | 29.6 | 15.31 d |
| $^{209}$Bi(n,6n)$^{204}$Bi | 38.1 | 11.22 h |
| $^{209}$Bi(n,7n)$^{203}$Bi | 45.2 | 11.76 h |
| $^{209}$Bi(n,8n)$^{202}$Bi | 54.0 | 1.72 h |
| $^{209}$Bi(n,9n)$^{201}$Bi | 61.4 | 1.8 h |

Table 3.9: List of threshold and non-threshold reactions observed in Al- and Co-samples.

| Reaction | Threshold energy [MeV] | Half-life of product |
|---|---|---|
| $^{27}$Al(n,$\alpha$)$^{24}$Na | 5.5 | 14.959 h |
| $^{59}$Co(n,$\gamma$)$^{60}$Co | - | 5.271 y |
| $^{59}$Co(n,2n)$^{58}$Co | 10.6 | 70.82 d |
| $^{59}$Co(n,3n)$^{57}$Co | 19.4 | 271.79 d |
| $^{59}$Co(n,4n)$^{56}$Co | 30.9 | 77.27 d |
| $^{59}$Co(n,5n)$^{55}$Co | 41.2 | 17.53 h |

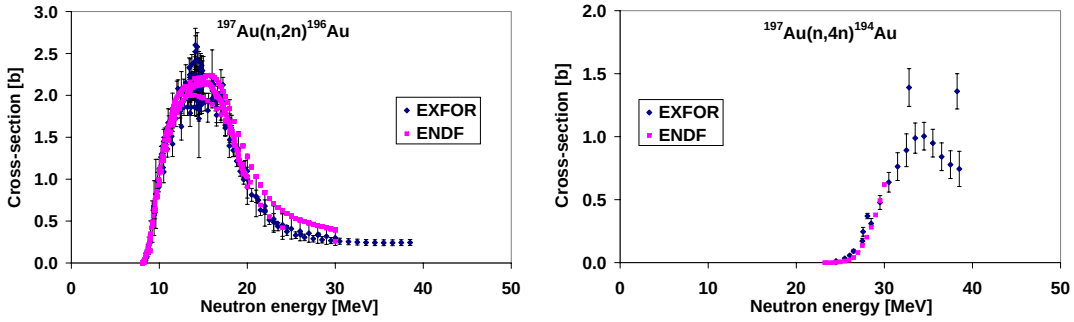


Figure 3.17: Cross-sections of (n,$x$n) reactions in Au. The measured data (from the EXFOR [163] database) were measured by many experimental groups. The evaluated data (from the ENDF [167] database) are shown as well.

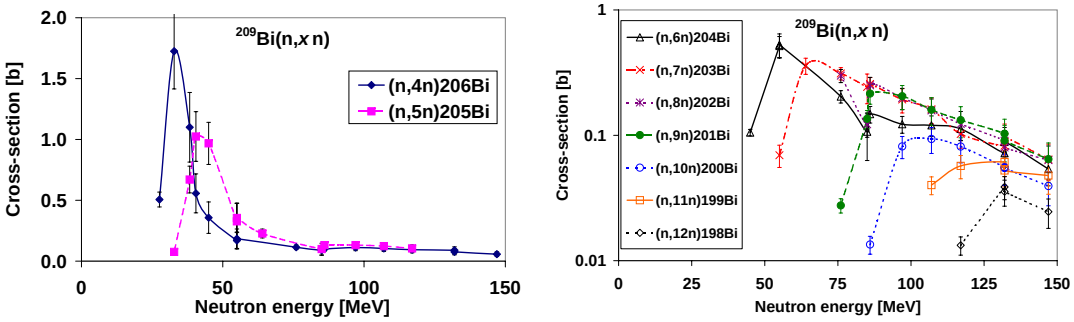


Figure 3.18: Experimental cross-sections of (n,$x$n) reactions in Bi [168].

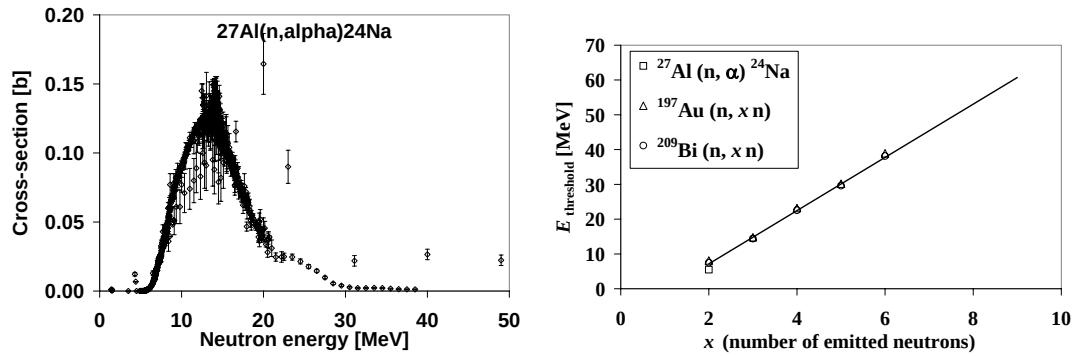


Figure 3.19: EXFOR [163] cross-sections of $^{27}$Al(p,$\alpha$)$^{24}$Na reaction (left). The threshold energies of (n,$x$n) reactions in Al, Au, Bi (right).

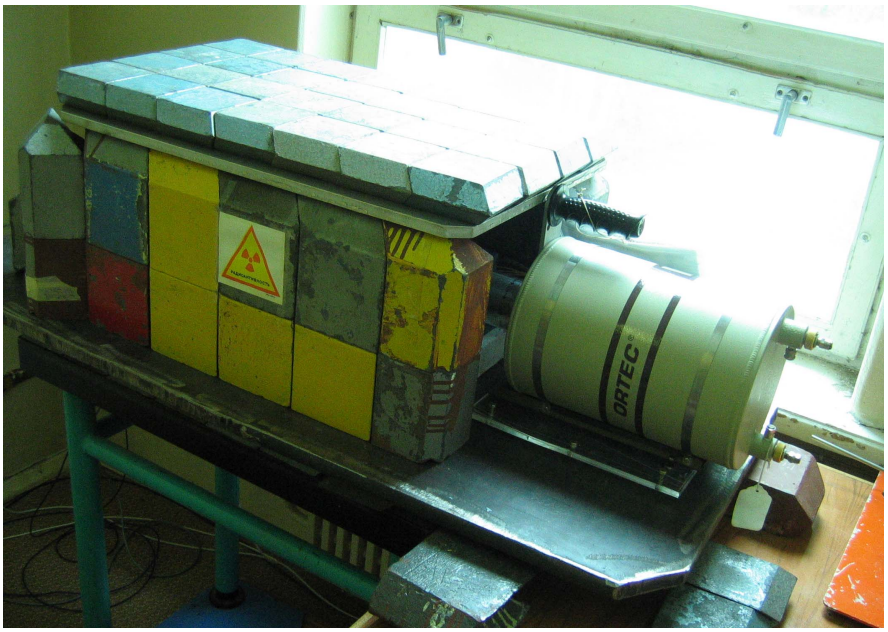


Figure 3.20: HPGe $\gamma$-spectrometer Ortec (with a liquid-nitrogen-filled Dewar flask) surrounded with lead shielding.

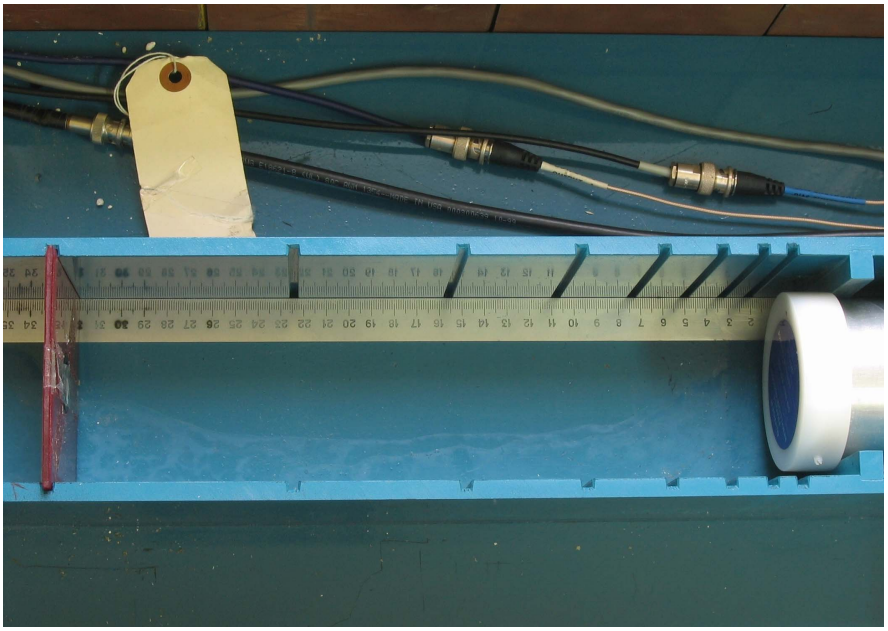

Figure 3.21: A grid with well-defined positions for measured sample placed on a plastic slab.

# Chapter 4

# Data analysis

The measured $\gamma$-spectra of irradiated samples, covering a region approximately from 50 up to 3500 keV, were processed by the DEIMOS32 code [169] that provides a Gaussian fit of $\gamma$-peaks taking into account the background fitted with a parabola (or linear, optionally) (**Fig. 4.1**). The DEIMOS32 output is a table with fitted surfaces of peaks, statistical errors of fits, energies assigned to peak centers, and other data needed in case of ambiguities in results or more detailed investigations, e.g., FWHM, height of subtracted background, number of iterations leading to the resultant fit, $\chi^2$.

## 4.1 Yields of activation reactions and corrections for various effects

The fitted area of peak $S(E)$ is nothing but the number of fully registered $\gamma$-quanta with energy $E$. To enable comparisons of yields of different reactions and yields of the same reactions in different samples, it is necessary to correct the acquired areas for several effects.

- Correction for the intensity of $\gamma$-transition

$$\frac{1}{I_\gamma(E)}. \tag{4.1}$$

  The decay of the excited state of a daughter nucleus can run various ways. The $\gamma$-emission probability $I_\gamma(E)$ is the probability that while decaying, the photon of the energy $E$ is emitted. $I_\gamma(E)$ is given by the nucleus structure and its value is different for different $\gamma$-transitions of the same isotope.

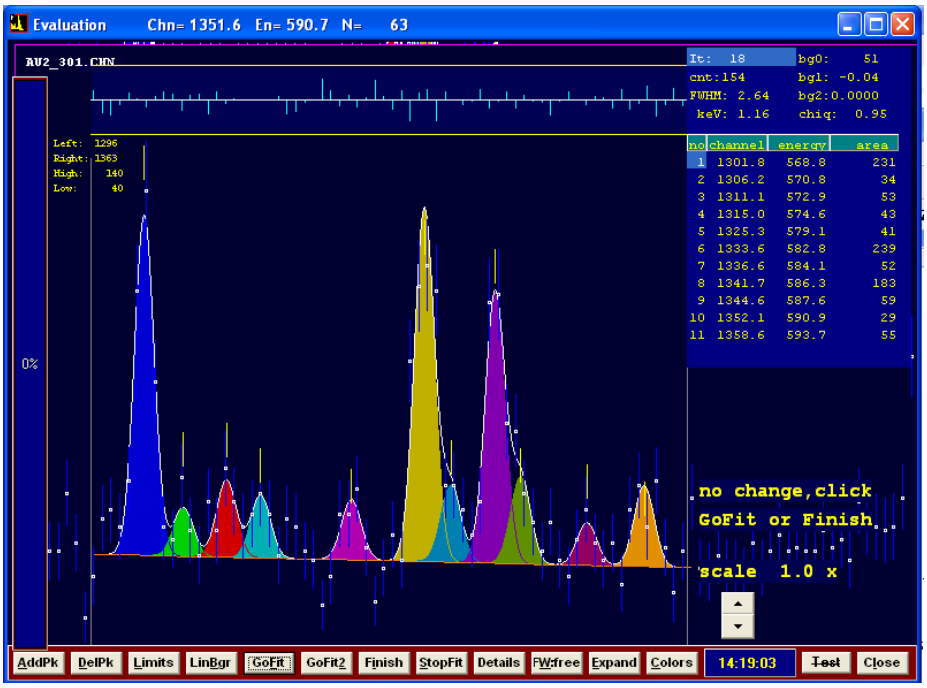


Figure 4.1: Example of fitting procedure in the Deimos32 code.

- Correction for the spectrometer efficiency

$$\frac{1}{\varepsilon_{\mathrm{p}}(E)}. \tag{4.2}$$

The full energy peak efficiency $\varepsilon_{\mathrm{p}}(E)$ is the detector ability to detect the total energy of the $\gamma$-ray with energy $E$. Such impulse is recorded into the full energy peak. Efficiency depends mainly on the distance between a measured sample and a detector and on detector structure (size of an active part, thickness of a passive envelope).The energetic dependence of $\varepsilon_{\mathrm{p}}(E)$ is described in detail in section 4.2.

- Correction for coincidence summing effects

$$\frac{1}{\mathrm{COI}}. \tag{4.3}$$

Coincidence correction factor COI [170] is the correction to possible effect of cascade coincidences, which create a false drop or grow of the fitted peak area $S(E)$. It depends on $\varepsilon_{\mathrm{p}}(E)$, the total efficiency $\varepsilon_{\mathrm{t}}(E)$

(i.e., the detector ability to detect such part of the $\gamma$-ray energy that is bigger than the minimal energy that can be registered by the detector), and the structure of a decay scheme, for details see section 4.2.

- Correction for the detector dead time

$$t_{\text{dead}} = \frac{t_{\text{real}}}{t_{\text{live}}}. \tag{4.4}$$

The dead time is the time when the detector is busy because of reading a signal, recording it into memory, regenerating the sensitive part of detector. During $t_{\text{dead}}$, the detector is not able to register another event if it happens. That means, if the measurement takes $t_{\text{real}}$, the detector was active $t_{\text{live}} < t_{\text{real}}$.

After applying corrections (4.1), (4.2), (4.3), (4.4) we get the number of nuclei decaying during the measurement. To get the number of nuclei produced during the whole period of irradiation, it is necessary to make another corrections yet – for decays during irradiation, cooling, measurement, and for unsteady beam.

- Correction for the decay from the end of irradiation to the end of measurement

$$\frac{\exp(\lambda t_{\text{cool}})}{1 - \exp(-\lambda t_{\text{real}})}, \tag{4.5}$$

where $t_{\text{cool}}$ is time from the end of the irradiation until the beginning of the measurement and $\lambda = \frac{\ln 2}{T_{1/2}}$ is decay constant. According to the decay law, the number of nuclei of decaying isotope in time $t$ is

$$n(t) = n(0)\exp(-\lambda t).$$

Take $n(0)$ as the number of nuclei at the end of irradiation. The number of decays during the measurement is

$$\Delta n = n(t_{\text{cool}}) - n(t_{\text{cool}}+t_{\text{real}}) = n(0)\exp(-\lambda t_{\text{cool}}) - n(0)\exp[-\lambda(t_{\text{cool}}+t_{\text{real}})].$$

Hence, we can express how many times the number of nuclei produced at the end of irradiation is bigger than the number of nuclei decaying during measurement:

$$\frac{n(0)}{\Delta n} = \frac{\exp(\lambda t_{\text{cool}})}{1 - \exp(-\lambda t_{\text{real}})},$$

which is expression (4.5).

- Correction for the decay during irradiation

$$\frac{\lambda t_{\mathrm{irr}}}{1-\exp(-\lambda t_{\mathrm{irr}})}, \tag{4.6}$$

where $t_{\mathrm{irr}}$ is the time of irradiation. The produced nuclei decay during irradiation already. There are not any produced radioactive nuclei at the beginning of irradiation $n(-t_{\mathrm{irr}}) = 0$. The nuclei are being produced during irradiation with a constant rate $P$ and $n(0)$ nuclei remain at its end. The number of produced nuclei at $t < 0$ is given by the differential equation

$$\frac{\mathrm{d}n}{\mathrm{d}t} = P - \lambda n.$$

Its solution can be found by the method of separation of variables

$$\int_{-t_{\mathrm{irr}}}^{0} \mathrm{d}t = \int_{0}^{n(0)} \frac{\mathrm{d}n}{P-\lambda n}.$$

The right side of this equation can be solved using the substitution $u = P - \lambda n$:

$$\int_{0}^{n(0)} \frac{\mathrm{d}n}{P-\lambda n} = \int_{P}^{P-\lambda n(0)} \frac{\mathrm{d}u}{-\lambda u} = -\frac{1}{\lambda} \ln \frac{P-\lambda n(0)}{P}.$$

Then

$$t_{\mathrm{irr}} = -\frac{1}{\lambda} \ln \frac{P-\lambda n(0)}{P}$$

and the production rate can be expressed as

$$P = \frac{\lambda n(0)}{1-\exp(-\lambda t_{\mathrm{irr}})}.$$

Hence, we can express how many times the number of nuclei produced during the whole irradiation is bigger than the number of nuclei that remained at its end:

$$\frac{P t_{\mathrm{irr}}}{n(0)} = \frac{\lambda t_{\mathrm{irr}}}{1-\exp(-\lambda t_{\mathrm{irr}})},$$

which is expression (4.6).

- Correction for beam fluctuations and interruptions during irradiation

$$B_{\mathrm{fluc}} = \frac{1 - \exp(-\lambda t_{\mathrm{irr}})}{t_{\mathrm{irr}} \sum_{i=1}^{N} \{ \frac{w(i)}{t_{\mathrm{p}}(i)} \exp(-\lambda t_{\mathrm{e}}(i)) [1 - \exp(-\lambda t_{\mathrm{p}}(i))] \}}, \tag{4.7}$$

  where $t_{\mathrm{p}}(i)$ is duration of $i$-th interval of irradiation, $t_{\mathrm{e}}(i)$ is time from the end of $i$-th interval until the end of the whole irradiation, $w(i)$ is the weight of $i$-th interval (i.e., the ratio between the number of protons in the $i$-th interval to the total number of protons), $N$ is the number of intervals.

  As it can be seen from **Fig. 3.8**, the approximation of constant beam intensity is not applicable in some cases. Therefore, $t_{\mathrm{irr}}$ was divided into $N$ intervals with constant intensity (each spill was taken as one interval) and duration of $t_{\mathrm{p}}(i) \simeq 10$ s. This correction is important mainly for isotopes that have $T_{1/2} \simeq t_{\mathrm{irr}}$.

- Correction for attenuation of photons in activation sample

$$C_{\mathrm{att}} = \frac{\mu(E_\gamma)\varrho x}{1 - \exp(-\mu(E_\gamma)\varrho x)}, \tag{4.8}$$

  where $\mu(E_\gamma)$ is the total mass attenuation coefficient in units of $\mathrm{cm}^2/\mathrm{g}$ (values taken from [171]). A beam of photons emitted from an activated sample (with density $\varrho$) has to penetrate a relevant part of its thickness $x$ and is attenuated. The self-absorption correction was mostly negligible, for thick samples and low energies it reached up to 14%.

- It is useful to normalize the number of produced nuclei per unit of sample mass $m$ and per one beam particle:

$$\frac{1}{m I_{\mathrm{p}}}, \tag{4.9}$$

  where $I_{\mathrm{p}}$ is the total beam flux.

After inclusion of all corrections (4.1)–(4.9), we get the relation between the peak area $S(E)$ and the total number of produced nuclei (of each produced isotope) per one gram of activated material and per one incident proton:

$$N_{\mathrm{yield}} = \frac{S_\gamma(E)}{I_\gamma(E)\varepsilon_{\mathrm{p}}(E)\mathrm{COI}} \frac{t_{\mathrm{real}}}{t_{\mathrm{live}}} \frac{B_{\mathrm{fluc}} C_{\mathrm{att}}}{m I_{\mathrm{p}}} \frac{\exp(\lambda t_{\mathrm{cool}})}{[1 - \exp(-\lambda t_{\mathrm{real}})]} \frac{\lambda t_{\mathrm{irr}}}{[1 - \exp(-\lambda t_{\mathrm{irr}})]}. \tag{4.10}$$

This relation was used in analysis of $\gamma$-spectra of all activation samples.

## 4.2 Detector efficiency calibration

The calibration of detector efficiency was performed with the use of standard calibration point-like sources (dimensions in order of tenths of mm, see **Fig. 3.16**): $^{133}$Ba, $^{139}$Ce, $^{57}$Co, $^{60}$Co, $^{137}$Cs, $^{152}$Eu, $^{154}$Eu, $^{54}$Mn, $^{226}$Ra (and its daughter product $^{214}$Bi), $^{113}$Sn, $^{228}$Th (and its daughter products $^{224}$Ra, $^{220}$Rn, $^{212}$Pb, $^{212}$Bi, $^{208}$Tl), $^{88}$Y; with several $\gamma$-lines ranging from 80 keV up to 2600 keV, see **Table 4.1**.

Several types of efficiencies are commonly used in $\gamma$-spectroscopy:

- **total (absolute) efficiency**

$$\varepsilon_{\mathrm{t}}(E) = \frac{\text{the number of counts (of any size) produced by the detector}}{\text{the number of } \gamma\text{-rays emitted by the source}};$$

- **intrinsic efficiency**

$$\varepsilon_{\mathrm{in}}(E) = \frac{\text{the number of counts produced by the detector}}{\text{the number of } \gamma\text{-rays striking the detector}};$$

- **relative efficiency** - efficiency of one detector relative to another, commonly

$$\varepsilon_{\mathrm{rel}}(E) = \frac{\text{efficiency of the detector}}{\text{efficiency of a NaI crystal (diameter and length of 7.62 cm)}},$$

each at 25 cm from a point source with 1333 keV (line of $^{60}$Co);

- **full energy peak (photopeak) efficiency**

$$\varepsilon_{\mathrm{p}}(E) = \frac{\text{the number of full energy peak counts produced by the detector}}{\text{the number of } \gamma\text{-rays emitted by the source}}.$$

We need to know $\varepsilon_{\mathrm{t}}(E)$ and $\varepsilon_{\mathrm{p}}(E)$.

If a standard emits $N_{\mathrm{real}}(E)$ photons with energy $E$ and $N_{\mathrm{FEP}}(E)$ photons are fully registered, $\varepsilon_{\mathrm{p}}(E)$ can be determined as

$$\varepsilon_{\mathrm{p}}(E) = \frac{N_{\mathrm{FEP}}(E)}{N_{\mathrm{real}}(E)}. \tag{4.11}$$

If $T$ is time between the reference date (when the calibration standard had activity $A_0$) and the beginning of measurement, the number of photons emitted with energy $E$ can be calculated as

$$N_{\mathrm{real}}(E) = I_\gamma(E) \int_T^{T+t_{\mathrm{real}}} A_0 \exp(-\lambda t)\mathrm{d}t = I_\gamma(E)\frac{1}{\lambda}A_0 \exp(-\lambda T)[1-\exp(-\lambda t_{\mathrm{real}})], \tag{4.12}$$

If $t_{\mathrm{real}} \ll T_{1/2}$, we can replace the exponential function $\exp(-\lambda t_{\mathrm{real}})$ by first two terms of the Taylor series

$$\exp(-\lambda t_{\mathrm{real}}) \doteq 1 - \lambda t_{\mathrm{real}} \tag{4.13}$$

and the formula (4.12) can be simplified with good enough accuracy as

$$N_{\mathrm{real}}(E) = I_\gamma(E) A_0 t_{\mathrm{real}} \exp(-\lambda T). \tag{4.14}$$

### 4.2.1 The effect of $\gamma$-$\gamma$ cascade coincidences

The formula (4.11) is valid on ideal conditions only, when all counts in full energy peak correspond to the registration of photon of appropriate $\gamma$-transition.

Consider a simple decay scheme as in **Fig. 4.2**. In first approximation, it is possible to take the directions of photons in a cascade (B+C) as independent. The probability that both photons hit the active part of detector is nonzero and increases with decreasing distance of a sample from detector (as detector occupies bigger space angle). Moreover, typical lifetimes of nuclear levels ($\sim$ 10 ps) are a few orders of magnitude shorter than time resolution of HPGe detectors ($\sim$ 10 ns) and two or more photons of one cascade can be registered at the same time. This is called $\gamma$-$\gamma$ **cascade coincidence**.

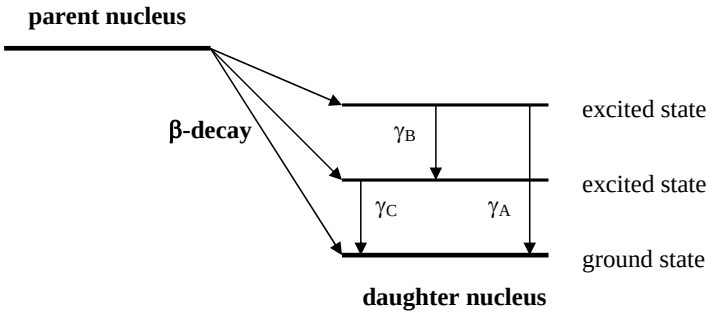


Figure 4.2: A simple decay scheme.

If photons B and C are registered together, the electric pulse is recorded into a **sum peak** B+C. If transition A=B+C really exists, the area of corresponding peak (i.e., the number of pulses in it) is then bigger than it should

Table 4.1: Energies and emission probabilities of the used calibration standards (data extracted from [38]).

| Isotope | $T_{1/2}$ [y] | $E_\gamma$ [keV] | $I_\gamma$ [%] | Isotope | $T_{1/2}$ [y] | $E_\gamma$ [keV] | $I_\gamma$ [%] |
|---|---|---|---|---|---|---|---|
| $^{152}$Eu | 13.537 | 121.8 | 28.37 | $^{137}$Cs | 30.07 | 661.7 | 85.1 |
| | | 244.7 | 7.53 | $^{228}$Th | 1.9116 | 238.6 | 43.5 |
| | | 295.9 | 0.91 | | | 241.1 | 4.10 |
| | | 344.3 | 26.57 | | | 277.4 | 2.30 |
| | | 367.8 | 0.92 | | | 300.1 | 3.28 |
| | | 411.1 | 2.86 | | | 549.8 | 0.114 |
| | | 778.9 | 12.92 | | | 583.2 | 30.6 |
| | | 867.4 | 4.92 | | | 727.3 | 6.58 |
| | | 964.1 | 14.61 | | | 860.6 | 4.50 |
| | | 1085.8 | 10.21 | | | 1620.7 | 1.49 |
| | | 1089.7 | 1.73 | | | 2614.5 | 35.86 |
| | | 1112.1 | 13.00 | $^{60}$Co | 5.2714 | 1173.2 | 99.97 |
| | | 1212.9 | 1.42 | | | 1332.5 | 99.98 |
| | | 1299.1 | 1.63 | $^{57}$Co | 0.7446 | 122.1 | 85.60 |
| | | 1408.0 | 21.01 | | | 136.5 | 10.68 |
| $^{154}$Eu | 8.593 | 123.1 | 40.79 | $^{226}$Ra | 1600 | 186.2 | 3.59 |
| | | 247.9 | 6.95 | | | 242.0 | 7.12 |
| | | 591.8 | 4.99 | | | 295.2 | 18.2 |
| | | 723.3 | 20.22 | | | 351.9 | 35.1 |
| | | 756.8 | 4.57 | | | 609.3 | 44.6 |
| | | 873.2 | 12.27 | | | 768.4 | 4.76 |
| | | 996.3 | 10.6 | | | 934.1 | 3.07 |
| | | 1004.8 | 18.01 | | | 1120.3 | 14.7 |
| | | 1274.4 | 35.19 | | | 1238.1 | 5.78 |
| | | 1596.5 | 1.80 | | | 1764.5 | 5.78 |
| $^{133}$Ba | 10.51 | 81.0 | 34.06 | | | 2118.6 | 1.17 |
| | | 276.4 | 7.16 | | | 2201.1 | 4.98 |
| | | 302.9 | 18.33 | | | 2447.7 | 1.55 |
| | | 356.0 | 62.05 | $^{54}$Mn | 0.855 | 834.8 | 100.0 |
| | | 383.8 | 8.94 | $^{139}$Ce | 0.377 | 165.9 | 79.87 |
| $^{88}$Y | 0.292 | 898.0 | 93.70 | $^{113}$Sn | 0.315 | 391.7 | 64.89 |
| | | 1836.1 | 99.20 | | | | |

be ($\gamma$-$\gamma$ coincidence summing). Likewise, the areas of peaks B and C are smaller ($\gamma$-$\gamma$ coincidence loss). The measured numbers of pulses must be corrected with respect to these effects.

The *net* area of peak A is proportional to the product of the $\gamma$-emission probability and full energy peak efficiency

$$N_{\mathrm{net}}(\mathrm{A}) \sim I_\gamma(\mathrm{A})\varepsilon_{\mathrm{p}}(\mathrm{A}). \tag{4.15}$$

The area of sum peak B+C is proportional to the product of the emission probability of the first transition $I_\gamma(\mathrm{B})$, branching ratio to the second transition $a(\mathrm{C})$, probability $c(\mathrm{C})$ that real photon is emitted when the second transition occurs (instead of electron conversion), and full energy peak efficiencies of both photons $\varepsilon_{\mathrm{p}}(\mathrm{B})$ and $\varepsilon_{\mathrm{p}}(\mathrm{C})$

$$N(\mathrm{B{+}C}) \sim I_\gamma(\mathrm{B})a(\mathrm{C})c(\mathrm{C})\varepsilon_{\mathrm{p}}(\mathrm{B})\varepsilon_{\mathrm{p}}(\mathrm{C}). \tag{4.16}$$

The quantity $c(\mathrm{C})$ equals

$$c(\mathrm{C}) = \frac{1}{\alpha(\mathrm{C}) + 1}, \tag{4.17}$$

where $\alpha(\mathrm{C})$ is the conversion coefficient of transition C.

The probability for $\gamma$-$\gamma$ **coincidence summing** A=B+C can be calculated as the ratio of area of sum peak B+C to area of net peak A

$$S(\mathrm{A}) = \frac{I_\gamma(\mathrm{B})}{I_\gamma(\mathrm{A})} a(\mathrm{C})c(\mathrm{C}) \frac{\varepsilon_{\mathrm{p}}(\mathrm{B})\varepsilon_{\mathrm{p}}(\mathrm{C})}{\varepsilon_{\mathrm{p}}(\mathrm{A})}. \tag{4.18}$$

The measured areas of peaks B and C are smaller than they should be due to $\gamma$-$\gamma$ coincidence losses[1]. The probability for $\gamma$-$\gamma$ **coincidence loss** of area of peak B can be calculated as the product of the probability that transition B is followed by radiative transition C $a(\mathrm{C})c(\mathrm{C})$ and probability that detector registers any part of energy of photon C that is bigger than its resolution $\varepsilon_{\mathrm{t}}(\mathrm{C})$

$$L(\mathrm{B}) = a(\mathrm{C})c(\mathrm{C})\varepsilon_{\mathrm{t}}(\mathrm{C}). \tag{4.19}$$

The coefficient for $\gamma$-$\gamma$ coincidence loss of area of peak C may be derived in an analogous way

[1] In principle, any physically possible energy deposition, which originates from a cascading photon, causes a coincidence loss, i.e., counts in: full energy peak, Compton continuum, single and double escape peaks, backscatter peak, 511 keV peak, X-ray peaks from surrounding material (especially Pb KX-rays), Ge KX escape peak, etc.

$$L(\mathrm{C}) = \frac{I_\gamma(\mathrm{B})}{I_\gamma(\mathrm{C})} a(\mathrm{C}) c(\mathrm{C}) \varepsilon_\mathrm{t}(\mathrm{B}). \tag{4.20}$$

These formulas can be generalized for the sake of multiple cascades (e.g., A=D+E+F). Correction coefficients for cascade transitions of higher orders can be found in [170].

Some decay schemes are very complicated and peak areas should be corrected for both coincidence summations $S(E)$ and coincidence losses $L(E)$. Using both correction factors, the measured number of pulses in full energy peak of energy $E$ is

$$N_\mathrm{FEP}(E) = N(E) - N(E)L(E) + N(E)S(E) - L(E)S(E)N(E). \tag{4.21}$$

The correct number of pulses originated from the net transition of energy $E$ is

$$N(E) = \frac{N_\mathrm{FEP}(E)}{\mathrm{COI}}, \tag{4.22}$$

where COI is **coincidence correction factor**

$$\mathrm{COI} = [1 - L(\mathrm{A})][1 + S(\mathrm{A})], \tag{4.23}$$

which depends on $\varepsilon_\mathrm{p}(E)$ and $\varepsilon_\mathrm{t}(E)$. Their determination is described in the following two sections.

Besides *true* $\gamma$-$\gamma$ cascade coincidences, *random* coincidences can occur as well. But they make contribution smaller than 1% in the nearest used geometry (checked for $^{57}$Co lines 122.1 and 136.5 keV, which belong to transitions from the same level, therefore, they cannot truly coincide). The influence of random coincidences were not taken into account.

### 4.2.2 Determination of $\varepsilon_\mathrm{t}(E)$

Total efficiency $\varepsilon_\mathrm{t}(E)$ equals the sum of efficiencies of all particular processes leading to any registerable loss of photon energy (photoefect, Compton scattering, pair creation). For a calibration standard with known activity holds

$$\varepsilon_\mathrm{t}(E) = \frac{N_\mathrm{tot} - N_\mathrm{back}}{N_\mathrm{real}(E)}, \tag{4.24}$$

where $N_\mathrm{tot}$ is the total number of registered pulses (from calibration source), $N_\mathrm{back}$ is the number of pulses from another sources (background radiation, detector noise); all $N_i$ in eq. (4.24) are per second. Using eq. (4.11) and

(4.24) it is possible to calculate the photofraction [172] (or peak-to-total ratio)

$$R(E) = \frac{\varepsilon_{\mathrm{p}}(E)}{\varepsilon_{\mathrm{t}}(E)} = \frac{N_{\mathrm{FEP}}(E)}{N_{\mathrm{tot}} - N_{\mathrm{back}}}. \tag{4.25}$$

Values of photofraction can be determined using standards with two or even better one transitions only. We used $^{139}$Ce (165.9 keV), $^{137}$Cs (661.7 keV), $^{54}$Mn (834.8 keV); $^{88}$Y (two well separable peaks 898.0 and 1836.1 keV); $^{57}$Co (using assumption that $R$ changes linearly in log-log scale in a small interval 122.1–136.5 keV, these two near peaks were replaced by a fictive peak 123.7 keV with energy equal to the weighted average and area equal to the sum of both peaks), $^{60}$Co (similarly, near peaks 1173.2 and 1332.5 keV were replaced by 1252.9 keV).

The obtained values of $R(E)$ were fitted with a polynomial function of the third order in logarithmic scale

$$R(E) = \exp[a \ln^3(E) + b \ln^2(E) + c \ln(E) + d], \tag{4.26}$$

where the fitted constants $a$, $b$, $c$, $d$ for used geometries (four different distances between sample and detector were used) can be found in **Table 4.2**. The curves of $\varepsilon_{\mathrm{t}}(E)$ are plotted in **Fig. 4.3**.

Table 4.2: Coefficients of photofraction $R$ (from eq. (4.26)).

| geometry | $a$ | $b$ | $c$ | $d$ |
|---|---|---|---|---|
| position 2 | 0.0546 | 0.113 | 0.114 | 0.106 |
| position 3 | -0.793 | -1.866 | -2.30 | -1.80 |
| position 4 | 2.95 | 9.52 | 12.4 | 9.47 |
| position 5 | -2.12 | -15.7 | -22.2 | -16.4 |

Table 4.3: Coefficients of full-energy peak efficiency $\varepsilon_{\mathrm{p,fit}}(E)$ and split parameters $E_{split}$ (from eq. (4.28)).

| geometry | $q_0$ | $q_1$ | $q_2$ | $q_3$ | $E_{split}$ | $k_0$ | $k_1$ |
|---|---|---|---|---|---|---|---|
| position 2 | 0.221 | -3.72 | 19.8 | -35.7 | 330 | 2.25 | -0.906 |
| position 3 | 0.0558 | -1.04 | 5.42 | -11.0 | 650 | 1.31 | -0.867 |
| position 4 | 0.114 | -2.09 | 11.8 | -24.7 | 715 | 0.706 | -0.872 |
| position 5 | 0.131 | -2.37 | 13.4 | -28.3 | 530 | 0.133 | -0.880 |

### 4.2.3 Determination of $\varepsilon_{\mathrm{p}}(E)$

Full energy peak efficiency can be determined as

$$\varepsilon_{\mathrm{p}}(E) = \frac{N(E) - N_{\mathrm{back}}}{N_{\mathrm{real}}(E)}. \tag{4.27}$$

According to formula (4.22), $N(E)$ depends on COI that depends on $\varepsilon_{\mathrm{p}}(E)$. Therefore, eq. (4.27) was solved by the iteration method. In each step of iteration, $\varepsilon_{\mathrm{p,exp}}(E)$ was calculated using the peak areas of measured calibration standards $N_{\mathrm{FEP}}(E)$. The obtained values for each geometry were fitted with a curve (for different ranges with a polynomial function of the third order and with a linear function; both in logarithmic scale)

$$\varepsilon_{\mathrm{p,fit}}(E) = \exp \sum_{j=0}^{3} q_j \ln^j E \quad \text{for} \quad E < E_{split}, \tag{4.28}$$

$$\varepsilon_{\mathrm{p,fit}}(E) = \exp \sum_{i=0}^{1} k_i \ln^i E \quad \text{for} \quad E \geq E_{split}. \tag{4.29}$$

The parameter $E_{split}$ was chosen to divide the spectrum into two parts that enable better fit of the dependence (but it does not have any physical meaning). Its values for each used geometry can be found in **Table 4.3**. In the first step of iteration, cascade effects were not taken into account until this point.

Then COI factors (formula (4.23)) were calculated for each transition of calibration standards using the fitted dependencies $R(E)$ (eq. (4.26)) and $\varepsilon_{\mathrm{p,fit}}(E)$ (eq. (4.28), (4.29)). The calculated COI factors were used for correction of experimental activities (eq. 4.22) and new iteration followed.

The iteration was repeated until the differences between coefficients $q_j$ and $k_i$ in two successive steps were less than 1% (usually 4–5 steps). The resultant values of coefficients can be found in **Table 4.3**. Calibration curves for each used geometry are shown in **Fig. 4.3**.

The courses of $\varepsilon_{\mathrm{p}}(E)$ correspond to expected shape. The efficiency is low for small $E_\gamma$, because such photons can be absorbed in the entrance window and hardly penetrate into detector active part. Initially, $\varepsilon_{\mathrm{p}}(E)$ increases with increasing energy and reach maximum around 100 keV. Then $\varepsilon_{\mathrm{p}}(E)$ slowly decrease with increasing energy, because the more energetic photons are the more of them fly through detector active part without occurring photoeffect.

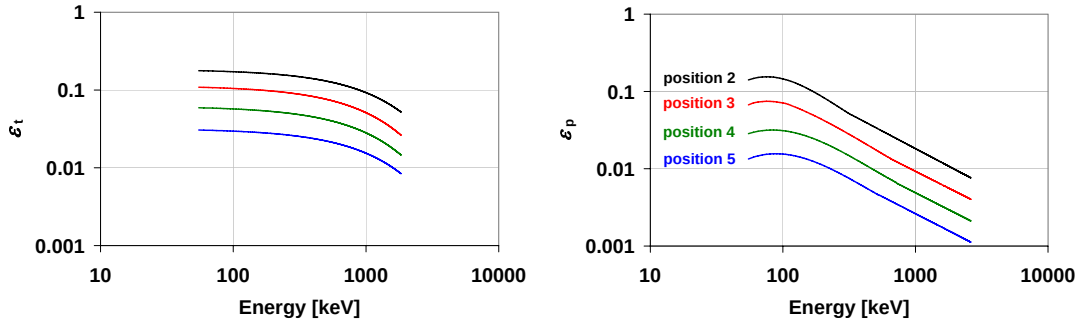


Figure 4.3: The curves of total efficiency $\varepsilon_t(E)$ for each measured geometry (left). Calibration curves of full peak efficiency $\varepsilon_p(E)$ for each measured geometry (right). The efficiencies decrease with increasing distance sample–detector.

### 4.2.4 The influence of nonzero dimensions of activation samples

While the efficiency calibration was done using point-like calibration sources, the measured activation samples had square size of dimensions of approximately 2 cm × 2 cm (**Fig. 3.16**). This can bring into some systematic error. Therefore, the measurement to estimate the importance of this circumstance was carried out.

The calibration was re-measured with two samples of standard calibration source of $^{152}$Eu (**Table 4.1**). One sample was point-like and one sample had circular shape with diameter 2 cm, which sufficiently imitated the size of usually used activation samples.

There are eight slots for sample holders. The closest position is No. 1, the second closest is No. 2, ..., the furthest is No. 8 (**Fig. 4.4**). The measurements were taken in six geometries (from 2 until 7), in which the activation samples are usually being measured.

The efficiencies measured with a point-like source and surface source give for all measured positions the same values within error bars, which include statistical uncertainties and uncertainties of the absolute activities of the point-like and surface calibration sources (1.6% and 5%, respectively), see **Fig. 4.5**.

I conclude that nonzero dimensions of the used activation samples have negligible influence and it is not necessary to take it into account in our case. Monte-Carlo simulations predict [173] that the efficiency is bigger for point-like source than for the surface one by a factor of 5% in the position number 2 and less for farther positions, which is not in contradiction with the experimental results.

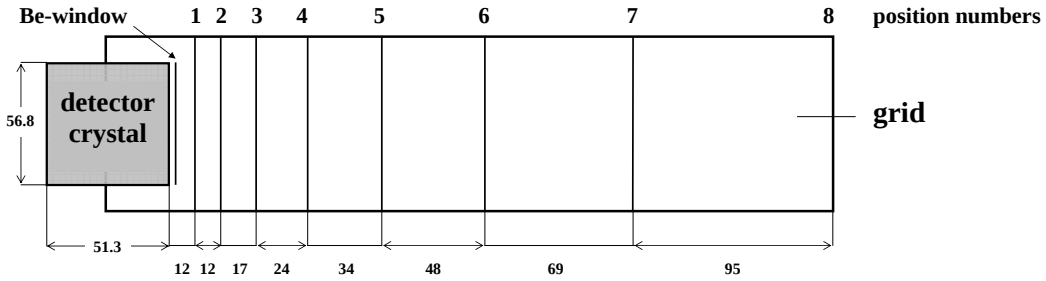


Figure 4.4: The scheme of the grid for foil holders with marked positions. Dimensions are in millimeters.

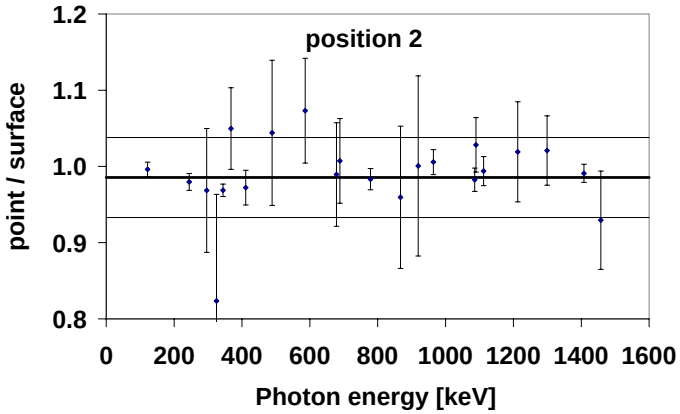


Figure 4.5: Ratios between efficiency given by a point-like source and a surface source as a function of an energy for the position number 2 (the closest used). The error bars of the points are of statistical origin. The thick solid line is weighted average over the whole energy range, the thin solid lines represent uncertainties that include statistical uncertainties and uncertainties of the absolute activities of both calibration sources.

# Chapter 5

# Experimental results

## 5.1 Yields of activation reactions

The yields (4.10) of radioactive isotopes produced in activation samples in units of [$g^{-1}$ $proton^{-1}$] are presented on example of the 1.5 GeV experiment in **Fig. 5.1**. The trends are practically identical for all four proton experiments, see Appendix B.

The dependencies of yields on the position along the target are given on the left side, dependencies of yields on the radial distance from the target axis are given on the right side of the figures. The delineated errors (hardly visible at this scale) are only of statistical origin (given by the error of the Gaussian fit of $\gamma$-peaks). Experimental errors, mainly the inaccuracies of the beam and activation foils displacements, beam intensity, and $\gamma$-spectrometer efficiency determinations can contribute up to 30% [97], which mainly change the absolute values and less the shape of yield spatial distributions.

The yields of threshold reactions (the list of them can be found in **Tables 3.7, 3.8, 3.9**) appear to have similar shapes.

- The *radial* distributions of the yields of all isotopes produced in threshold reactions decrease as the intensity of spallation part of neutron spectra falls down with increasing perpendicular distance from the target (beam) axis.

- The *longitudinal* distributions of the yields of all isotopes produced in threshold reactions change for one order of magnitude and have clear maximum observed in the first gap between blanket sections.

  While, the neutron field around the setup is a complicated mixture of spallation, fission, moderated and back-scattered neutrons, the isotopes generated in threshold reactions are produced mainly by neutrons

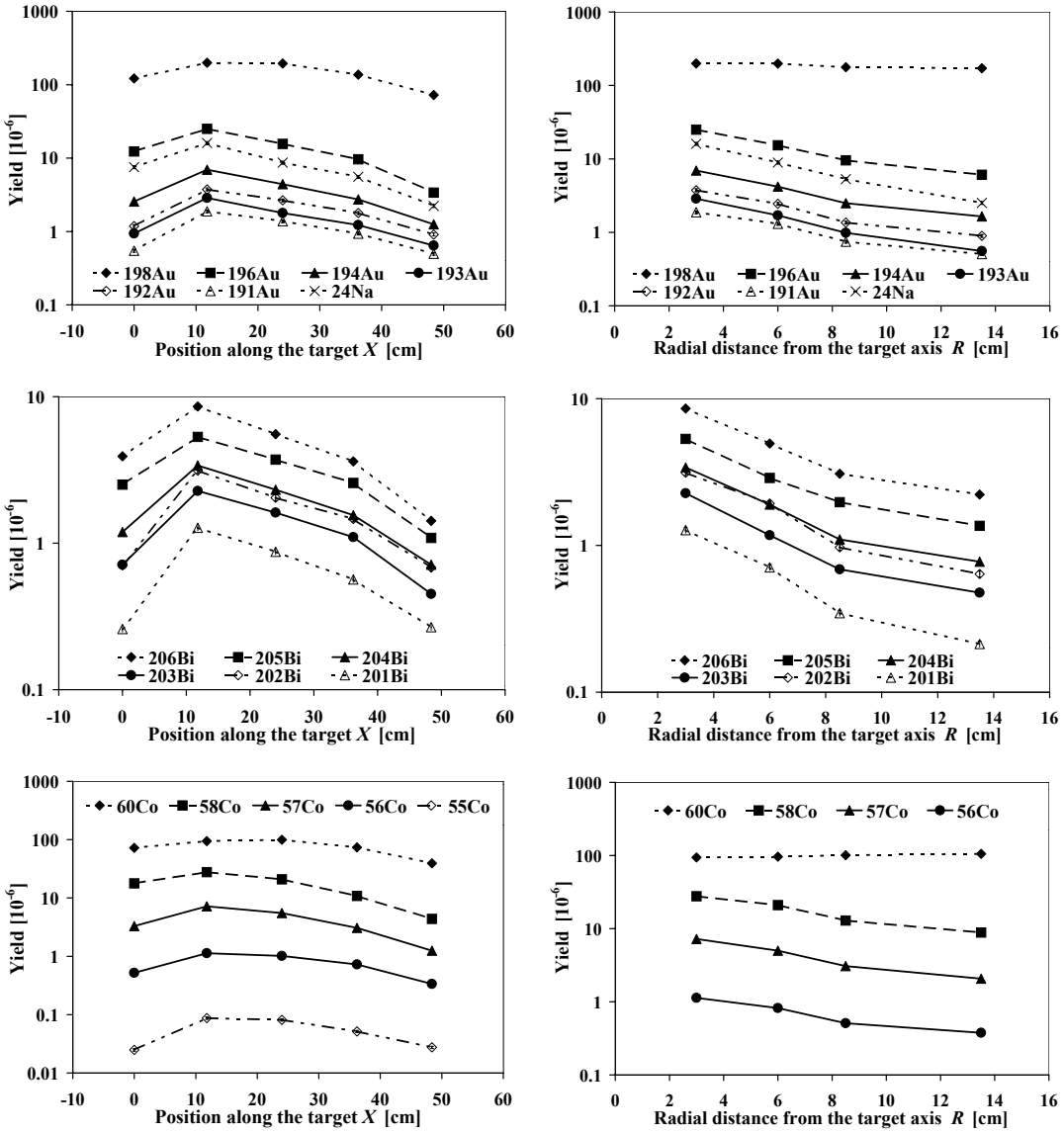


Figure 5.1: Longitudinal (left) and radial (right) distributions of the experimental yields of nuclei produced in Al, Au, Bi, and Co samples (example of 1.5 GeV experiment). The lines linking experimental points are delineated to guide readers' eyes.

isotropically evaporated in spallation reactions. Thus, one could expect the maximum in the centre of the target. But the shape of the longitudinal distribution reflects the interplay of two main processes. First, the spallation cross-section of protons decreases along the target in relation with the decrease in the primary proton energy due to the ionisation losses. Second, the intensity of the primary proton beam decreases as well as protons interact with the target by spallation. Consequently, the maximum intensity of the fast neutron field is shifted from the centre to the target's front.

The yields of nuclei produced in neutron capture reactions (listed in **Tables 3.7, 3.9**) show different shape.

- The *radial* distributions of $^{198}$Au and $^{60}$Co are almost constant. The reason for such behaviour is the polyethylene shielding that moderates high-energy neutrons outgoing from the setup at first and then partly scatters low-energy neutrons back. Herewith, the moderator creates an intensive homogeneous field of low-energy neutrons (**Fig. 3.7**) that is predominant in production of $^{198}$Au and $^{60}$Co. Therefore, the radial distributions of these isotopes are constant.

- The *longitudinal* distributions of $^{198}$Au and $^{60}$Co are mainly influenced by the polyethylene shielding as well. However, the contribution of low-energy neutrons from moderator is decreased in front of the target and behind it, because the target/blanket is not shielded from front and back ends, see **Fig. 1.15**. Therefore, the yields of $^{198}$Au and $^{60}$Co are lower in these positions.

## 5.2 Changes of yields in dependence on threshold energy

Ratios between yields at the end of the target and in front of it as a function of reaction threshold energy are shown in **Fig. 5.2** left. These ratios increase with increasing threshold energy. This indicates that the resulting neutron spectrum becomes harder at the end of the target than at its forepart. Differences between sample materials are probably due to different energy cross-sections dependencies.

Ratios between yields at $R = 3.0$ cm and at $R = 13.5$ cm as a function of reaction threshold energy are shown on the right side of **Fig. 5.2**. In contrast to the latter, these ratios are almost independent on threshold energy. This is the sign that the shapes of fast neutron spectra are similar in both positions.

I studied this phenomenon using MCNPX simulations as well, see section 6.1.1.

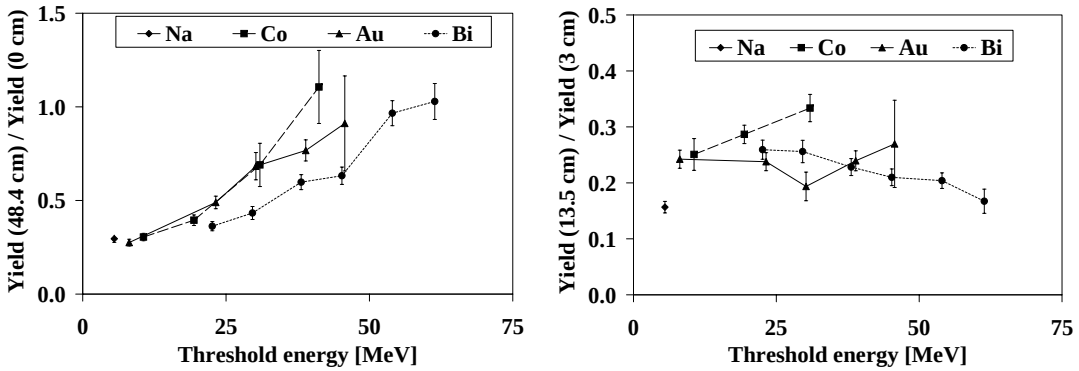


Figure 5.2: Ratios of yields at the end of target ($X = 48.4$ cm) and in front of the target ($X = 0$ cm) and as a function of reaction threshold energy (left). Ratios of yields at $R = 13.5$ cm and at $R = 3.0$ cm as a function of reaction threshold energy (right). The lines link points belonging to one element. Example of 1.5 GeV experiment.

# Chapter 6

# Simulations

The Monte-Carlo simulations of neutron production in the E+T setup and activation reactions in the samples were performed by the MCNPX code version 2.6.C [104]. The influence of possible inaccuracies in the description of the E+T setup geometry (**Fig. 6.1**) on the produced neutron field is negligible [97].

Now, let me to recall the possibilities of description of spallation reaction available in MCNPX 2.6.C (for details, see sections 1.2, 2.2):

- the intra-nuclear cascade (INC) stage can be described with the Bertini INC model (default in MCNPX), Isabel INC model, Liège INC model (so-called INCL4), or CEM03 model (which works alone);
- the Multistage Pre-equilibrium Exciton Model is model of pre-equilibrium emission of particles (only nucleons, photons, and charged pions were taken into account in author's simulations), which is included in the Bertini and Isabel INC models and can be switched on/off; the CEM03 model uses its own pre-equilibrium model (the improved Modified Exciton Model) without user-possibility to adjust it; the Liège INC model does not include any pre-equilibrium model;
- the equilibrium emission of particles can be described with Dresner (default for Bertini and Isabel INC) or ABLA (default for Liège INC) evaporation models.

Hereafter, I use following abbreviations when mentioning various combinations of the models: B stands for Bertini INC model, I stands for Isabel INC model, L stands for Liège INC model, CEM stands for CEM03 model, D stands for Dresner evaporation model, A stands for ABLA evaporation model.

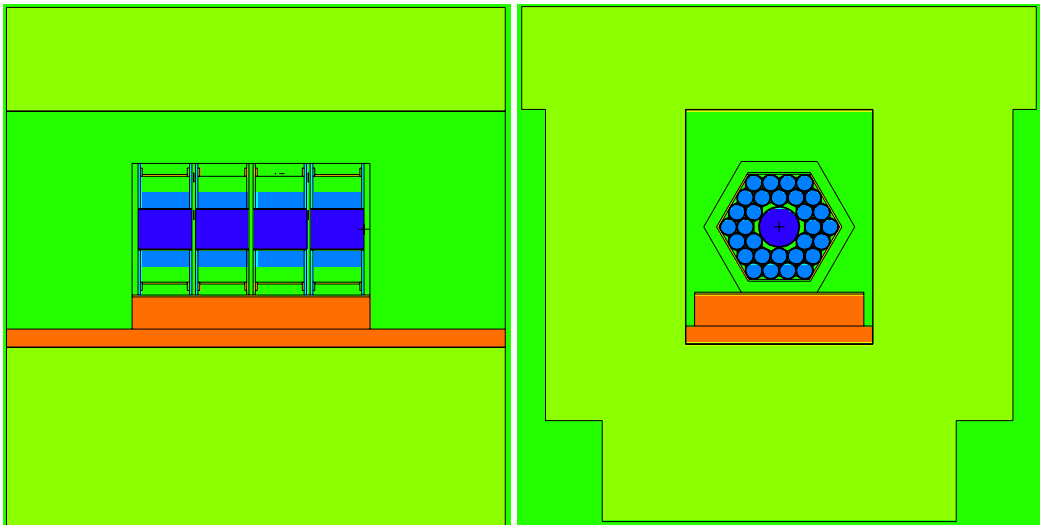

Figure 6.1: Cross-sectional side view (left) and front view (right) of the E+T setup description in MCNPX (MCNPX plot). Compare with **Fig. 1.15**.

I used the LA150 data library [132] as the source of evaluated cross-sections.

When simulating neutron spectra and yields of activation reactions, I simulated from $1 \times 10^6$ to $1 \times 10^7$ events in each case. When simulating neutron multiplicity, I simulated 20000 events in each case, which corresponds to the relative uncertainty $\approx 0.7\%$.

## 6.1 Neutron spectra simulations

### 6.1.1 The influence of physics models on simulated spectra

At first, I used the default option Bertini+Dresner for simulations of the produced neutron spectra $\Phi_n(E)$ (using the F4 tally). The simulations show that neutron spectrum is harder at the end of target when compared to its beginning (left side of **Fig. 6.2**) and that neutron spectrum has similar shape inside target as well as farther from it (right side of **Fig. 6.2**). We drew the same conclusion from the experimental results, see **Fig. 5.2**.

Then, I used all combinations of INC+evaporation models available in MCNPX 2.6.C. The upper part of **Fig. 6.3** shows an example of neutron spectra simulation (produced in the 1.0 GeV experiment), the lower part of **Fig. 6.3** shows their ratios.

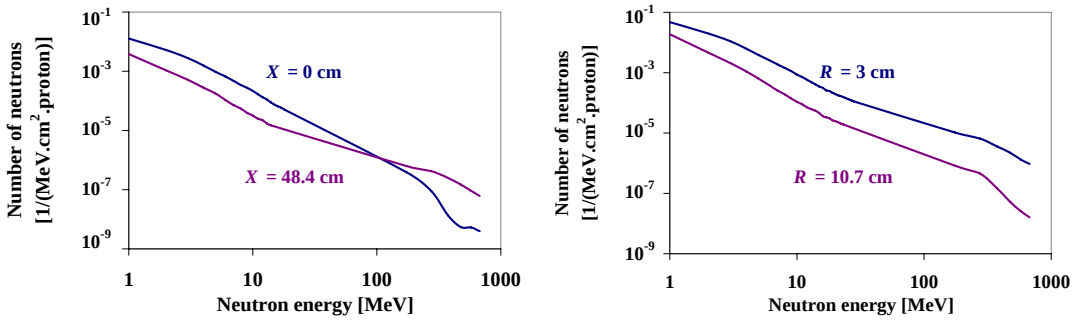


Figure 6.2: Neutron spectra (in log-log scale) in front of ($X = 0$ cm) and behind ($X = 48.4$ cm) target, both at $R = 3$ cm (left). Neutron spectra inside target ($R = 3$ cm) and farther from target ($R = 10.7$ cm), both at $X = 11.8$ cm (right). MCNPX simulation (Bertini+Dresner) of 1.0 GeV experiment.

I found the largest differences between models in three regions: between $\sim 10^{-4}$ and $\sim 10^{-1}$ MeV, between 5 and 30 MeV, and above 750 MeV (generally near to the beam energy). Even a bit larger differences were observed for bigger beam energies, see Appendix C.

The domain of tens of MeV is of our interest, because the observed threshold reactions have threshold energies there. I focused on this domain (**Fig. 6.4**) and observed two separated regions: in the first region the simulations differ significantly when different evaporation models are used, in the second region when different INC models are used. Rather, the following combinations of INC+evaporation models give the same results (i.e., differences $< 5\%$):

- Bertini+Dresner compared with Isabel+Dresner and Bertini+ABLA compared with Isabel+ABLA both in 1-45 MeV and above 80 MeV (**Fig. 6.4** top left);
- Isabel+Dresner compared with Isabel+ABLA and Bertini+Dresner compared with Bertini+ABLA above 35 MeV and Liège INC+Dresner compared with Liège INC+ABLA above 30 MeV (**Fig. 6.4** top right).

Similar results (the same shape and differences less than 20%) give also:

- Bertini+Dresner compared with CEM03 between 60 and 250 MeV (**Fig. 6.4** top right);
- Bertini+Dresner compared with Liège INC+Dresner and Bertini+ABLA compared with Liège INC+ABLA between 50 MeV and 700 MeV (**Fig. 6.4** bottom left);

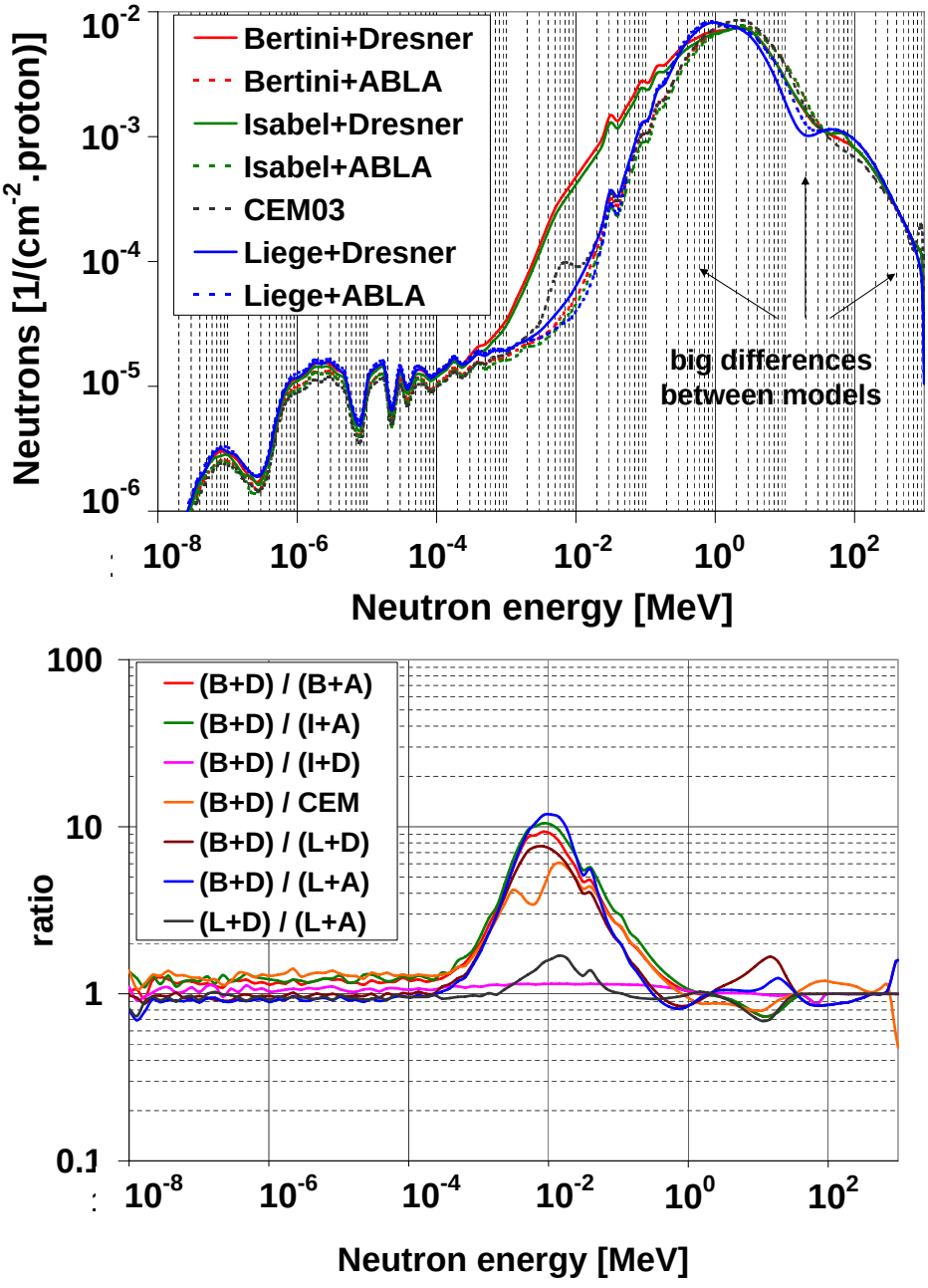


Figure 6.3: Neutron spectra (produced in the first target section) in log-log scale (top) and ratios of these neutron spectra (bottom). MCNPX simulations of the 1.0 GeV proton experiment. All combinations of available physics models in 2.6.C version were used. Equidistant logarithmic energy binning with 100 intervals (for neutron spectra normalized per unit of energy see **Fig. C.1**).

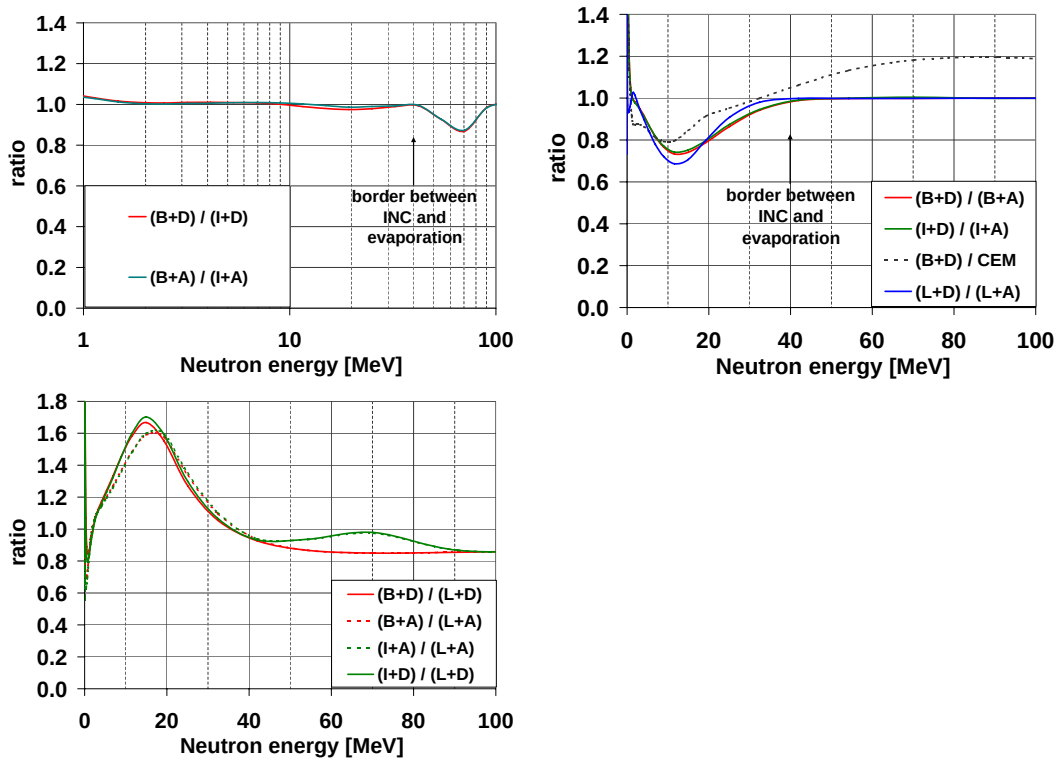


Figure 6.4: Ratios of neutron spectra from **Fig. 6.3**. MCNPX simulations of the 1.0 GeV proton experiment.

- Isabel+Dresner compared with Liège INC+Dresner and Isabel+ABLA compared with Liège INC+ABLA between 90 MeV and 700 MeV (**Fig. 6.4** bottom left).

I interpret this as the evidence of the border between intra-nuclear cascade and evaporation phase of spallation reaction as they are described in the used models. This point appears to be around 40 MeV, which corresponds to the nuclear potential well depth (separation energy plus Fermi-energy), see section 1.2. The border is a bit smaller for Liège INC ($\approx$ 36 MeV) than for Bertini and Isabel INC ($\approx$ 43 MeV), which reflects different approaches to determination of the end of the cascade stage (section 2.2.1).

### 6.1.2 Changes of neutron spectra in dependence on beam energy

Neutron spectra coming from different proton beam energies do not have the same shapes, see **Fig. 6.5**. The contribution of evaporation neutrons (with

energy between 5 MeV and 30 MeV) increases with increasing beam energy. The reason for such behaviour is different energy dependence of number of neutrons emitted during INC and evaporation stages of spallation reaction. The cascade component weakly depend on the proton energy, whereas the evaporation component depends much more on it (see **Fig. 1.8**).

In the case of INC, the most important is the number of collisions made by the incident particle. This parameter does not change strongly with incident energy, because the nucleon-nucleon cross-section does not change much in the considered energy region (see also **Fig. 6.17** right).

In the case of evaporation, the number of emitted neutrons depends mainly on the excitation energy left in the target nucleus at the end of the cascade stage. This excitation energy increases (slightly less than linearly) with the proton beam energy (see **Fig. 1.9**).

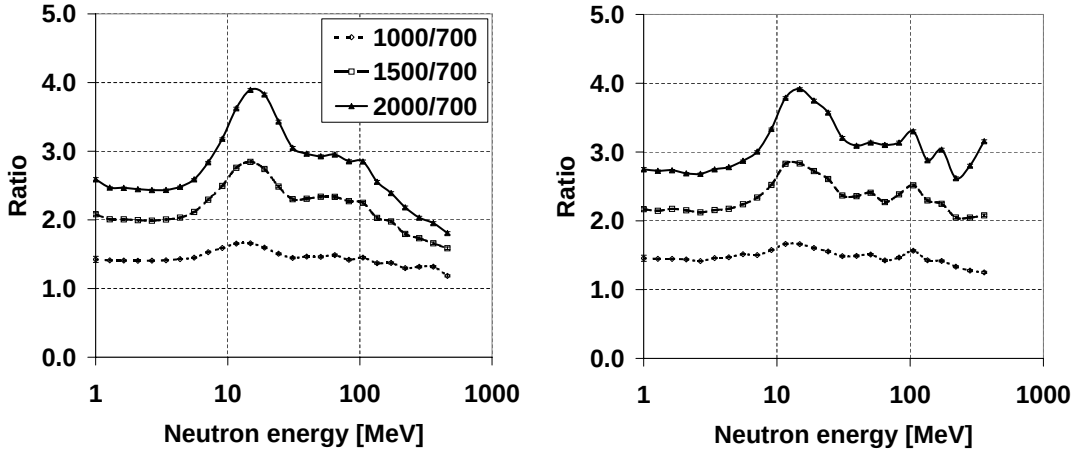


Figure 6.5: Ratios of neutron spectra produced with different proton beam energies. Inside target ($R = 3$ cm) (left) and farther from it ($R = 13$ cm) (right), both at $X = 11.8$ cm. MCNPX simulation (Bertini+Dresner).

## 6.2 Simulations of yields of activation reactions

### 6.2.1 Convolution with (n,$x$n)-cross-sections included in MCNPX

I simulated the yields of nuclei produced in the activation foils directly with MCNPX (using F4 tally with the FM multiplier card) by the convolution of

the simulated neutron spectra $\Phi_{\rm n}(E,r,z)$ (normalized per one beam particle) with the corresponding cross-sections $\sigma_{\rm n}(E)$ (inbuilt in MCNPX from ENDF database [167] for $^{27}$Al(n,$\alpha$)$^{24}$Na, $^{197}$Au(n,$\gamma$)$^{198}$Au, $^{197}$Au(n,2n)$^{196}$Au, and $^{197}$Au(n,4n)$^{194}$Au reactions):

$$N_{\rm yield}(r,z) = \frac{1}{A_r m_u} \int_0^\infty \Phi_{\rm n}(E,r,z)\sigma_{\rm n}(E){\rm dE}, \tag{6.1}$$

where $A_r$ is the specific atomic mass of a chemical element from which the sample is made, $m_u$ is the unified atomic mass unit.

At first, I used the default option Bertini+Dresner, see examples of 1.0 GeV experiment in **Fig. 6.6**. The shapes of longitudinal as well as radial distributions of yields are described very well. A quantitative agreement between experimental and simulated yields is a bit worse, but the absolute differences are less than 40%. The case of $^{198}$Au is a bit special and it is discussed in section 6.3, the rest of this section is concentrated on the yields of threshold reactions.

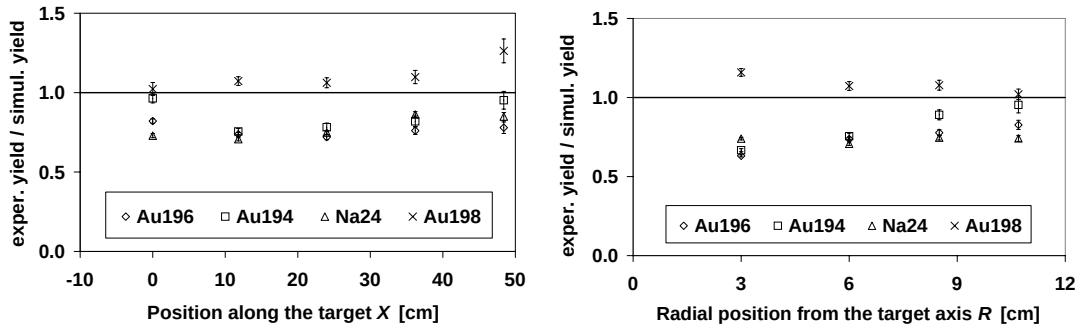


Figure 6.6: Absolute comparison of experimental and simulated (Bertini+Dresner) yields of isotopes produced in Al- and Au-activation samples in longitudinal (left) and radial (right) directions. 1 GeV experiment.

To estimate the influence of different INC+evaporation models on simulated yields of activation reactions, I simulated these yields using all models, see examples of 1.0 GeV experiment in **Fig. 6.7**. Following relations can be seen:

- in the case of $^{196}$Au ($E_{thresh} \approx 8$ MeV) - simulation using Bertini+Dresner gives the same results as Isabel+Dresner (within the error bars); the same holds for Bertini+ABLA compared to Isabel+ABLA;
- in the case of $^{194}$Au ($E_{thresh} \approx 23$ MeV) - simulation using Bertini+Dresner gives the same results as Bertini+ABLA (within the error bars); the same holds for Isabel+Dresner compared to Isabel+ABLA.

Taking into account

- the threshold energies (**Table 3.7**) and
- the fact that cross-sections of these threshold reactions reach their maxima about 10 MeV after $E_{thresh}$ and have important influence even 20 MeV after $E_{thresh}$ (**Fig. 3.17**),

I conclude that evaporation models (Dresner and ABLA) have dominant influence for neutron energies up to $\simeq$ 35 MeV. The INC models (Bertini and Isabel) are dominant for bigger energies. The Liège INC model has influence on the evaporation part of neutron spectra. This observation agree with the conclusion done at the end of section 6.1.1.

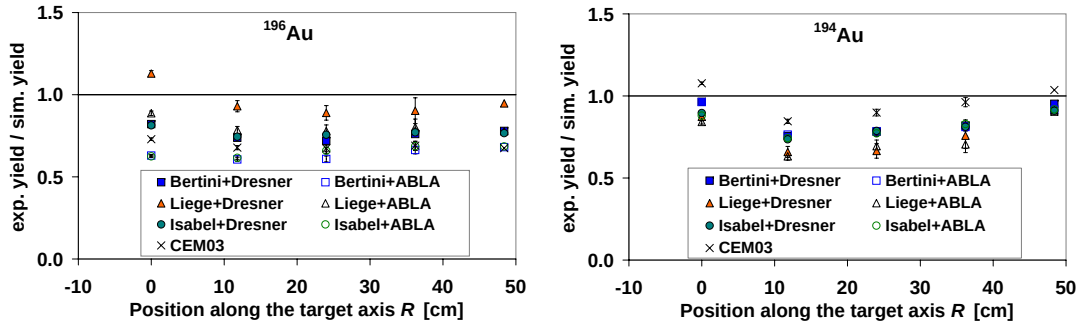


Figure 6.7: Absolute comparison of experimental yields with simulated ones using various combinations of INC+evaporation models. $^{196}$Au (left) and $^{194}$Au (right) distributions. 1 GeV experiment.

From **Fig. 6.7** can be also seen that all of used INC+evaporation models show approximately the same trends. The relative variances between various model combinations are up to 50%. Therefore, I decided to compare relative values (experimental and simulated shapes in longitudinal and radial distributions) rather than absolute values. I normalized the ratios between experimental and simulated yields to the second foil in each set (which is common in both sets – longitudinal and radial). The shapes in *longitudinal* direction agree well for all proton beam energies, see left part of **Fig. 6.8**.

In the contrary, the shapes in *radial* direction differ in dependence on the beam energy. The trends of experimental data and simulations agree well for 0.7 GeV and 1.0 GeV. For 1.5 and 2.0 GeV, these ratios considerably increase with increasing radial distance from the target axis, see right part of **Fig. 6.8**.

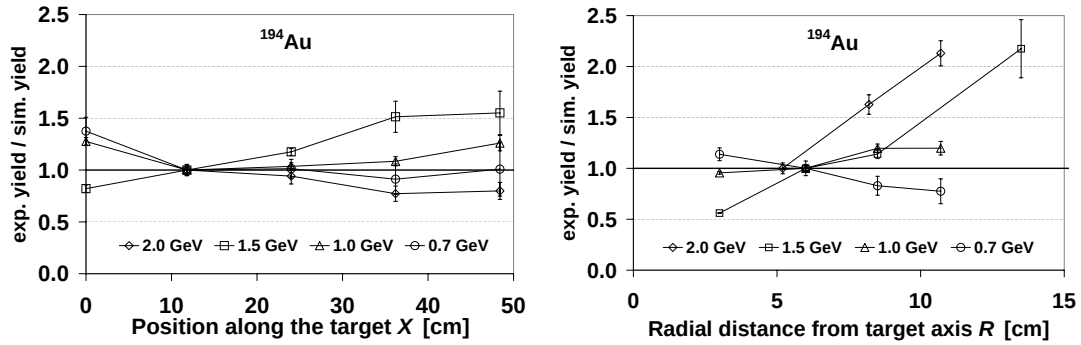


Figure 6.8: Relative comparison of experimental and simulated (Liège+ABLA) yields of $^{194}$Au in longitudinal (left) and radial (right) directions for all proton experiments (normalized to the second foil in each set).

### 6.2.2 Convolution with improved (n,$x$n)-cross-sections and inclusion of proton-induced reactions

I tried to use another cross-sections for convolution with neutron fluxes (eq. (6.1)). But the present status of knowledge of cross-sections for (n,$x$n)-reactions is insufficient. The cross-sections of several observed reactions are known with high enough accuracy at least in the energy region up to 40 MeV (**Fig. 3.17, 3.19**), but the knowledge of most cross-sections is insufficient (**Fig. 3.18**) or they have not been studied at all.

To enable calculations of yields of other observed isotopes and improve existing cross-sections, the TALYS code version 0.79 [144] (up to $E_\mathrm{n} = 150$ MeV) and MCNPX (for $E_\mathrm{n} > 150$ MeV) were used for calculation of corresponding (n,$x$n)-reactions cross-sections, for details see Appendix D.

Moreover, the isotopes observed in activation samples can be produced not only by neutrons, but also by protons[1]. Therefore, the cross-sections $\sigma_\mathrm{p}(E)$ of possible proton-induced reactions leading to the same nuclei as neutron-induced ones (e.g., $^{197}$Au(p,pn)$^{196}$Au, $^{197}$Au(p,p3n)$^{194}$Au) were determined as well, see also Appendix D.

I used these new cross-sections for "manual" convolution with MCNPX simulated neutron $\Phi_\mathrm{n}(E,r,z)$ and proton $\Phi_\mathrm{p}(E,r,z)$ spectra (in the positions of activation samples) to obtain the simulated yields:

$$N_\mathrm{yield}(r,z) = \frac{1}{A_r m_u} \int_0^\infty [\Phi_\mathrm{n}(E,r,z)\sigma_\mathrm{n}(E) + \Phi_\mathrm{p}(E,r,z)\sigma_\mathrm{p}(E)]\mathrm{d}E. \quad (6.2)$$

[1]Protons can contribute up to 20% [84, 97] to the observed yields. The influence of other particles (as pions or photons) is negligible in our case [97].

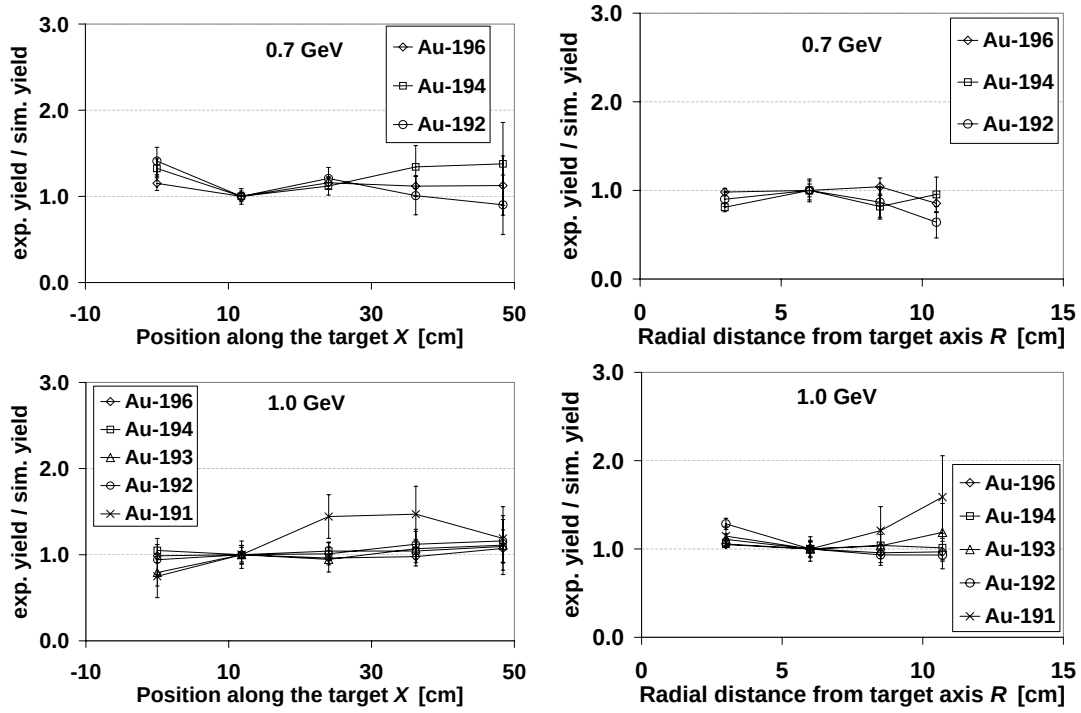


Figure 6.9: Relative comparison of experimental and simulated (spectra simulated with Liège INC+ABLA and convoluted with TALYS+MCNPX cross-sections) Au-yields in longitudinal (left) and radial (right) directions for the 0.7 GeV (top) and 1.0 GeV (bottom) proton experiments (normalized to the second foil in each set).

Comparison with experimental yields (**Fig. 6.9, 6.10**) pointed to that the usage of improved (n,$x$n)-cross-sections and inclusion of proton-induced reactions did not cancel the discrepancy in radial direction (**Fig. 6.11**). Naturally, it caused an increase in simulated yields, which is more distinctive in the positions closer to the beam axis, where the share of protons is largest.

I assume that the reason is in the evaluated cross-section libraries or INC+evaporation models. It looks like they do not describe correctly the angular distribution of the produced high-energy neutrons for proton beam energies bigger than some value between 1.0 and 1.5 GeV. Similar observations have been done on both thick and thin targets [140], when it was found that simulations underestimate the neutron production for backward angles, see also section 2.4. It will be also interesting if final results of the 1.26 $A$GeV deuteron experiment show discrepancy in the radial direction.

Source of problems could be for example the U-blanket as the LA150 data library (neither the NRG-2003 library, see section 2.2.4) does not include cross-sections for uranium and all interactions in the blanket are being

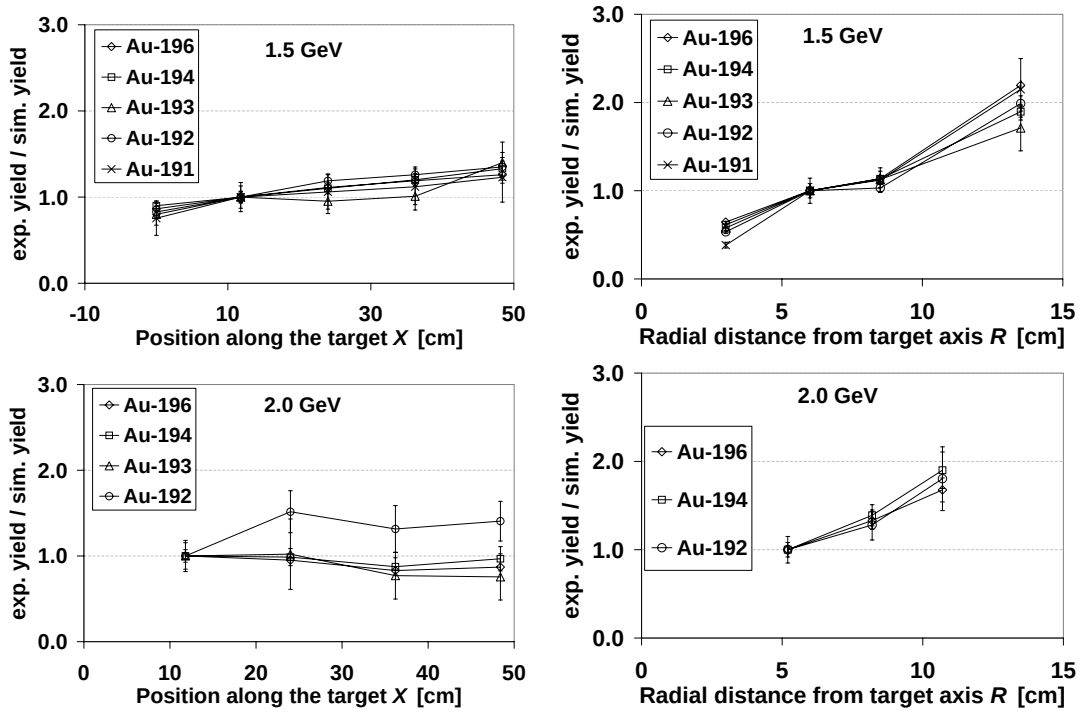


Figure 6.10: Relative comparison of experimental and simulated (spectra simulated with Liège INC+ABLA and convoluted with TALYS+MCNPX cross-sections) Au-yields in longitudinal (left) and radial (right) directions for the 1.5 GeV (top) and 2.0 GeV (bottom) proton experiments (normalized to the second foil in each set in the case of 1.5 GeV, to the first foil in the case of 2.0 GeV).

simulated by INC+evaporation models. This assumption could be tested if we carry out an experiment with 1.5 GeV or 2.0 GeV proton beam on the E+T setup without the U-blanket.

## 6.3 Neutron multiplicity

I studied the influence of the polyethylene shielding on the produced neutron field (**Fig. 3.7**) to find out which parts of spectra are significantly changed and which are not influenced. The neutron spectrum is not influenced for $E_n > 0.5$ MeV, but it is strongly influenced for lower energies. This low energy neutron field, which was created by moderation in polyethylene, is near to homogeneous. The Cd-layer on the inner walls of the shielding absorbed the peak of thermal neutrons (below the cadmium threshold $E_n < 0.5$ eV).

The most of the low energy neutron field (0.5 eV $< E_n <$ 0.5 MeV) comes from the shielding-moderator and its intensity is determined by the

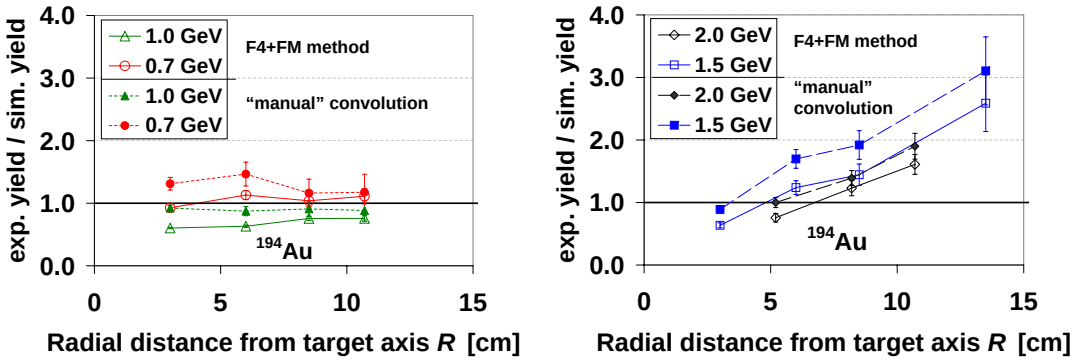


Figure 6.11: Absolute comparison of experimental and simulated (Liège INC+ABLA) yields of $^{194}$Au in radial direction. Open symbols represent values when the simulated yields were calculated directly with MCNPX (using F4 tally with the FM multiplier card), full symbols represent values when "manual" convolution (with TALYS+MCNPX cross-sections of (n,$x$n)- and (p,p($x-1$)n)-reactions) were used.

total number of neutrons leaving the blanket. The resonance and epithermal neutrons (0.5 eV $< E_{\mathrm{n}} <$ 1 keV) are dominant for the neutron capture reactions in activation samples, i.e., $^{197}$Au(n,$\gamma$)$^{198}$Au (see bottom right corner of **Fig. 6.12**). Thus, the production of $^{198}$Au depends on the total number of neutrons escaping the blanket.

### 6.3.1 Determination of neutron multiplicity

The often used method for the determination of the integral number of neutron produced on thick target is the so-called water-bath/activation-foil method [152]. The conventional variant of this method uses two basic premises: neutrons from the source are predominantly contained within the moderator volume; it is possible to integrate the measured thermal flux distribution over the water volume with adequate precision. As the latter requires the usage of a large-scale grid of activation foils, I used the new form of this method [138], which replaces the flux integration by relating a small-scale set of foil activities to the integral quantity – the integral number of neutrons produced per one beam particle (so-called neutron multiplicity) $M_{\mathrm{n}}^{\mathrm{sim}}$ obtained by simulation.

I took into account our experiments with polyethylene moderator: the E+T proton (**Table 1.4**, Appendix B) and deuteron (**Table 1.5** - preliminary results by Svoboda [153, 154]) experiments, and the 885 MeV proton experiment (**Table 1.3** – author's analysis [84]) with a Pb-target surrounded

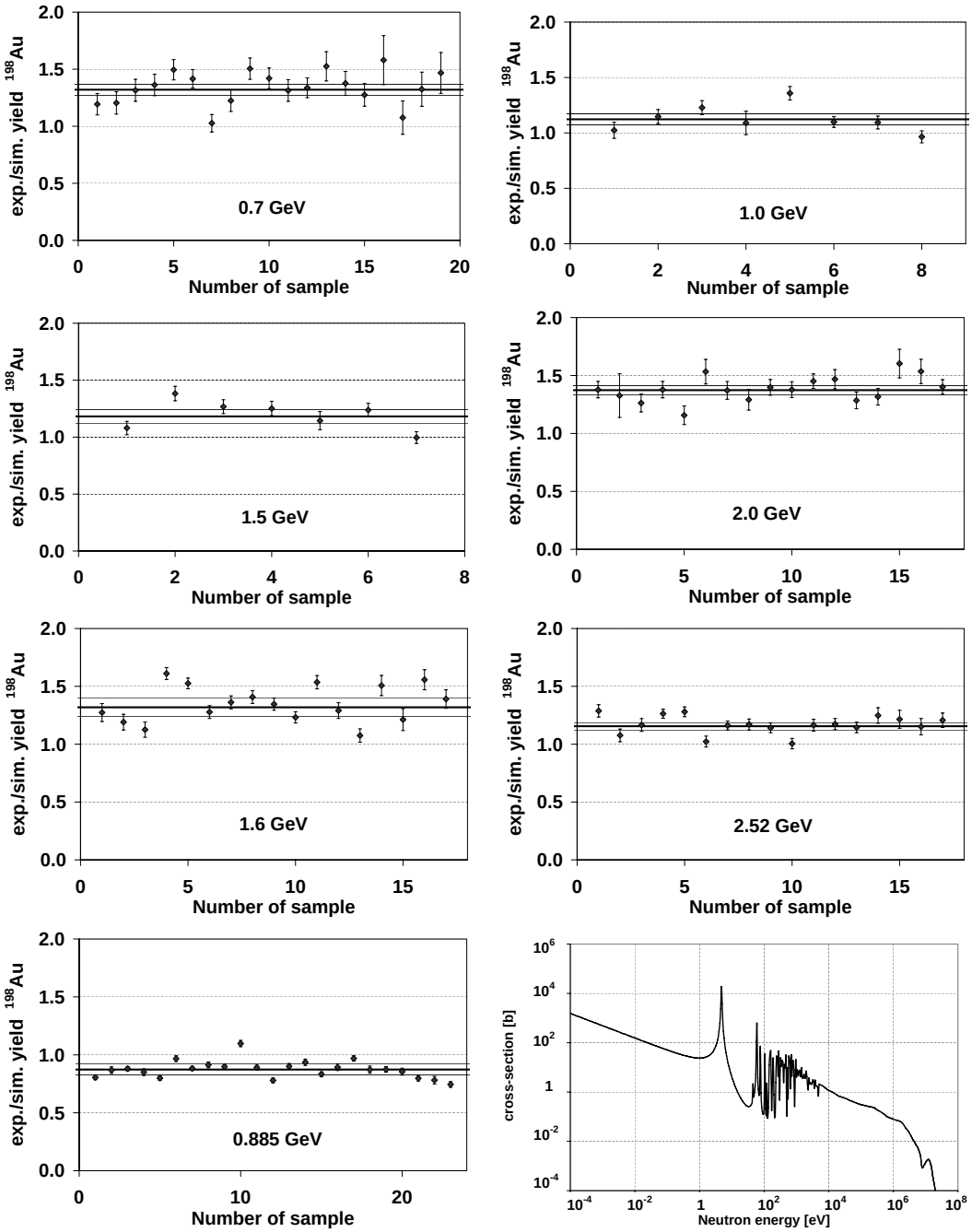


Figure 6.12: Ratios between experimental and simulated (Liège+ABLA) $^{198}$Au yields for our experiments with polyethylene moderator. Thick solid lines represent the weighted averages of these ratios, thin solid lines represent their lower and upper limits. The last figure is cross-section of $^{197}$Au(n,$\gamma$)$^{198}$Au [163].

by a polyethylene moderator (the same as in the E+T setup). Polyethylene worked as a water bath – it moderated the outgoing neutrons.

I determined the ratios between experimental yields $N_{\mathrm{yield}}^{\mathrm{exp}}$ and simulated yields $N_{\mathrm{yield}}^{\mathrm{sim}}$ of $^{198}$Au for all used Au-samples, see **Fig. 6.12** and **Table 6.1**. The experimental neutron multiplicity can be obtained by multiplying the mean value of these ratios (over all Au-samples in each experiment) and the simulated neutron multiplicity:

$$M_{\mathrm{n}}^{\mathrm{exp}} = M_{\mathrm{n}}^{\mathrm{sim}} \langle \frac{N_{\mathrm{yield}}^{\mathrm{exp}}}{N_{\mathrm{yield}}^{\mathrm{sim}}} \rangle. \tag{6.3}$$

The advantage of this procedure is that the experimental value of neutron multiplicity $M_{\mathrm{n}}^{\mathrm{exp}}$ is highly insensitive to the simulated value $M_{\mathrm{n}}^{\mathrm{sim}}$ and its error. On the assumption that MCNPX models well the shape of low energy part of neutron spectrum and its approximate magnitude, the product of the two terms on the right-hand side of eq. (6.3) effectively cancels out the dependence on $M_{\mathrm{n}}^{\mathrm{sim}}$.

Now, let me to comment the validity of this assumption. I simulated both terms from the right-hand side of eq. (6.3) using all combinations of INC+evaporation models in MCNPX 2.6.C and, thus, determined the left-hand side of eq. (6.3). Neutron multiplicity $M_{\mathrm{n}}^{\mathrm{sim}}$ does not depend significantly on the combination of the INC+evaporation models in the considered region (0.7–2 GeV), differences are less than 10%, only Liège INC+Dresner gives smaller values for bigger energies (13% less than Bertini+Dresner for 2 GeV), see **Fig. 6.13**.

But $\langle \frac{N_{\mathrm{yield}}^{\mathrm{exp}}}{N_{\mathrm{yield}}^{\mathrm{sim}}} \rangle$ changes with different INC+evaporation models and influences $M_{\mathrm{n}}^{\mathrm{exp}}$, see example of 1 GeV experiment in **Fig. 6.14**. Bertini+Dresner, Isabel+Dresner, Liège+Dresner, and Liège+ABLA give the same values of $M_{\mathrm{n}}^{\mathrm{exp}}$ (within the error bars) thanks to the fact that the differences in $M_{\mathrm{n}}^{\mathrm{sim}}$ and $\langle \frac{N_{\mathrm{yield}}^{\mathrm{exp}}}{N_{\mathrm{yield}}^{\mathrm{sim}}} \rangle$ (which are very small anyway) really cancel out. This is not valid for CEM03, Bertini+ABLA, and Isabel+ABLA, which show bigger differences of $M_{\mathrm{n}}^{\mathrm{exp}}$ (38%, 17%, 18%, respectively). Despite of such dissension, I do consider this method to be applicable to our case because the ABLA model has been generally coupled with the Liège INC model and its combinations with other INC models need not to be reliable for lower energies. Hereafter, I take into account the results of the first four model combinations.

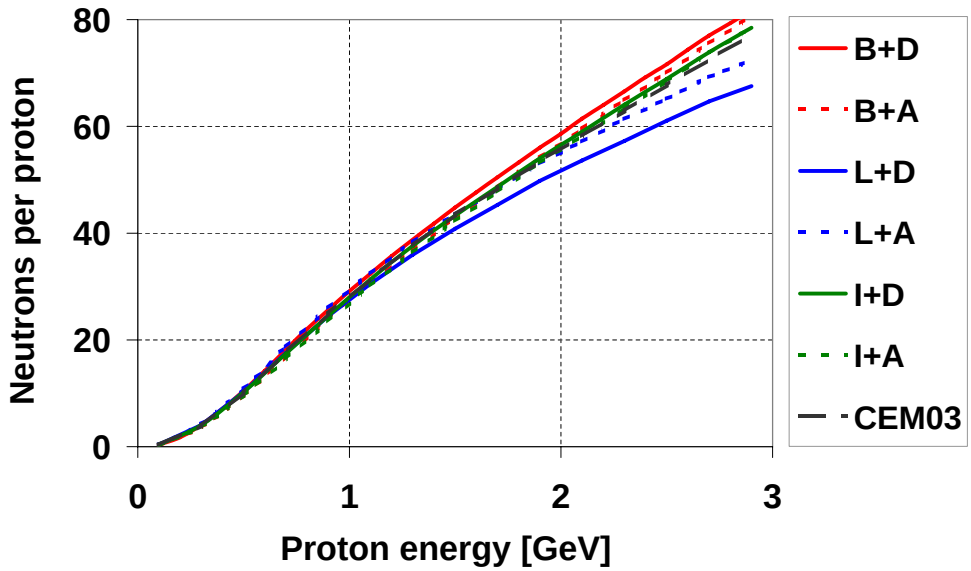


Figure 6.13: Dependence of neutron multiplicity on proton beam energy for the E+T setup. Comparison of all INC+evaporation models combinations available in MCNPX 2.6.C version.

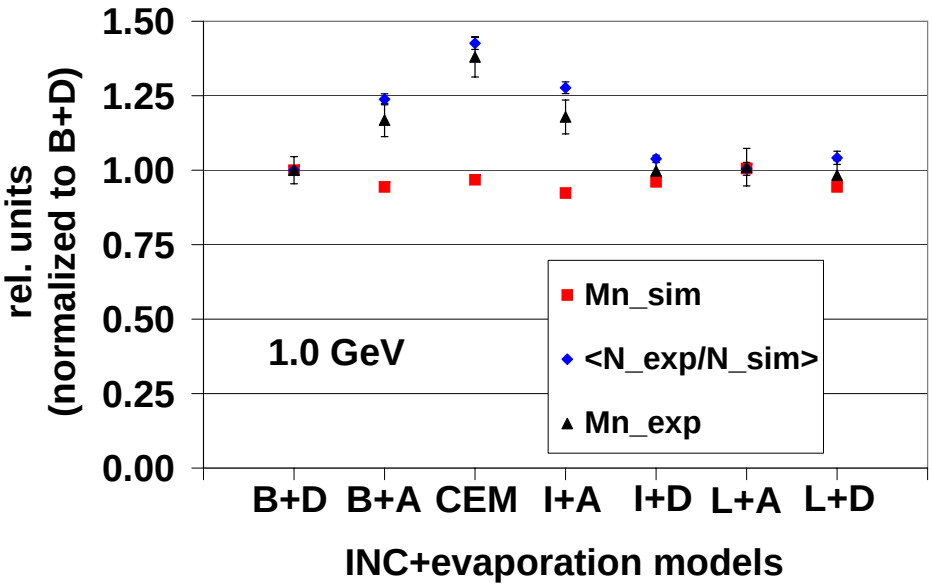


Figure 6.14: Comparison of INC+evaporation models combinations in description of the simulated neutron multiplicity $M_{\mathrm{n}}^{\mathrm{sim}}$, the mean value of the ratios between experimental $N_{\mathrm{yield}}^{\mathrm{exp}}$ and simulated yields $N_{\mathrm{yield}}^{\mathrm{sim}}$ of $^{198}$Au, and the influence on the experimental multiplicity $M_{\mathrm{n}}^{\mathrm{exp}}$, see eq. (6.3). Example of the 1 GeV experiment.

### 6.3.2 Neutron multiplicity on a simple lead target

The energy dependence of neutron multiplicity was studied by a number of experiments for lead targets of different sizes (see the overview [138]). Because $M_{\mathrm{n}}$ depends on the target size, the data need to be normalized.

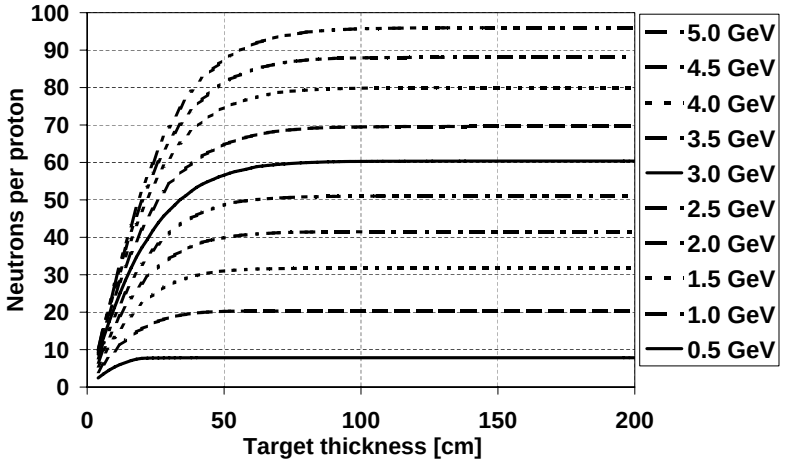


Figure 6.15: Dependence of neutron multiplicity on target thickness and beam energy for a Pb-target with radius of 5 cm (usual radius). MCNPX simulation (Bertini+Dresner). Such dependence was investigated experimentally by Letourneau et al. [39], see **Fig. 1.13**.

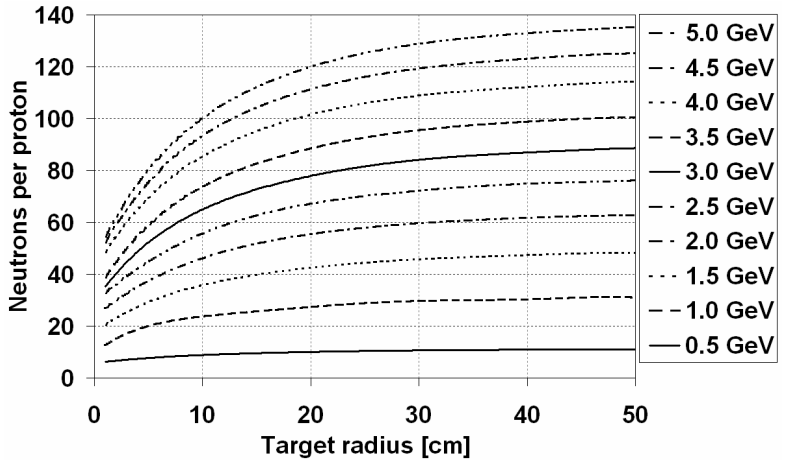


Figure 6.16: Dependence of neutron multiplicity on target radius and beam energy for a Pb-target with thickness of 100 cm (saturated thickness). MCNPX simulation (Bertini+Dresner).

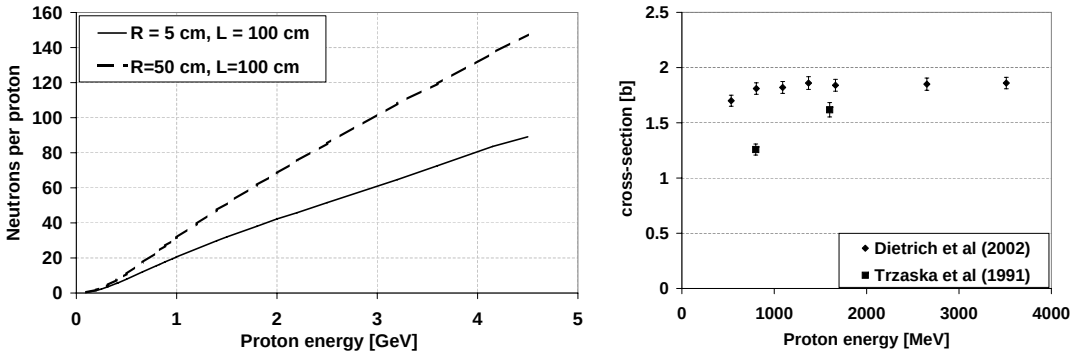


Figure 6.17: Dependence of neutron multiplicity produced on a Pb-target with radius of 5 cm (usual radius) and 50 cm (saturated radius), both for target thickness of 100 cm (saturated thickness), on proton beam energy. MCNPX simulation (Bertini+Dresner) (left). Total cross-section of p+Pb reaction measured by Dietrich et al. [174] and Trzaska et al. [175] (right).

With help of MCNPX simulation I have found the "saturated thickness" ($L \approx 100$ cm, see **Fig. 6.15**) and "saturated radius" ($R \approx 50$ cm, see **Fig. 6.16**), for which I have got complete saturation of neutron production – it is possible to reach the maximal number of the produced neutrons for the given beam energy, see **Fig. 6.17** left. In all simulations presented in this section, I used a homogeneous beam with radius of 1.5 cm.

The saturated thickness is smaller than one could expect considering the electronic-stopping range done by ionization (**Fig. 1.12**), which is bigger than 100 cm even for $E_\mathrm{p} > 1.7$ GeV on Pb-target. Saturation is for lower beam energies done by ionization, for bigger energies by loss of protons by nuclear reactions.

The reason consists in practical extinction of primary proton beam (with the incident energy in a GeV range) before 100 cm of target thickness, because almost all beam particles interact by spallation reactions during this distance. Taking into account that the total reaction cross-section for p+Pb is approximately constant in a GeV-range ($\sigma_\mathrm{tot} \approx 1.8$ b, see **Fig. 6.17** right), only 0.3% of the primary proton beam remains after passing 100 cm of lead.

The most of the experiments have been carried out with a target radius around 5 cm. For this reason all data from different experiments have been re-counted to the case with the radius of 5 cm and the saturated thickness of 100 cm (by comparing the simulated multiplicities for this "normalized" target size with a real target size). The applied corrections were mostly a few percent; the exception are only data by Vasilkov et al. [176] with a very large target. The obtained compilation was fitted by a simple polynomial

function, see **Fig. 6.18**. Our experimental point of the 885 MeV proton experiment with a simple Pb-target and polyethylene moderator is in very good agreement with other experimental points.

The MCNPX simulation describes the integral neutron production very well for proton energies less than app. 0.8 GeV (the ratio simulation to experiment is 1.01 for 0.5 GeV; 1.10 for 0.8 GeV), but overestimates it for bigger energies (the ratio simulation to experiment is 1.13 for 1 GeV, 1.15 for 2 GeV; 1.18 for 3 GeV, 1.29 for 4.5 GeV).

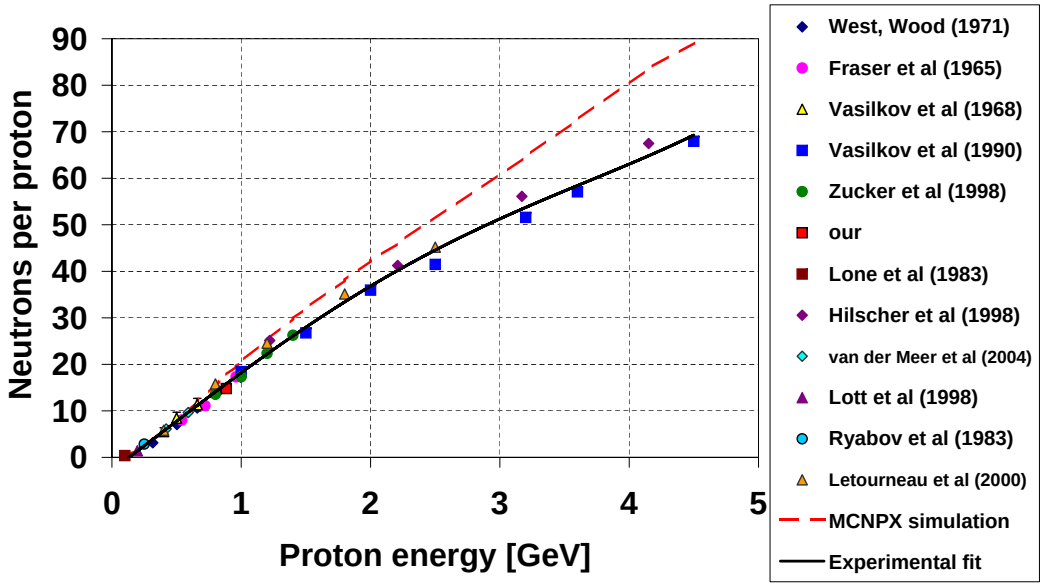


Figure 6.18: The compilation of neutron multiplicities for p+Pb have been measured to date. Experimental data (West, Wood [177], Fraser et al. [178], Vasilkov et al. [176, 42], Zucker et al. [179], our experimental point [84], Lone et al. [180], Hilscher et al. [35], van der Meer et al. [138], Lott et al. [40], Ryabov et al. [181], Letourneau et al. [39]) were re-counted to target thickness of 100 cm and radius of 5 cm and fitted by a simple polynomial function (solid black curve). The red dashed curve represents MCNPX simulation (Bertini+Dresner).

### 6.3.3 Neutron multiplicity on the E+T setup

The E+T setup consists not only of natural lead (target), but also of natural uranium (blanket). As the incident beam has Gaussian distribution (see section 3.3.2), the separation into target and blanket is not strict and it is possible to talk about a target made of lead and uranium.

The situation for uranium is different than for lead, because $^{238}$U has huge neutron capture cross-section, see **Fig. 6.19**. First, let me to consider

a simple U-target. The U-target size for which the neutron *production* reaches saturation (and for bigger size stays the same) exists too (**Fig. 6.20** left). But important is other size – such, for which the number of *escaped* neutrons (i.e., available for other, for example transmutation, purposes) reaches its maximum (**Fig. 6.20** right) and for bigger target size decreases because of neutron *capture* (for details see Appendix E). The "classical" saturation occurs for radius smaller than 20 cm, where the number of produced neutrons increases more steeply with target thickness than the number of absorbed neutrons. The maximal number of escaped neutrons happen for $R \approx 20$ cm, $L \approx 100$ cm. For bigger target radii the number of escaped neutrons drops as the number of captured neutrons increase.

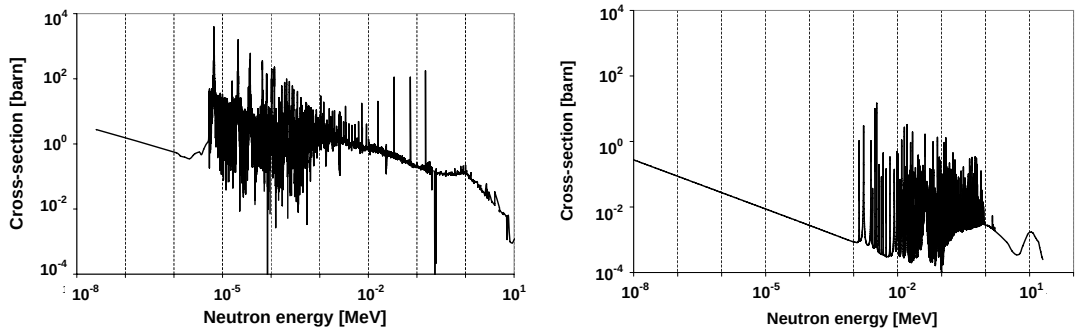


Figure 6.19: Neutron capture cross-section on $^{238}$U [163] (left) and $^{\text{nat}}$Pb [167] (right).

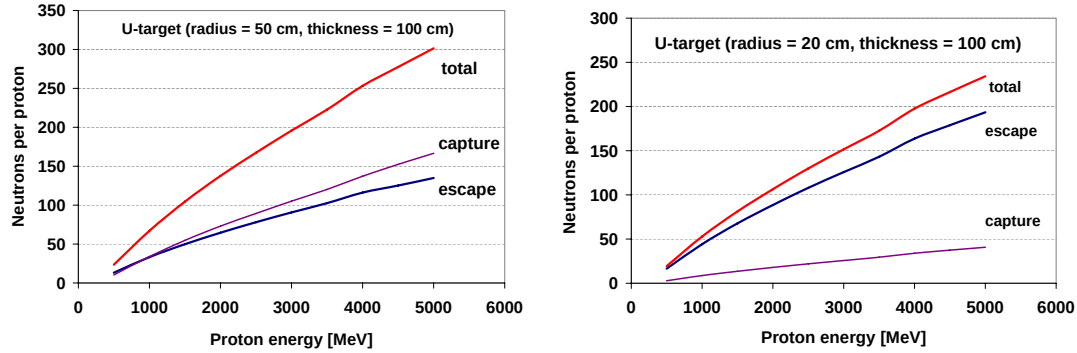


Figure 6.20: Dependence of neutron multiplicity on beam energy for a U-target. Two important cases are plotted: saturated target size for maximal neutron production – radius of 50 cm, thickness of 100 cm (left); optimal target size for maximum number of escaped neutrons – radius of 20 cm, thickness of 100 cm (right). MCNPX simulation (Bertini+Dresner).

I compared the values of $M_n^{exp}$ obtained using eq. (6.3) for the E+T experiments with a simple Pb-target data and MCNPX simulations, see **Fig. 6.21** and **Table 6.1**. I did these simulations using Liège INC+ABLA, because the Liège INC model is the only one among physics models available in MCNPX 2.6.C that gives reasonable results for experiments with deuteron beams with energy bigger than 2 GeV [94]. The E+T experimental results are bigger (app. between 10% and 40%) than the simulated neutron production, they are between predictions for saturated Pb-target and optimal U-target.

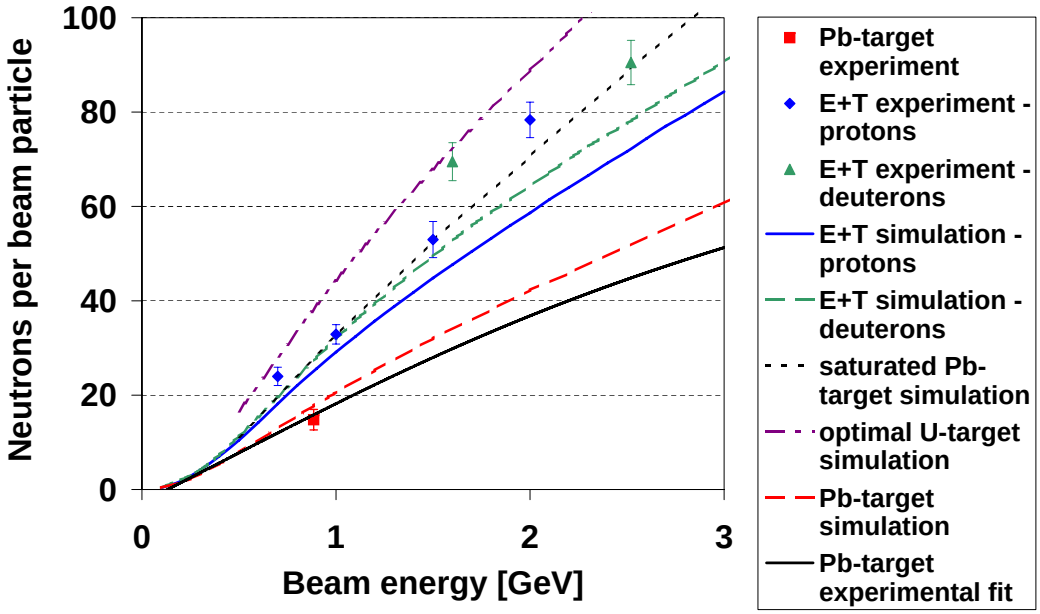


Figure 6.21: The compilation of neutron multiplicities for our experiments with polyethylene moderator compared with MCNPX simulations (Liège+ABLA).

Noteworthy is that the dependence of the integral neutron production on beam energy starts to be constant around 1 GeV when normalized per unit of beam energy (so-called neutron cost), see **Fig. 6.22**. Hence, the optimal beam energy for neutron production appears to be around this value (which agree with results of others, e.g. [36], see section 1.2.3).

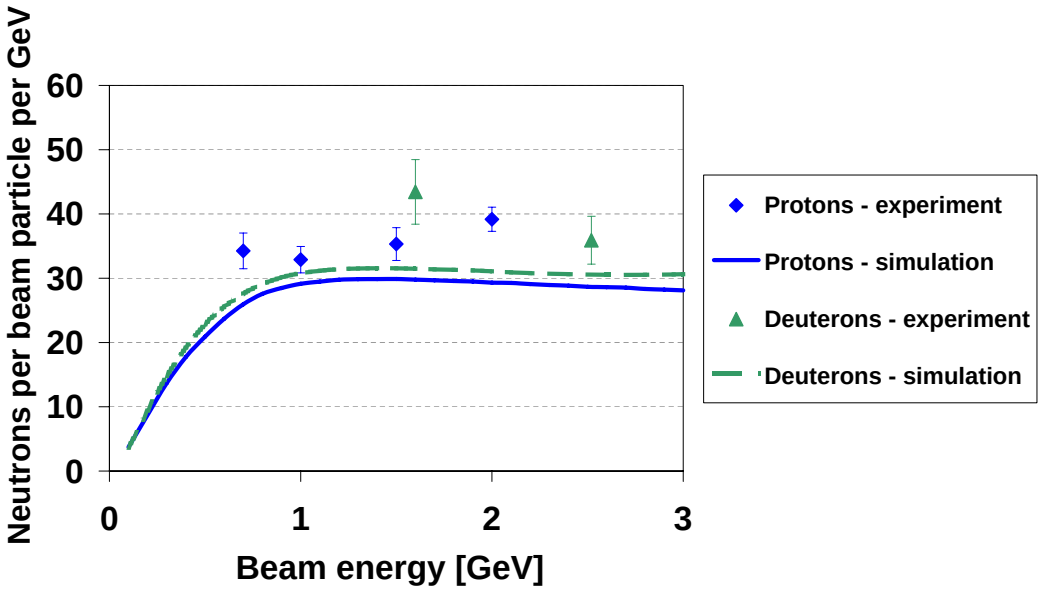


Figure 6.22: Dependence of neutron cost on beam energy. Experimental data of the E+T proton and deuteron experiments compared with MCNPX simulations (Liège+ABLA).

Table 6.1: Mean values of ratios between experimental and simulated yields (Liège+ABLA) of $^{198}$Au, neutron multiplicities, and neutron costs in our experiments with polyethylene moderator (which worked as a water bath). The errors of $\langle \frac{N^{\mathrm{exp}}_{\mathrm{yield}}}{N^{\mathrm{sim}}_{\mathrm{yield}}} \rangle$ are errors of the mean value including $\chi^2$. The errors of neutron multiplicities and costs include also errors of the beam integral determination.

| Setup | Beam particle | Beam energy [GeV] | $\langle \frac{N^{\mathrm{exp}}_{\mathrm{yield}}}{N^{\mathrm{sim}}_{\mathrm{yield}}} \rangle$ | $M^{\mathrm{exp}}_{\mathrm{n}}$ | $M^{\mathrm{sim}}_{\mathrm{n}}$ | $M^{\mathrm{exp}}_{\mathrm{n}}$ per GeV | $M^{\mathrm{sim}}_{\mathrm{n}}$ per GeV |
|---|---|---|---|---|---|---|---|
| Pb-target | p | 0.885 | $0.87 \pm 0.05$ | $14.8 \pm 2.2$ | 17.0 | $16.7 \pm 2.5$ | 19.2 |
| E+T | p | 0.7 | $1.32 \pm 0.04$ | $24.0 \pm 1.9$ | 18.2 | $34.3 \pm 2.8$ | 26.0 |
| | | 1.0 | $1.12 \pm 0.04$ | $32.9 \pm 2.1$ | 29.3 | $32.9 \pm 2.1$ | 29.3 |
| | | 1.5 | $1.18 \pm 0.05$ | $53.0 \pm 3.8$ | 44.8 | $35.3 \pm 2.6$ | 29.9 |
| | | 2.0 | $1.37 \pm 0.03$ | $78.4 \pm 5.3$ | 58.6 | $39.2 \pm 1.9$ | 29.3 |
| | d | 1.6 | $1.32 \pm 0.06$ | $70 \pm 8$ | 53 | $43 \pm 5$ | 33 |
| | | 2.52 | $1.16 \pm 0.03$ | $91 \pm 9$ | 78 | $36 \pm 4$ | 31 |

# Chapter 7

# Conclusion

In the framework of the "Energy plus Transmutation" project, I have studied neutron production in the spallation reactions of protons with the kinetic energies of 0.7, 1.0, 1.5, and 2.0 GeV that hit the thick, lead target with the uranium blanket surrounded by the polyethylene moderator. The produced neutron field was measured by means of activation detectors.

Due to the hard part of the neutron spectrum in the Pb/U-assembly, I observed isotopes produced in (n,$x$n)-reactions (the emission of up to $x = 9$ neutrons) with threshold energy up to $E_{\mathrm{thresh}} \approx 60$ MeV. The maximum intensity of the high-energy neutron field (the region of tens of MeV ) produced in the spallation target is located in the region between the first and second target/blanket sections. The neutron energy spectrum becomes harder at the end of the target. The contribution of evaporation neutrons in the spallation spectrum increases with increasing proton beam energy.

Low-energy neutrons (epithermal and resonance region) were produced mainly by moderation (and back-scattering) in the polyethylene shielding. I used this homogenous low-energy neutron field to determine the integral number of produced neutrons per one beam particle.

I compared the experimental results with Monte-Carlo simulations performed using the MCNPX code, version 2.6.C. The overall experimental data of the integral neutron production on simple lead target (extracted from literature) are described very well for proton beam energies less than 0.8 GeV, but overestimated for bigger energies ($10 - 30\%$ difference up to 4.5 GeV). The experimental integral neutron production on the E+T setup is bigger than the simulated one (but for less than 40%) for all used proton beam energies as well as for 1.6 and 2.52 GeV deuteron beams.

Simulations of the produced neutron spectra in the E+T setup significantly differ when different combinations of intra-nuclear cascade models with evaporation models are used. The biggest differences are in the regions

of $10^{-4} - 10^{-1}$ MeV, $5 - 30$ MeV, and near to the beam energy. The border between different neutron production mechanisms, as they are described in the used models, was found out to be around 40 MeV (a bit lower for the Liège INC model, a bit higher for the Bertini and Isabel INC models). Neutrons are produced in the evaporation stage below this point, in the cascade stage above it.

MCNPX describes well the shape of the longitudinal distributions of the yields of threshold reactions. This was observed for the E+T experiments with all used proton beam energies and all combinations of intra-nuclear cascade models with evaporation models included in the 2.6.C version. A quantitative agreement between experimental and simulated yields is a bit worse, the absolute differences reach typically tens of per cent, but do not exceed 40%.

The shapes of the radial distributions of experimental yields of threshold reactions differ from the simulated ones in dependence on the proton beam energy. While for 0.7 and 1.0 GeV the simulations and experiments are in a reasonable agreement, for 1.5 and 2.0 GeV the simulations predict much steeper decrease of the yields with growing radial distance than it was measured. This discrepancy between experimental and simulated data is as large as a factor of two and cannot be explained with the uncertainties of the experimental data.

Incompleteness of (n,$x$n)-cross-section libraries used for calculation of the yields is probably not the reason as the usage of improved cross-sections (calculated with TALYS and MCNPX) did not help to reach an agreement between experiment and simulation. I conclude that the reason of the observed discrepancy in radial distributions of yields of threshold reactions should be in the LA150 evaluated cross-section libraries or intra-nuclear cascade+evaporation models included in MCNPX. For proton beam energies bigger than some value between 1.0 and 1.5 GeV (it will be interesting if final results of the 1.26 $A$GeV deuteron experiment show discrepancy in the radial direction), they do not describe correctly the angular distribution of produced neutrons, namely they underestimate the neutron production at backward angles.

Whereas LA150 does not include cross-sections for uranium, all interactions in the blanket are simulated by intra-nuclear cascade+evaporation models. Therefore, new experiment with 1.5 GeV or 2.0 GeV proton beam on the E+T setup without the U-blanket could validate or foreclose modelling of interactions in the U-blanket as the source of the observed discrepancy.

# Appendix A
# Example of MCNPX input file

This is an example of the MCNPX input file that was used in simulations presented in this thesis. Italic font is used for comments.

c CELL CARD
*Pb-target*
*(cell number, material number, density, surfaces numbers – the intersection operator is a blank space between two signed surface numbers)*
1 1 -11.340 -1 50 -51
*Fe out of the beam tube*
2 8 -7.874 2 -3 -4
*U-rods place*
50 0 358 70 -71 105 -100 103 -101 102 -104 fill=1
*lattice with U-rods*
51 0 203 -202 205 -204 -201 200 lat=2 u=1 trcl=(0 0 0.5)
fill=-4:4 -4:4 0:0
3 3 3 3 3 3 3 3 3
3 3 3 3 2 2 2 2 3
3 3 3 2 2 2 2 2 3
3 3 2 2 3 3 2 2 3
3 2 2 3 3 3 2 2 3
3 2 2 3 3 2 2 3 3
3 2 2 2 2 2 3 3 3
3 2 2 2 2 3 3 3 3
3 3 3 3 3 3 3 3 3
*U-rod*
100 2 -19.050 -250 252 -253 u=2
*Al-envelope of U-rods*
*(The union operator is signified by a colon ":")*
101 3 -2.7 (250 -251 252 -253):(-251 50 -252):(-251 253 -254) u=2

*air*
102 4 -0.00129 251 u=2
103 4 -0.00129 -500 u=3
*vertical Fe-plate that enclose a blanket section*
110 8 -7.874 (350 -351 352 -353 358 70 -354 -401 402 403 -404
(-105:100:-103:101:-102:104)):
(350 -351 352 -353 355 358 -71 -401 402 403 -404
(-105:100:-103:101:-102:104))
*vertical Al-plate in front and behind hexagon*
120 3 -2.7 (358 -70 50 405 -400 403 -401 402 -404):
(358 -51 71 405 -400 403 -401 402 -404)
*Al-shielding for Pb-target*
130 3 -2.7 1 -358 50 -51
*Fe-shielding around U-rods*
140 8 -7.874 (-100 72 101 -451 354 -355):(-72 105 -102 452 354 -355):
(-105 455 452 453 354 -355):(-72 105 -103 453 354 -355):
(-100 72 104 -454 354 -355)
*upper Al-shielding around U-rods*
141 8 -7.874 100 -450 -451 -454 354 -355
*air inside target*
*(The complement operator, signified by the # symbol, stands for "not in". The notation* #n*, where* n *is a cell number, means that the description of the current cell is the complement of the description of cell* n*. That is, a number immediately after # is interpreted as a cell number and is shorthand for the geometry specification of that cell number.)*
145 4 -0.00129 (100:-103:101:-102:104:-105) 405 -400 403 -401 402 -404
70 -71 (#110) (#140) (#141) (#152) (#155) (#202) (#205)
(#252) (#255) (#256)
*next three sections of the target transformed*
150 like 1 but trcl=(0 0 12.2)
151 like 50 but trcl=(0 0 12.2)
152 like 110 but trcl=(0 0 12.2)
153 like 120 but trcl=(0 0 12.2)
154 like 130 but trcl=(0 0 12.2)
155 like 140 but trcl=(0 0 12.2)
156 like 145 but trcl=(0 0 12.2)
200 like 1 but trcl=(0 0 24.4)
201 like 50 but trcl=(0 0 24.4)
202 like 110 but trcl=(0 0 24.4)
203 like 120 but trcl=(0 0 24.4)
204 like 130 but trcl=(0 0 24.4)

```
205 like 140 but trcl=(0 0 24.4)
206 like 145 but trcl=(0 0 24.4)
250 like 1 but trcl=(0 0 36.6)
251 like 50 but trcl=(0 0 36.6)
252 like 110 but trcl=(0 0 36.6)
253 like 120 but trcl=(0 0 36.6)
254 like 130 but trcl=(0 0 36.6)
255 like 140 but trcl=(0 0 36.6)
256 like 141 but trcl=(0 0 36.6)
257 like 145 but trcl=(0 0 36.6)
Cd-layer
350 6 -8.65 (304:-302:-308:310) (303 -305 309 -311 300 -301)
polyethylene box
360 5 -0.802 (300 -301 303 -305 311 -313):(300 -301 303 -305 312 -309):
                (300 -301 305 -307 317 -318):(300 -301 306 -303 312 -313):
                (300 -301 314 -315 -306 316)
Fe-plate
361 8 -7.874 58 -59 320 -321 -405 322
wooden plates under the blanket
362 9 -0.5 58 -59 320 -321 -322 323
textolite plate
363 9 -0.5 300 -301 308 -310 302 -323
air everywhere inside
370 4 -0.00129 300 -301 302 -304 308 -310 (400:401:-402:-403:404:-405:
                  -58:59) (#361) (#362) (#363) (#520)
air outside the blanket
380 4 -0.00129 (-306:307:-300:301:-312:313) (#2) (#360) -500
end of target/blanket, beginning of activation samples definition
500 10 -19.3 79 -81 82 -83 92 -93
501 10 -19.3 79 -81 84 -85 92 -93
510 10 -19.3 86 -87 82 -83 92 -93
511 10 -19.3 86 -87 84 -85 92 -93
520 10 -19.3 90 -91 92 -93 94 -95
gaps between target/blanket sections
5000 4 -0.00129 -400 -401 402 403 -404 405 58 -50
5001 4 -0.00129 -400 -401 402 403 -404 405 51 -52 (#500) (#501)
5002 4 -0.00129 -400 -401 402 403 -404 405 53 -54
5003 4 -0.00129 -400 -401 402 403 -404 405 55 -56 (#510) (#511)
5004 4 -0.00129 -400 -401 402 403 -404 405 57 -59
surrounding of the whole setup
10000 0 500
```

c SURFACE CARD
*cylinder with radius of 4.2 cm*
1 cz 4.2
*z planes for Fe at the out of the beam tube*
2 pz -100.5
3 pz -100 4 cz 15
*z planes for target and blanket*
50 pz 0
51 pz 11.4
52 pz 12.2
53 pz 23.6
54 pz 24.4
55 pz 35.8
56 pz 36.6
57 pz 48
58 pz -1.25
59 pz 49.25
70 pz 0.5
71 pz 10.9
72 py 0
*z planes for activation samples*
79 pz 11.8
81 pz 11.805
82 py 2
83 py 4
84 py 10
85 py 12
86 pz 36.2
87 pz 36.205
90 py 11.8
91 py 11.805
92 px -1
93 px 1
94 pz 16.9
95 pz 18.9
*big hexagon for fill with lattice*
100 py 11.20
101 p 1 0.57735 0 12.93265
102 p -1 0.57735 0 -12.93265
103 p 1 0.57735 0 -12.93265
104 p -1 0.57735 0 12.93265

105 py -11.2
*small hexagon for the lattice definition*
200 px -1.807573351
201 px 1.807573351
202 p 0.577350269 -1 0 2.087205922
203 p 0.577350269 -1 0 -2.087205922
204 p -0.577350269 -1 0 2.087205922
205 p -0.577350269 -1 0 -2.087205922
*definition of U-rod inside the lattice*
250 cz 1.6881
251 cz 1.8
252 pz 0.1119
253 pz 10.2881
254 pz 10.4
*polyethylene box and Cd-layer*
300 pz -30
301 pz 76
302 py -25
303 py -25.1
304 py 25
305 py 25.1
306 py -41.5
307 py 47.1
308 px -19.9
309 px -20
310 px 19.9
311 px 20
312 px -50
313 px 50
*details of polyethylene box (bottom, top)*
314 px -37.8
315 px 37.8
316 py -63.1
317 px -55
318 px 55
*wooden and iron plate under the target*
320 px -18.1
321 px 18.1
322 py -14.4
323 py -21.2
*details on setup iron plates*

350 px -13
351 px 13
352 py -13
353 py 13
354 pz 0.9
355 pz 10.5
358 cz 4.4
*hexagon in front of the target*
400 py 14
401 p 1 0.57735 0 16.16581
402 p -1 0.57735 0 -16.16581
403 p 1 0.57735 0 -16.16581
404 p -1 0.57735 0 16.16581
405 py -14
*planes for iron hexagon around U rods*
450 py 11.6
451 p 1 0.57735 0 13.39453
452 p -1 0.57735 0 -13.39453
453 p 1 0.57735 0 -13.39453
454 p -1 0.57735 0 13.39453
455 py -11.6
500 so 130

c DATA CARD
*neutrons, protons, photons, charged pions*
mode n h p /
*particles simulated in all cells*
*("*nr*" means repeat the preceding entry on the card n-times.)*
imp:n,h,p,/ 1 52r 0
*definitions of materials (material number,* 1000·*proton number+nucleon number, nuclide fraction in the material, libraries)*
$^{\mathrm{nat}}Pb$
m1 82204 1.4 82206 24.1 82207 22.1 82208 52.4 hlib=24h nlib=24c cond=1
$^{\mathrm{nat}}U$
m2 92238 99.2745 92235 0.72 92234 0.005 cond=1
*Al*
m3 13027 1 hlib=24h nlib=24c cond=1
*air*
m4 7000 -0.755
8000 -0.232
18000 -0.013

```
    hlib=24h nlib=24c plib=02p cond=0
polyethylene
m5 6012 1 1001 2 nlib=60c cond=0 mt5 poly.01t
Cd
m6 48000 1 cond=1
Fe
m8 26058 0.282 26057 2.119 26056 91.754 26054 5.845
     nlib=24c hlib=24h cond=1
wood or textolite
m9 1001 0.513066 1002 0.000080 6000 0.230081 8016 0.256773
     nlib=60c plib=02p cond=0
Au
m10 79197 1 nlib=60c cond=1
Neutron physics options
("nj" means jump n-times over the preceding entry and
take the default value.)
phys:n 1500 3j -1
Proton physics options
phys:h 1500 j -1 4j
Photon physics options
phys:p 1500 4j
Pion physics options
phys:/ 1500 4j
yields of the 197-Au(n,gamma)198-Au reaction
f4:n 500
fm4 0.0030574 10 102
f14:n 501
fm14 0.0030574 10 102
f24:n 510
fm24 0.0030574 10 102
f34:n 511
fm34 0.0030574 10 102
f44:n 520
fm44 0.0030574 10 102
energy binning
f104:n 500 e104 1.5 148i 150.5 175 26i 1525
f114:n 501 e114 1.5 148i 150.5 175 26i 1525
f124:n 510 e124 1.5 148i 150.5 175 26i 1525
f134:n 511 e134 1.5 148i 150.5 175 26i 1525
f144:n 520 e144 1.5 148i 150.5 175 26i 1525
f204:h 500 e204 1.5 148i 150.5 175 26i 1525
```

f214:h 501 e214 1.5 148i 150.5 175 26i 1525
f224:h 510 e224 1.5 148i 150.5 175 26i 1525
f234:h 511 e234 1.5 148i 150.5 175 26i 1525
f244:h 520 e244 1.5 148i 150.5 175 26i 1525
f304:/ 500 e304 1.5 148i 150.5 175 26i 1525
f314:/ 501 e314 1.5 148i 150.5 175 26i 1525
f324:/ 510 e324 1.5 148i 150.5 175 26i 1525
f334:/ 511 e334 1.5 148i 150.5 175 26i 1525
f344:/ 520 e344 1.5 148i 150.5 175 26i 1525
*INCL4 model*
lca 8j 2
*ABLA model*
lea 6j 2
*the number of incident particles (events)*
nps 1e6
*beam definition*
sdef par h erg 1500 sur 2 pos 0 0 -100.5 rad d1 dir 1 vec 0 0 1
si1 h 0 1.5
sp1 -21 1

# Appendix B
# Experimental yields

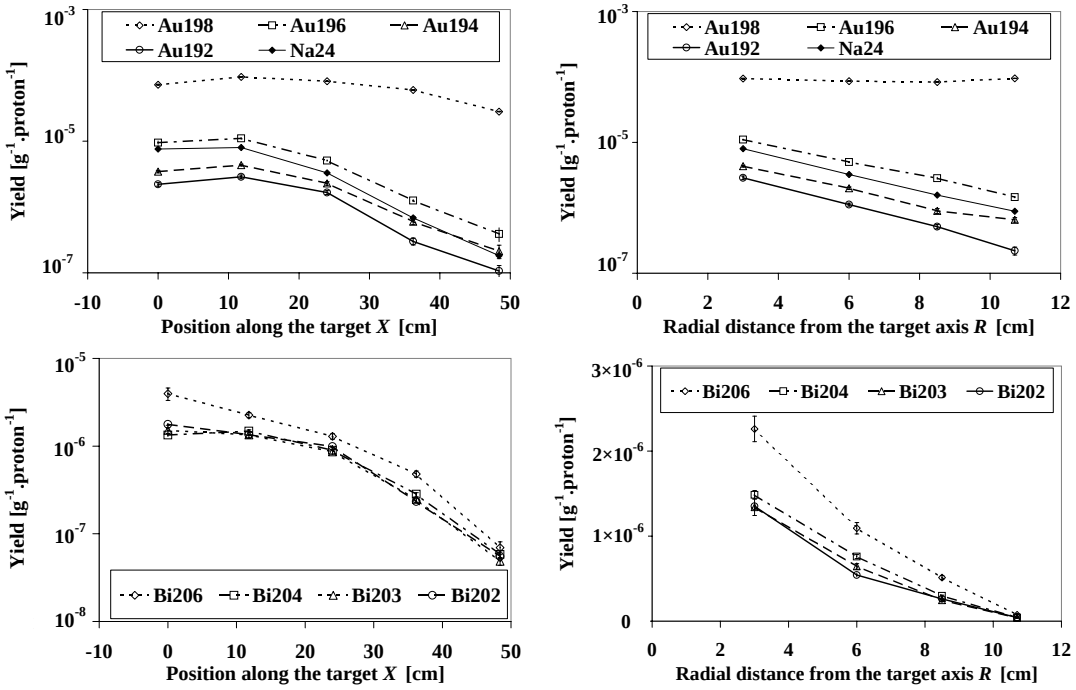


Figure B.1: Longitudinal (left) and radial (right) distributions of the experimental yields of nuclei produced in Al-, Au-, and Bi-foils (0.7 GeV experiment). The lines linking experimental points are delineated to guide readers' eyes.

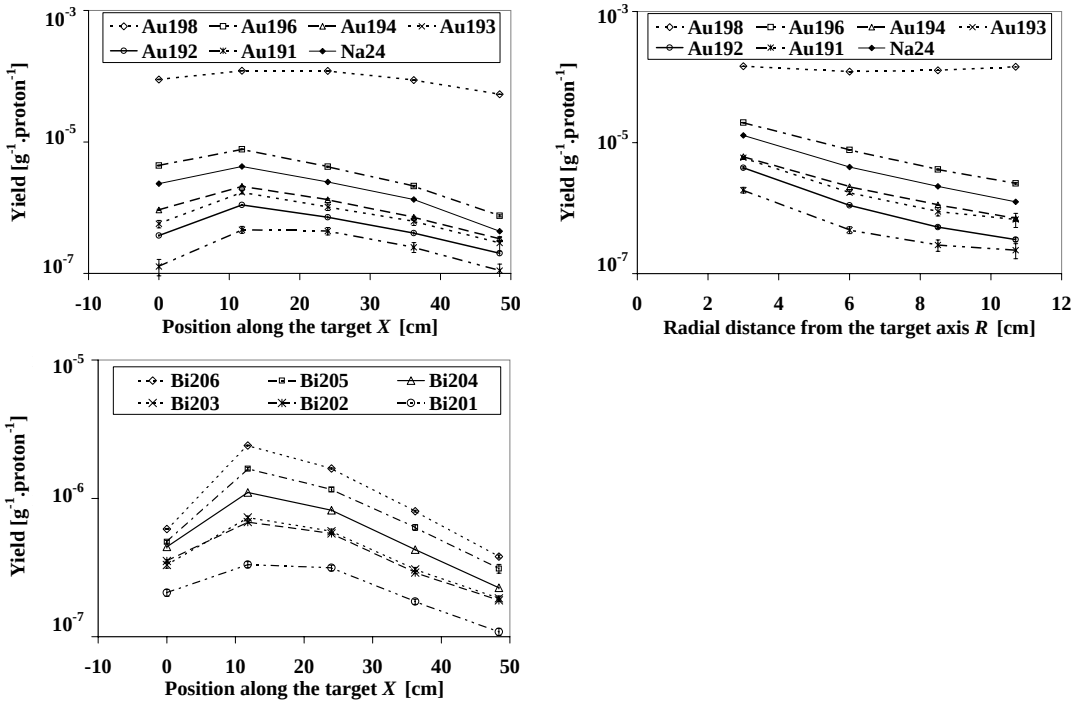


Figure B.2: Longitudinal (left) and radial (right) distributions of the experimental yields of nuclei produced in Al-, Au-, and Bi-foils (1.0 GeV experiment). The lines linking experimental points are delineated to guide readers' eyes.

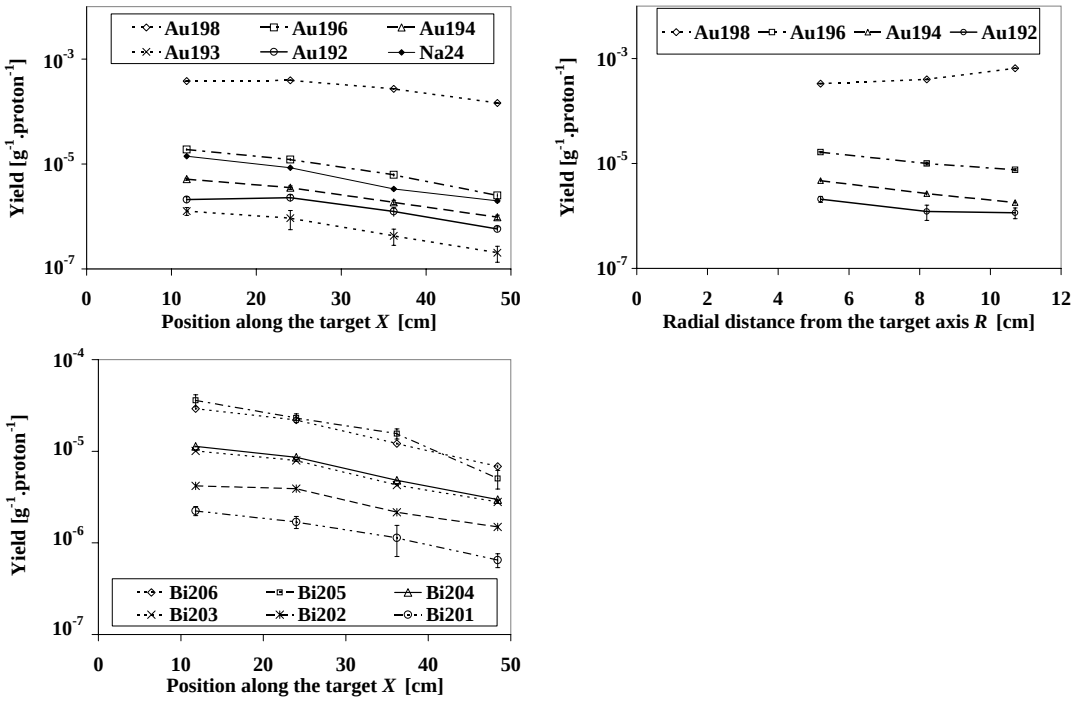


Figure B.3: Longitudinal (left) and radial (right) distributions of the experimental yields of nuclei produced in Al-, Au-, and Bi-foils (2.0 GeV experiment). The lines linking experimental points are delineated to guide readers' eyes.

Table B.1: The experimental yields of nuclei produced in Al- and Au-foils (0.7 GeV experiment).

| Foil | $^{27}$Al | $^{197}$Au | | | |
|---|---|---|---|---|---|
| Reaction | (n,$\alpha$) | (n,$\gamma$) | (n,2n) | (n,4n) | (n,6n) |
| Product | $^{24}$Na | $^{198}$Au | $^{196}$Au | $^{194}$Au | $^{192}$Au |
| $E_{thresh}$ [MeV] | 5.5 | - | 8.1 | 23 | 39 |
| $T_{1/2}$ [h] | 15 | 65 | 148 | 38 | 5 |
| $X$ [cm] | Longitudinal yields [$10^{-6}\cdot$g$^{-1}\cdot$ proton$^{-1}$], $R = 3$ cm | | | | |
| 0.0 | 7.62(8) | 72.1(14) | 9.5(5) | 3.45(15) | 2.21(14) |
| 11.8 | 7.98(12) | 94.6(12) | 11.05(24) | 4.33(15) | 2.88(19) |
| 24.0 | 3.30(6) | 81.4(7) | 5.07(13) | 2.29(14) | 1.66(11) |
| 36.2 | 0.85(4) | 59.9(3) | 1.25(4) | 0.60(6) | 0.30(4) |
| 48.4 | 0.228(19) | 28.1(3) | 0.39(9) | 0.21(5) | 0.107(22) |
| $R$ [cm] | Radial yields [$10^{-6}\cdot$g$^{-1}\cdot$ proton$^{-1}$], $X = 11.8$ cm | | | | |
| 3.0 | 9.95(15) | 94.6(12) | 11.05(24) | 4.33(15) | 2.88(19) |
| 6.0 | 4.03(7) | 86.2(11) | 5.01(10) | 1.99(8) | 1.12(6) |
| 8.5 | 1.95(4) | 83.8(6) | 2.83(10) | 0.90(8) | 0.52(4) |
| 10.7 | 1.10(7) | 95.0(7) | 1.46(4) | 0.66(5) | 0.22(3) |

Table B.2: The experimental yields of nuclei produced in Bi-foils (0.7 GeV experiment).

| Foil | $^{209}$Bi | | | |
|---|---|---|---|---|
| Reaction | (n,4n) | (n,6n) | (n,7n) | (n,8n) |
| Product | $^{206}$Bi | $^{204}$Bi | $^{203}$Bi | $^{202}$Bi |
| $E_{thresh}$ [MeV] | 22 | 38 | 45 | 53 |
| $T_{1/2}$ [h] | 150 | 11 | 12 | 2 |
| $X$ [cm] | Longitudinal yields [$10^{-6}\cdot$g$^{-1}\cdot$ proton$^{-1}$], $R = 3$ cm | | | |
| 0.0 | 4.0(6) | 1.34(5) | 1.51(11) | 1.77(4) |
| 11.8 | 2.26(15) | 1.49(5) | 1.34(10) | 1.35(4) |
| 24.0 | 1.29(9) | 0.896(28) | 0.86(5) | 0.990(26) |
| 36.2 | 0.48(4) | 0.283(12) | 0.247(17) | 0.233(7) |
| 48.4 | 0.070(12) | 0.058(4) | 0.049(5) | 0.055(3) |
| $R$ [cm] | Radial yields [$10^{-6}\cdot$g$^{-1}\cdot$ proton$^{-1}$], $X = 11.8$ cm | | | |
| 3.0 | 2.26(15) | 1.49(5) | 1.34(10) | 1.35(4) |
| 6.0 | 1.09(7) | 0.759(24) | 0.64(3) | 0.543(22) |
| 8.5 | 0.512(24) | 0.297(10) | 0.248(15) | 0.263(10) |
| 10.7 | 0.074(13) | 0.0429(32) | 0.039(5) | 0.0421(30) |

Table B.3: The experimental yields of nuclei produced in Al- and Au-foils (1.0 GeV experiment).

| Foil | $^{27}$Al | $^{197}$Au | | | | | |
|---|---|---|---|---|---|---|---|
| Reaction | (n,$\alpha$) | (n,$\gamma$) | (n,2n) | (n,4n) | (n,5n) | (n,6n) | (n,7n) |
| Product | $^{24}$Na | $^{198}$Au | $^{196}$Au | $^{194}$Au | $^{193}$Au | $^{192}$Au | $^{191}$Au |
| $E_{thresh}$ [MeV] | 5.5 | - | 8.1 | 23 | 30 | 39 | 46 |
| $T_{1/2}$ [h] | 15 | 65 | 148 | 38 | 18 | 5 | 3 |
| $X$ [cm] | Longitudinal yields [$10^{-6}\cdot$g$^{-1}\cdot$ proton$^{-1}$], $R = 6$ cm | | | | | | |
| 0.0 | 2.31(4) | 89.0(6) | 4.37(6) | 0.926(22) | 0.57(8) | 0.377(18) | 0.13(4) |
| 11.8 | 4.24(6) | 121.4(8) | 7.72(9) | 2.12(5) | 1.72(10) | 1.10(3) | 0.46(6) |
| 24.0 | 2.46(4) | 120.6(8) | 4.22(8) | 1.33(4) | 1.02(12) | 0.72(4) | 0.44(6) |
| 36.2 | 1.332(23) | 87.4(6) | 2.12(6) | 0.71(3) | 0.62(8) | 0.411(23) | 0.25(4) |
| 48.4 | 0.439(10) | 53.2(4) | 0.75(3) | 0.334(17) | 0.29(7) | 0.203(16) | 0.11(3) |
| $R$ [cm] | Radial yields [$10^{-6}\cdot$g$^{-1}\cdot$ proton$^{-1}$], $X = 11.8$ cm | | | | | | |
| 3.0 | 12.86(14) | 146.8(12) | 20.17(17) | 6.09(8) | 5.86(27) | 4.11(16) | 1.88(19) |
| 6.0 | 4.24(6) | 121.4(8) | 7.72(9) | 2.12(5) | 1.72(10) | 1.10(3) | 0.46(6) |
| 8.5 | 2.15(4) | 127.1(9) | 3.89(7) | 1.13(3) | 0.89(13) | 0.51(3) | 0.27(5) |
| 10.7 | 1.24(3) | 143.6(9) | 2.39(7) | 0.70(3) | 0.67(16) | 0.330(22) | 0.23(6) |

Table B.4: The experimental yields of nuclei produced in Bi-foils (1.0 GeV experiment).

| Foil | $^{209}$Bi | | | | | |
|---|---|---|---|---|---|---|
| Reaction | (n,4n) | (n,5n) | (n,6n) | (n,7n) | (n,8n) | (n,9n) |
| Product | $^{206}$Bi | $^{205}$Bi | $^{204}$Bi | $^{203}$Bi | $^{202}$Bi | $^{201}$Bi |
| $E_{thresh}$ [MeV] | 22 | 30 | 38 | 45 | 53 | 61 |
| $T_{1/2}$ [h] | 150 | 367 | 11 | 12 | 2 | 2 |
| $X$ [cm] | Longitudinal yields [$10^{-6}\cdot$g$^{-1}\cdot$ proton$^{-1}$], $R = 6$ cm | | | | | |
| 0.0 | 0.601(6) | 0.485(11) | 0.446(10) | 0.330(17) | 0.353(6) | 0.208(12) |
| 11.8 | 2.409(19) | 1.639(38) | 1.101(10) | 0.728(18) | 0.675(11) | 0.332(17) |
| 24.0 | 1.644(19) | 1.16(4) | 0.821(13) | 0.579(20) | 0.558(8) | 0.315(15) |
| 36.2 | 0.808(11) | 0.616(31) | 0.426(5) | 0.307(10) | 0.291(5) | 0.179(8) |
| 48.4 | 0.380(9) | 0.310(22) | 0.226(4) | 0.189(8) | 0.1832(33) | 0.108(6) |

Table B.5: The experimental yields of nuclei produced in Al- and Au-foils (1.5 GeV experiment).

| Foil | $^{27}$Al | $^{197}$Au | | | | | |
|---|---|---|---|---|---|---|---|
| Reaction | (n,$\alpha$) | (n,$\gamma$) | (n,2n) | (n,4n) | (n,5n) | (n,6n) | (n,7n) |
| Product | $^{24}$Na | $^{198}$Au | $^{196}$Au | $^{194}$Au | $^{193}$Au | $^{192}$Au | $^{191}$Au |
| $E_{thresh}$ [MeV] | 5.5 | - | 8.1 | 23 | 30 | 39 | 46 |
| $T_{1/2}$ [h] | 15 | 65 | 148 | 38 | 18 | 5 | 3 |
| $X$ [cm] | Longitudinal yields [$10^{-6}\cdot$g$^{-1}\cdot$ proton$^{-1}$], $R = 3$ cm | | | | | | |
| 0.0 | 7.5(3) | 120.8(29) | 12.5(3) | 2.57(8) | 0.94(7) | 1.18(6) | 0.55(14) |
| 11.8 | 16(7) | 215(5) | 25.1(6) | 6.97(20) | 2.87(17) | 3.74(19) | 1.88(21) |
| 24.0 | 8.7(4) | 194(5) | 15.4(3) | 4.41(13) | 1.78(11) | 2.65(13) | 1.38(19) |
| 36.2 | 5.55(25) | 141(3) | 9.46(23) | 2.72(8) | 1.22(9) | 1.78(9) | 0.94(13) |
| 48.4 | 2.23(10) | 74.3(19) | 3.46(9) | 1.22(4) | 0.64(5) | 0.91(5) | 0.50(10) |
| $R$ [cm] | Radial yields [$10^{-6}\cdot$g$^{-1}\cdot$ proton$^{-1}$], $X = 11.8$ cm | | | | | | |
| 3.0 | 16.0(7) | 215(5) | 25.1(6) | 6.97(20) | 2.87(17) | 3.74(19) | 1.88(21) |
| 6.0 | 8.9(4) | 195(5) | 15.2(4) | 4.20(13) | 1.70(11) | 2.45(13) | 1.30(33) |
| 8.5 | 5.30(24) | 174(4) | 9.40(21) | 2.53(8) | 0.98(9) | 1.36(7) | 0.74(14) |
| 13.5 | 2.51(11) | 173(4) | 6.01(15) | 1.64(5) | 0.56(7) | 0.90(5) | 0.51(17) |

Table B.6: The experimental yields of nuclei produced in Bi-foils (1.5 GeV experiment).

| Foil | $^{209}$Bi | | | | | |
|---|---|---|---|---|---|---|
| Reaction | (n,4n) | (n,5n) | (n,6n) | (n,7n) | (n,8n) | (n,9n) |
| Product | $^{206}$Bi | $^{205}$Bi | $^{204}$Bi | $^{203}$Bi | $^{202}$Bi | $^{201}$Bi |
| $E_{thresh}$ [MeV] | 22 | 30 | 38 | 45 | 53 | 61 |
| $T_{1/2}$ [h] | 150 | 367 | 11 | 12 | 2 | 2 |
| $X$ [cm] | Longitudinal yields [$10^{-6}$·g$^{-1}$· proton$^{-1}$], $R = 3$ cm | | | | | |
| 0.0 | 3.92(18) | 2.51(11) | 1.19(5) | 0.712(32) | 0.706(32) | 0.260(12) |
| 11.8 | 8.57(39) | 5.31(24) | 3.39(15) | 2.27(10) | 3.13(14) | 1.27(6) |
| 24.0 | 5.55(25) | 3.72(17) | 2.31(11) | 1.62(7) | 2.04(9) | 0.87(4) |
| 36.2 | 3.61(16) | 2.58(12) | 1.55(7) | 1.10(5) | 1.47(7) | 0.565(26) |
| 48.4 | 1.42(6) | 1.09(5) | 0.712(32) | 0.450(20) | 0.682(31) | 0.267(12) |
| $X$ [cm] | Radial yields [$10^{-6}$·g$^{-1}$· proton$^{-1}$], $X = 11.8$ cm | | | | | |
| 3.0 | 8.57(39) | 5.31(24) | 3.39(15) | 2.27(10) | 3.13(14) | 1.27(6) |
| 6.0 | 4.94(22) | 2.88(13) | 1.19(9) | 1.17(5) | 1.93(9) | 0.708(32) |
| 8.5 | 3.08(14) | 1.97(9) | 1.10(5) | 0.687(31) | 0.97(4) | 0.345(16) |
| 13.5 | 2.22(10) | 1.36(6) | 0.77(4) | 0.477(22) | 0.639(29) | 0.213(10) |

Table B.7: The experimental yields of nuclei produced in Co-foils (1.5 GeV experiment).

| Foil | $^{59}$Co | | | | |
|---|---|---|---|---|---|
| Reaction | (n,$\gamma$) | (n,2n) | (n,3n) | (n,4n) | (n,5n) |
| Product | $^{60}$Co | $^{58}$Co | $^{57}$Co | $^{56}$Co | $^{55}$Co |
| $E_{thresh}$ [MeV] | - | 10.6 | 19.4 | 30.9 | 41.2 |
| $T_{1/2}$ [h] | 46174 | 1700 | 6523 | 1854 | 18 |
| $X$ [cm] | Longitudinal yields [$10^{-6}\cdot$g$^{-1}\cdot$ proton$^{-1}$], $R = 3$ cm | | | | |
| 0.0 | 72.23(15) | 17.8(8) | 3.30(15) | 0.522(24) | 0.0248(11) |
| 11.8 | 94(4) | 27.68(6) | 7.21(33) | 1.13(5) | 0.087(4) |
| 24.0 | 100(5) | 20.9(9) | 5.51(25) | 1.02(5) | 0.0813(37) |
| 36.2 | 73.6(33) | 10.8(5) | 3.07(14) | 0.724(33) | 0.0514(23) |
| 48.4 | 39.3(18) | 4.39(20) | 1.25(6) | 0.336(15) | 0.0274(12) |
| $X$ [cm] | Radial yields [$10^{-6}\cdot$g$^{-1}\cdot$ proton$^{-1}$], $X = 11.8$ cm | | | | |
| 3.0 | 94(4) | 27.7(13) | 7.21(33) | 1.13(5) | |
| 6.0 | 96(4) | 20.9(10) | 5.00(23) | 0.820(37) | |
| 8.5 | 100.7(39) | 12.9(6) | 3.07(14) | 0.509(23) | |
| 13.5 | 105(5) | 8.8(4) | 2.07(9) | 0.377(17) | |

Table B.8: The experimental yields of nuclei produced in Al- and Au-foils (2.0 GeV experiment).

| Foil | $^{27}$Al | $^{197}$Au | | | | |
|---|---|---|---|---|---|---|
| Reaction | (n,$\alpha$) | (n,$\gamma$) | (n,2n) | (n,4n) | (n,5n) | (n,6n) |
| Product | $^{24}$Na | $^{198}$Au | $^{196}$Au | $^{194}$Au | $^{193}$Au | $^{192}$Au |
| $E_{thresh}$ [MeV] | 5.5 | - | 8.1 | 23 | 30 | 39 |
| $T_{1/2}$ [h] | 15 | 65 | 148 | 38 | 18 | 5 |
| $X$ [cm] | Longitudinal yields [$10^{-6}$·g$^{-1}$· proton$^{-1}$], $R$ = 5.2 cm | | | | | |
| 11.8 | 14.15(38) | 381(5) | 18.9(8) | 5.14(24) | 1.26(22) | 2.10(29) |
| 24.0 | 8.46(23) | 395(5) | 12.2(6) | 3.54(28) | 0.93(37) | 2.28(32) |
| 36.2 | 3.35(13) | 271.6(33) | 6.21(36) | 1.86(17) | 0.43(15) | 1.24(23) |
| 48.4 | 1.98(9) | 145.0(17) | 2.52(20) | 0.97(10) | 0.20(7) | 0.58(6) |
| $R$ [cm] | Radial yields [$10^{-6}$·g$^{-1}$· proton$^{-1}$], $X$ = 11.8 cm | | | | | |
| 5.2 | | 333(4) | 16.4(5) | 4.71(27) | | 2.08(28) |
| 8.2 | | 400(5) | 10.0(6) | 2.67(20) | | 1.22(39) |
| 10.7 | | 654(7) | 7.58(34) | 1.80(11) | | 1.15(27) |

Table B.9: The experimental yields of nuclei produced in Bi-foils (2.0 GeV experiment).

| Foil | $^{209}$Bi | | | | | |
|---|---|---|---|---|---|---|
| Reaction | (n,4n) | (n,5n) | (n,6n) | (n,7n) | (n,8n) | (n,9n) |
| Product | $^{206}$Bi | $^{205}$Bi | $^{204}$Bi | $^{203}$Bi | $^{202}$Bi | $^{201}$Bi |
| $E_{thresh}$ [MeV] | 22 | 30 | 38 | 45 | 53 | 61 |
| $T_{1/2}$ [h] | 150 | 367 | 11 | 12 | 2 | 2 |
| $X$ [cm] | Longitudinal yields [$10^{-6}\cdot$g$^{-1}\cdot$ proton$^{-1}$], $R = 5.2$ cm | | | | | |
| 11.8 | 29.1(6) | 36(6) | 11.33(14) | 10.08(22) | 4.19(7) | 2.23(31) |
| 24.0 | 21.95(38) | 23.1(26) | 8.61(10) | 7.94(19) | 3.91(9) | 1.69(23) |
| 36.2 | 12.13(33) | 15.6(21) | 4.82(9) | 4.28(14) | 2.16(6) | 1.13(18) |
| 48.4 | 6.84(24) | 5.0(12) | 2.97(5) | 2.80(12) | 1.49(5) | 0.65(13) |

# Appendix C
# Neutron spectra simulations

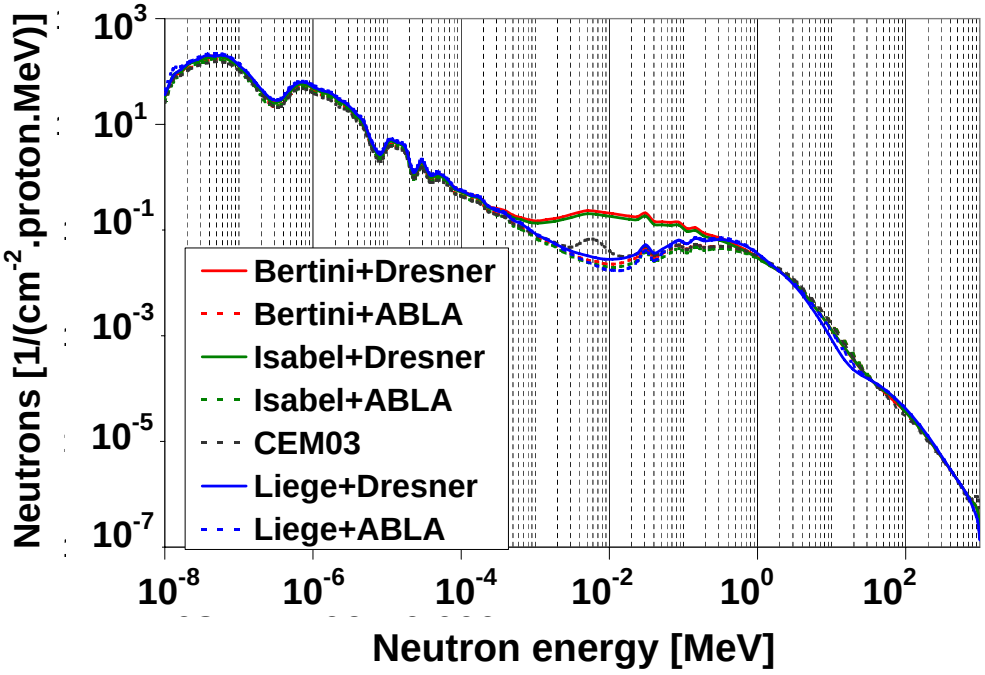


Figure C.1: Neutron spectra (produced in the first target section) in log-log scale. MCNPX simulations of the 1.0 GeV proton experiment. Neutron spectra are normalized per unit of energy in each bin (equidistant logarithmic energy binning with 100 bins in the whole scale). All combinations of available physics models in 2.6.C version were used.

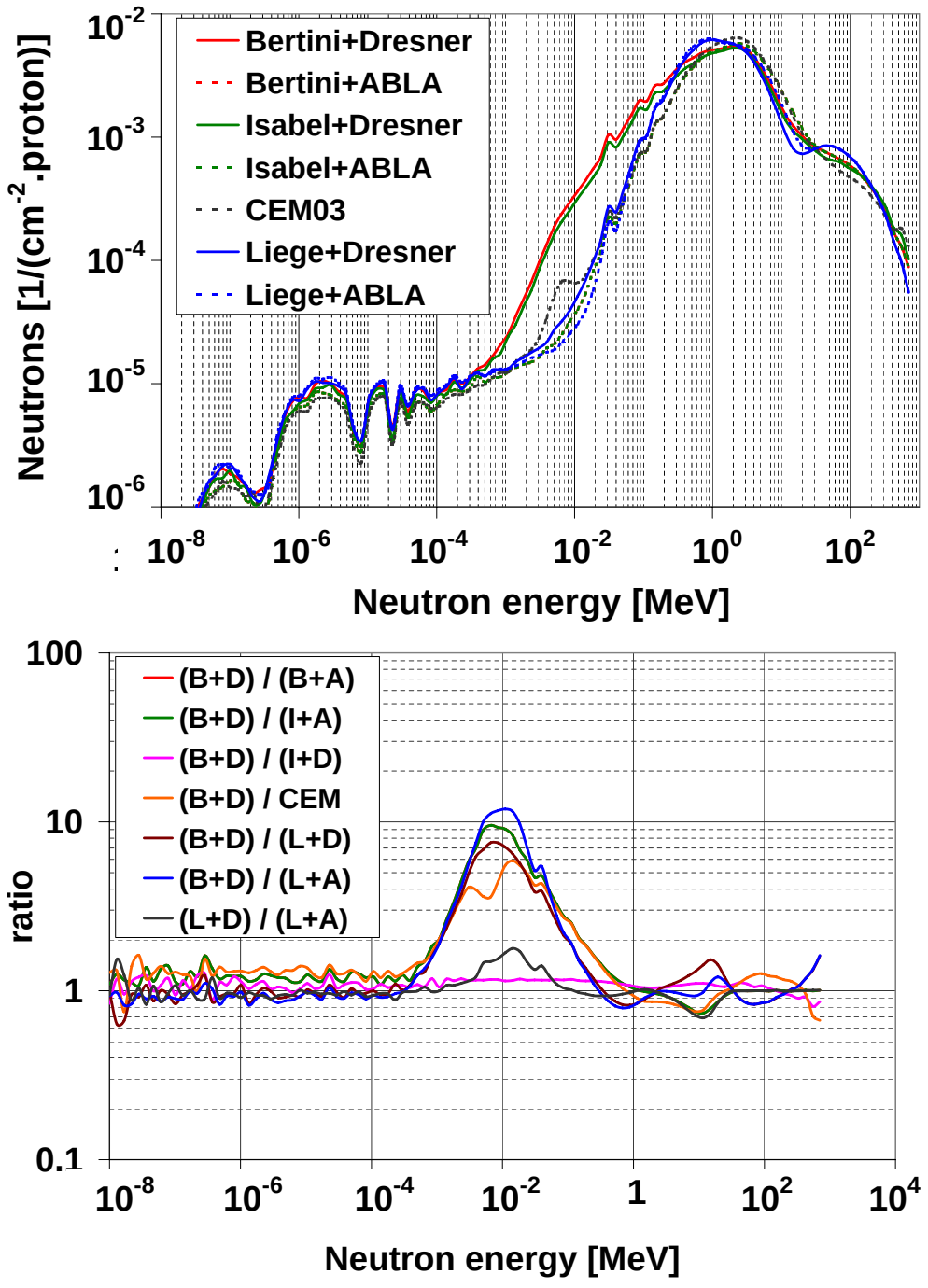


Figure C.2: Neutron spectra (produced in the first target section) in log-log scale (top) and ratios of neutron spectra from above figure (bottom). MCNPX simulations of the 0.7 GeV proton experiment. Equidistant logarithmic energy binning with 100 intervals. All combinations of available physics models in 2.6.C version were used.

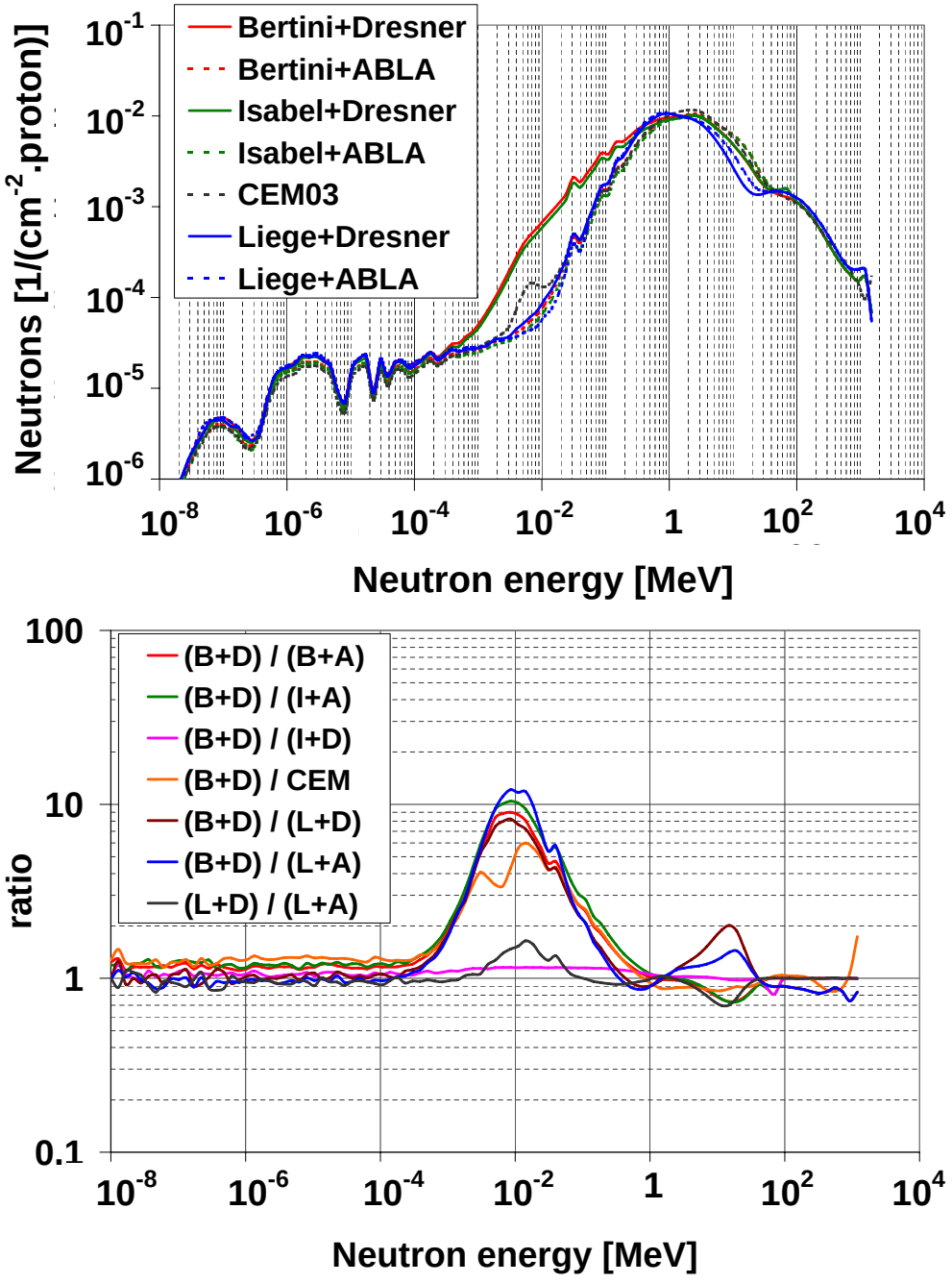


Figure C.3: Neutron spectra (produced in the first target section) in log-log scale (top) and ratios of neutron spectra from above figure (bottom). MCNPX simulations of the 1.5 GeV proton experiment. Equidistant logarithmic energy binning with 100 intervals. All combinations of available physics models in 2.6.C version were used.

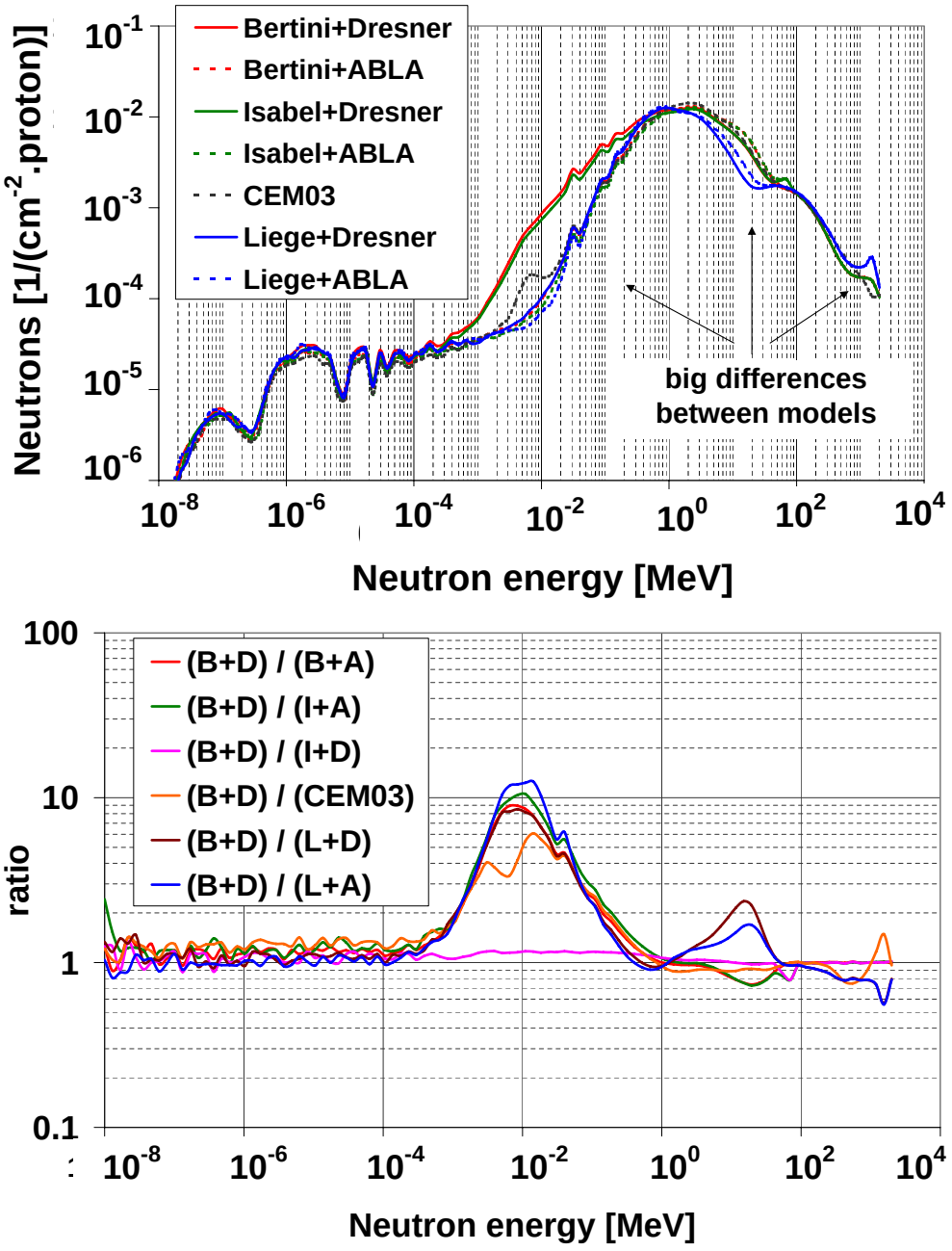


Figure C.4: Neutron spectra (produced in the first target section) in log-log scale (top) and ratios of neutron spectra from above figure (bottom). MCNPX simulations of the 2.0 GeV proton experiment. Equidistant logarithmic energy binning with 100 intervals. All combinations of available physics models in 2.6.C version were used.

# Appendix D
# The (n,$x$n)- and (p,p($x-1$)n)-cross-sections calculated with TALYS and MCNPX

First, I show an example of the TALYS input file used in the simulations presented in this thesis. Italic font is used for comments.

*neutron as an incident particle*
projectile n
*gold as a target element*
element Au
*197 as a nucleon number*
mass 197
*the name of file with a list of energies (in MeV) of the incident particle*
energy range

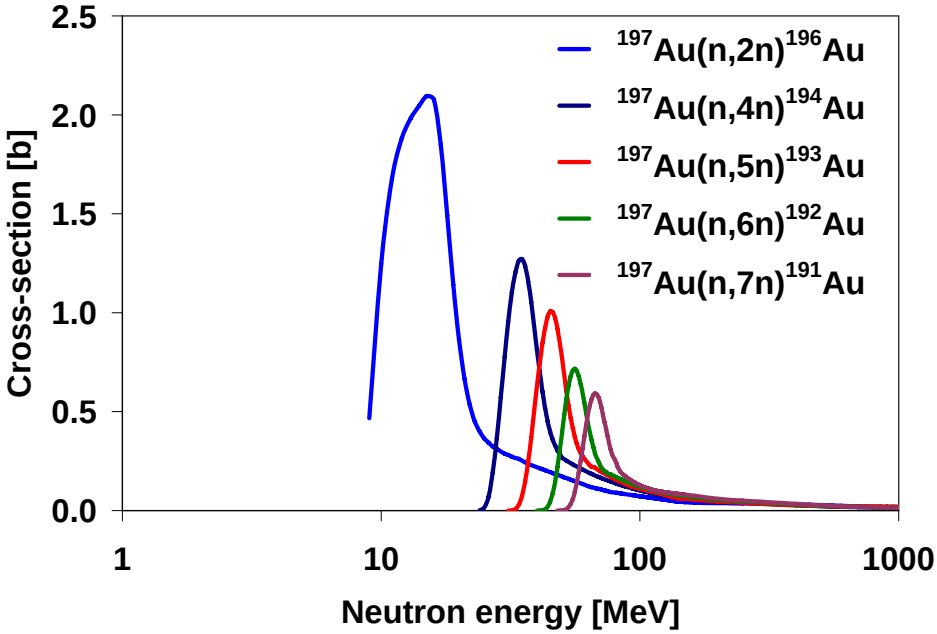


Figure D.1: The $^{197}$Au(n,$x$n)-cross-sections calculated with TALYS (below 150 MeV) and MCNPX (above 150 MeV).

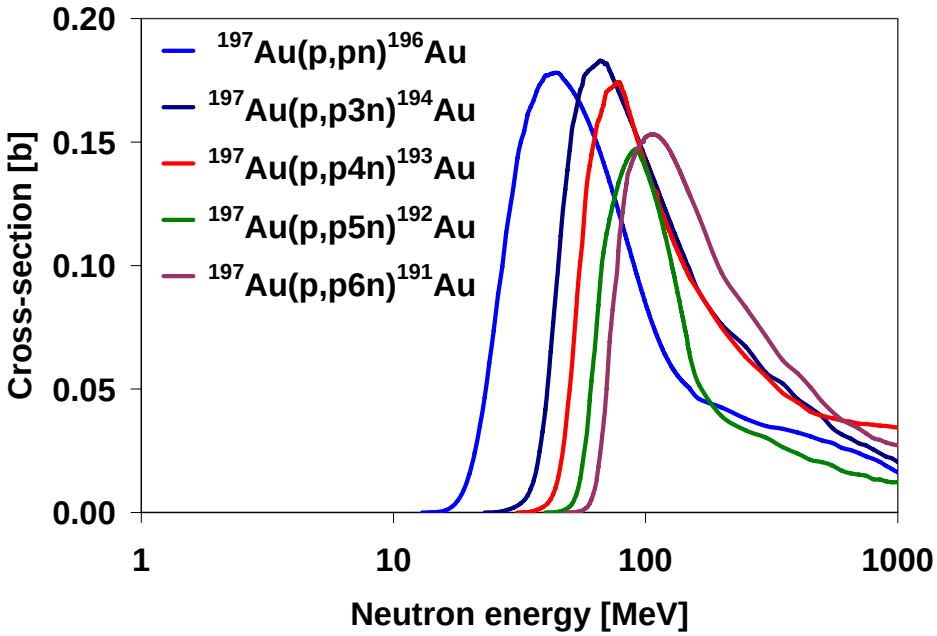


Figure D.2: The $^{197}$Au(p,p($x-1$)n)-cross-sections calculated with TALYS (below 150 MeV) and MCNPX (above 150 MeV).

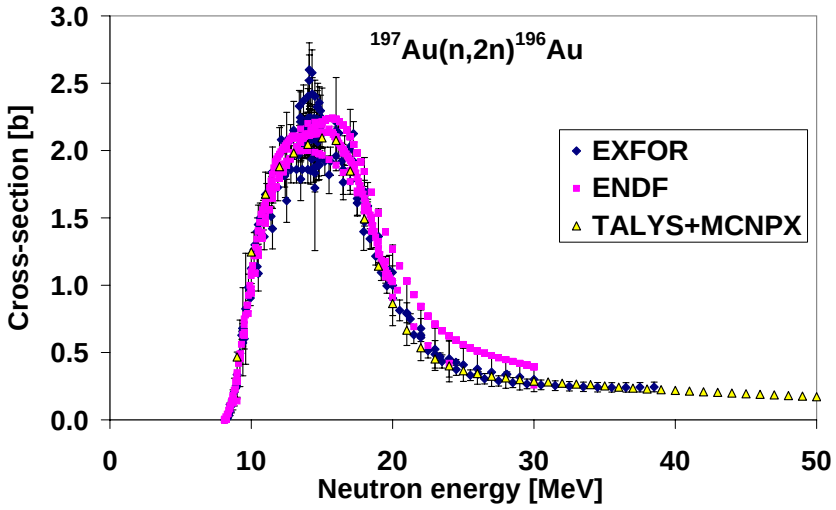


Figure D.3: Comparison of TALYS cross-sections with experimental and evaluated cross-sections of the $^{197}$Au(n,2n)$^{196}$Au.

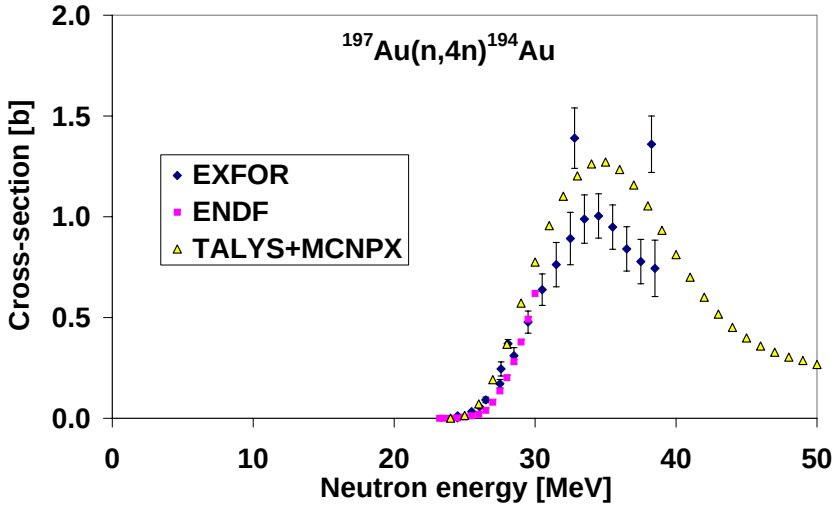


Figure D.4: Comparison of TALYS cross-sections with experimental and evaluated cross-sections of $^{197}$Au(n,4n)$^{194}$Au.

# Appendix E
# Neutron emission on a U-target

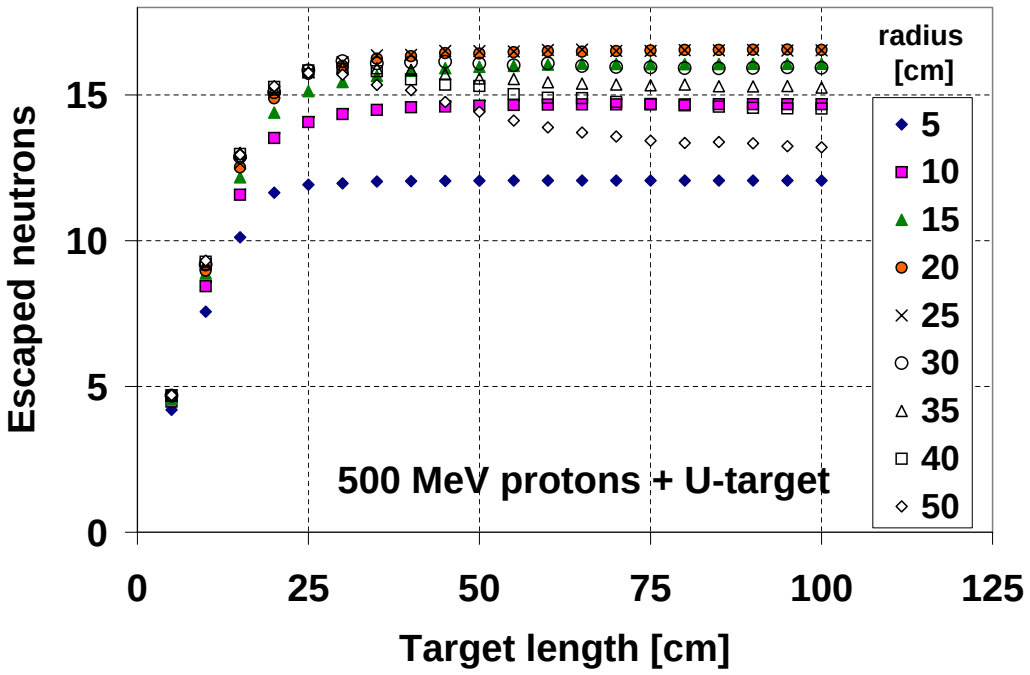


Figure E.1: Numbers of neutrons escaped from surface of a U-target irradiated with the 0.5 GeV proton beams in dependence on target size. MCNPX simulation (Bertini+Dresner).

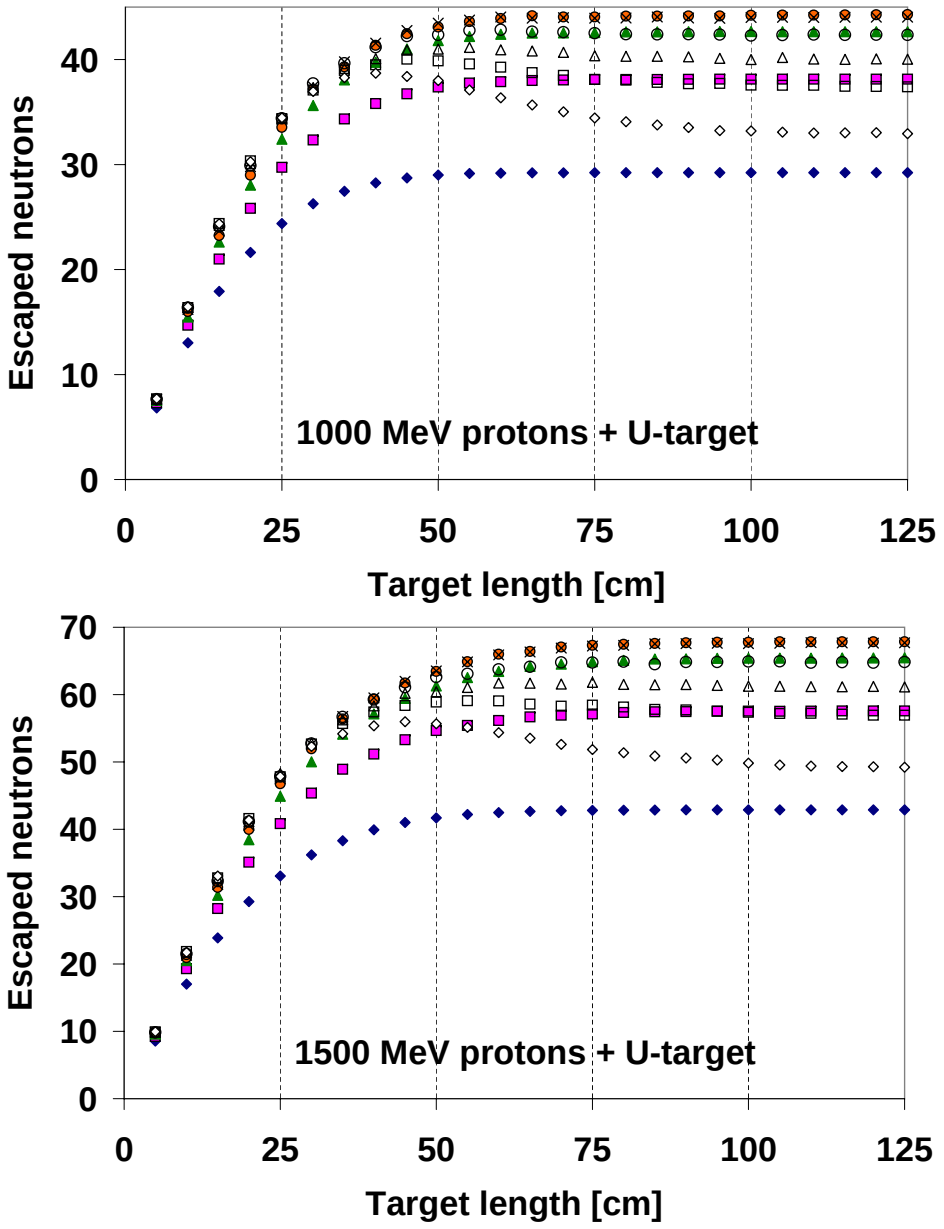


Figure E.2: Numbers of neutrons escaped from surface of a U-target irradiated with the 1.0 and 1.5 GeV proton beams in dependence on target size. The symbols refer to the values of a target radius with the same convention as in **Fig. E.1**. MCNPX simulation (Bertini+Dresner).

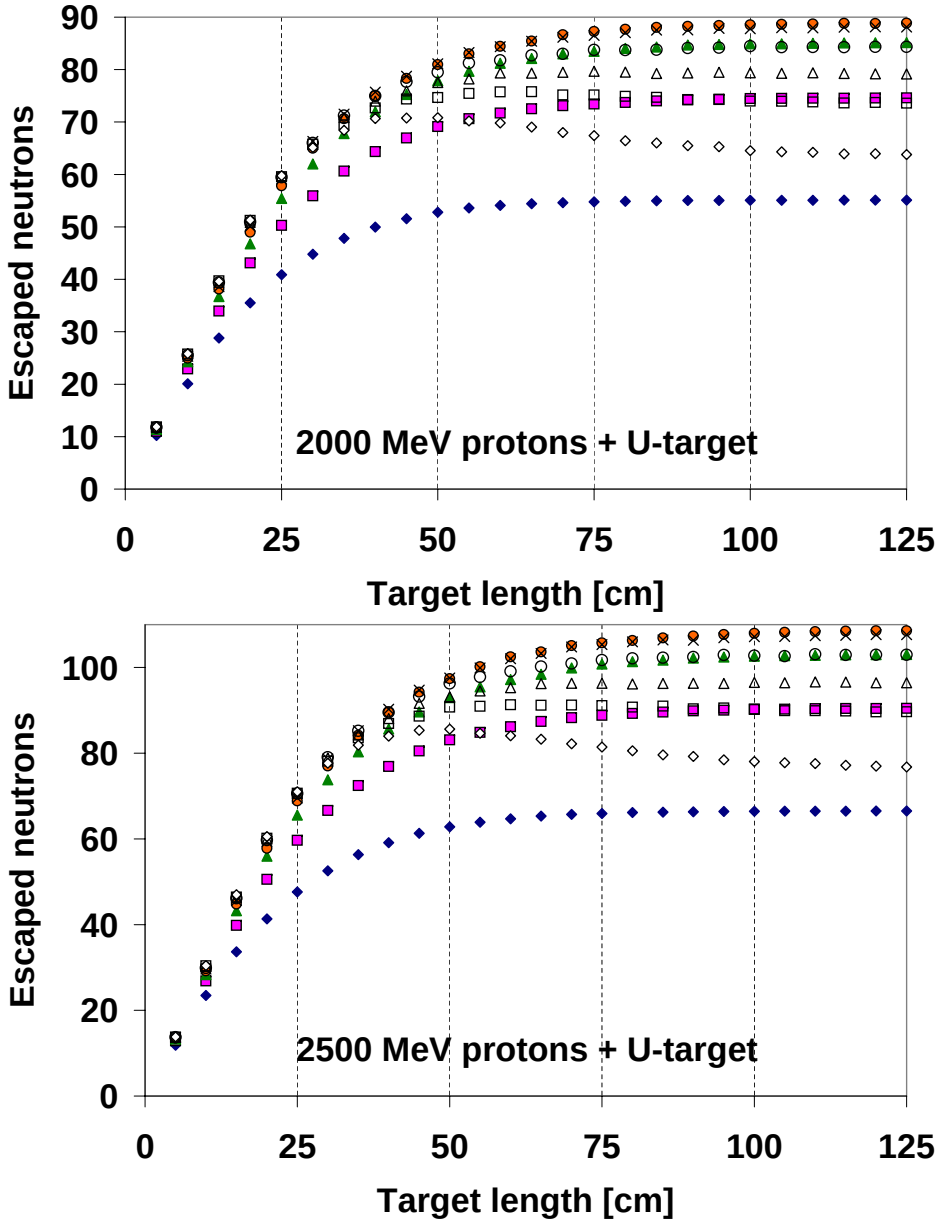


Figure E.3: Numbers of neutrons escaped from surface of a U-target irradiated with the 2.0 and 2.5 GeV proton beams in dependence on target size. The symbols refer to the values of a target radius with the same convention as in **Fig. E.1**. MCNPX simulation (Bertini+Dresner).

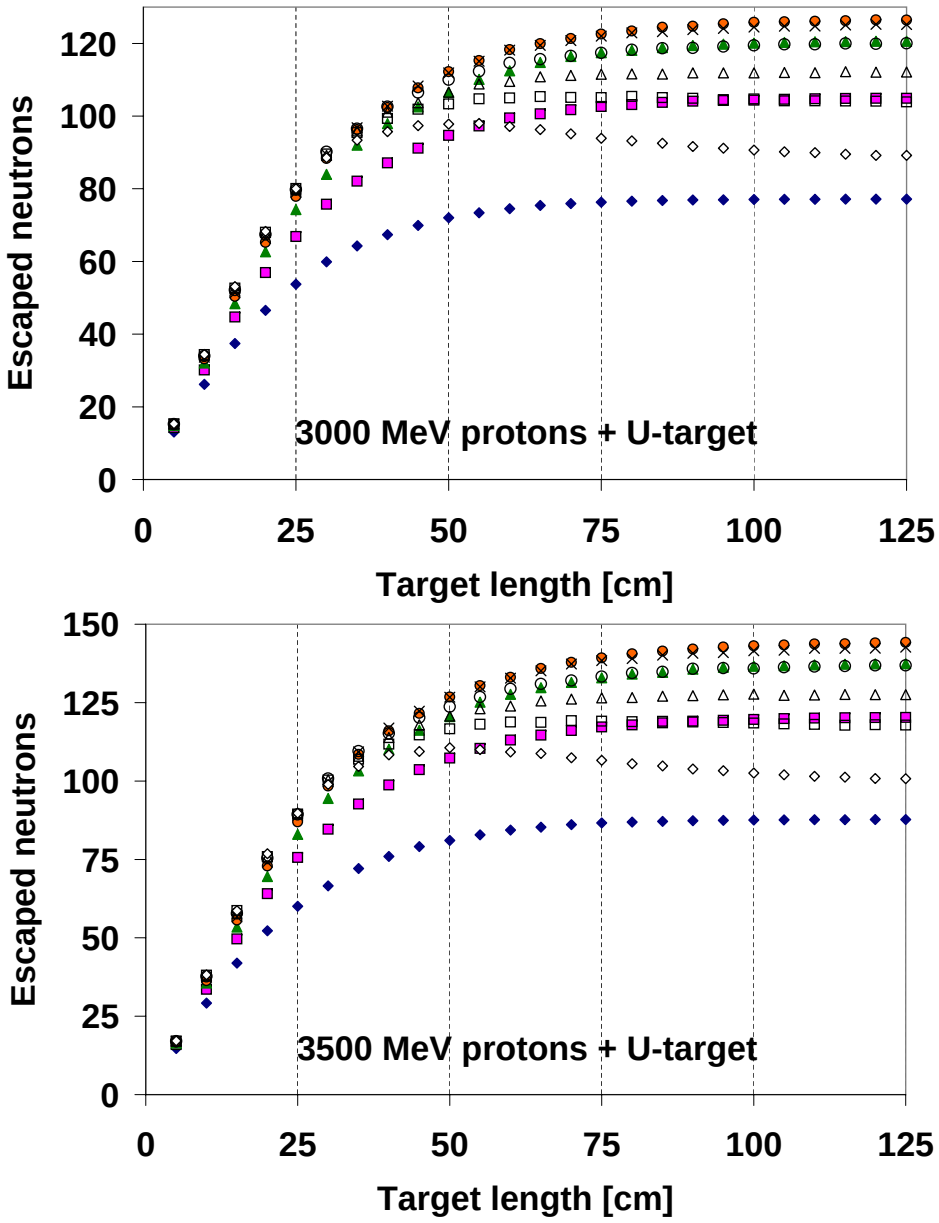


Figure E.4: Numbers of neutrons escaped from surface of a U-target irradiated with the 3.0 and 3.5 GeV proton beams in dependence on target size. The symbols refer to the values of a target radius with the same convention as in **Fig. E.1**. MCNPX simulation (Bertini+Dresner).

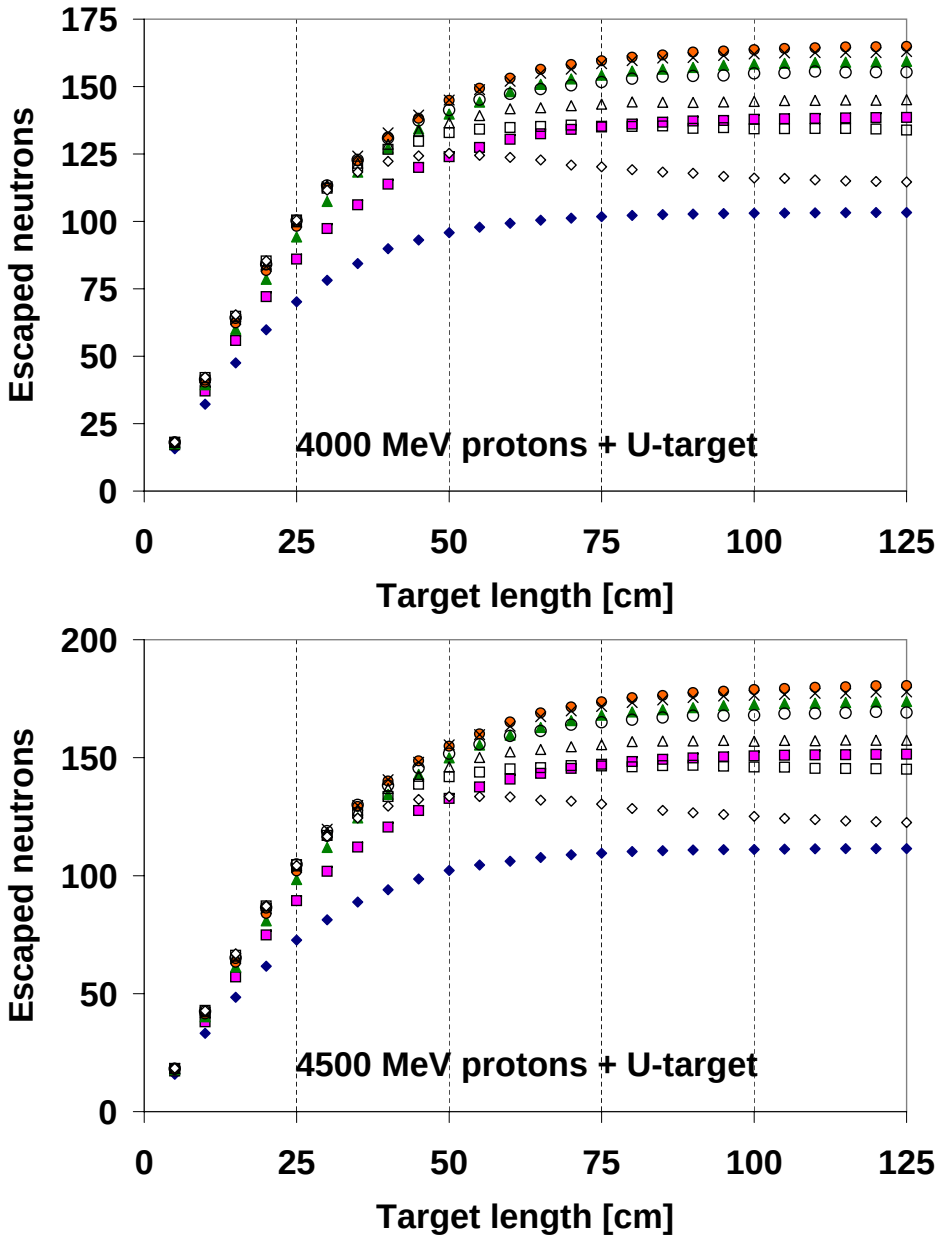


Figure E.5: Numbers of neutrons escaped from surface of a U-target irradiated with the 4.0 and 4.5 GeV proton beams in dependence on target size. The symbols refer to the values of a target radius with the same convention as in **Fig. E.1**. MCNPX simulation (Bertini+Dresner).

# Bibliography


[1] Rubbia C. et al. *A European Roadmap for Developing Accelerator Driven Systems (ADS) for Nuclear Waste Incineration*, ENEA 2001. ISBN 88-8286-008-6 [inrwww.fzk.de/ads-roadmap.html]

[2] Nifenecker H. et al. *Hybrid Nuclear Reactors*, Progress in Particle and Nuclear Physics 43 (1999) 683-827 [http://lpsc.in2p3.fr/gpr/PPNPport/node1.html]

[3] Rutherford E. *Collision of alpha particles with light atoms. III. Nitrogen and oxygen atoms*, Philosophical Magazine 37 (1919) 571-580

[4] Cockcroft J. D., Walton E. T. S. *Experimental with High Velocity Positive Ions - (I) Further Developments in the Method of Obtaining High Velocity Positive Ions*, Proceeding of the Royal Society A 136 (1932) 619-630

[5] Gudowski W. *Acelerator Driven Transmutation Systems - new challenges, new experiments, new instrumentations* [www.sysf.physto.se/instrumentation_seminars/seminars_2004/ presentations/40401_transmutation.pdf]

[6] Bowman C. D. et al. *Nuclear energy generation and waste transmutation using an accelerator-driven intense thermal neutron source*, Nuclear Instruments and Methods in Physics Research A 320 (1992) 336-367

[7] Barber W. C., George W. D. *Neutron Yields from Targets Bombarded by Electrons*, Phys. Rev. 116 (1959) 1551-9

[8] Tatsuhiko S. et al. *Measurement of the neutron spectrum by the irradiation of a 2.04-GeV electron beam into thick targets*, Nuclear Instruments and Methods in Physics Research A 463 (2001) 299-308

[9] Jones S. E. et al. *Experimental Investigation of Muon-Catalyzed d-t Fusion*, Phys. Rev. Lett. 51 (1983) 1757-1760

[10] Mason T. E. et al. *The Spallation Neutron Source: A Powerful Tool for Materials Research*, 33rd ICFA Advanced Beam Dynamics Workshop on High Intensity and High Brightness Hadron Beams. AIP Conference Proceedings, Volume 773 (2005) 21-25

[11] Angelone M., Atzeni S., Rollet S. *Conceptual study of a compact accelerator-driven neutron source for radioisotope production, boron neutron capture therapy and fast neutron therapy*, Nuclear Instruments and Methods in Physics Research A 487 (2002) 585-594

[12] Rossi B. *About properties of penetrating, corpuscular radiation at sea level*, Zeitschrift für Physik 82 (1933) 151

[13] Masarik J., Kim K. J., Reedy R. C. *Numerical simulations of in situ production of terrestrial cosmogenic nuclides*, Nuclear Instruments and Methods in Physics Research B 259 (2007) 642-5

[14] Cunningham B. B. et al., Physical Review 72 (1947) 739

[15] Serber R. *Nuclear Reactions at High Energies*, Physical Review 72 (1947) 1114-5

[16] Harvey B. G. *Spallation*, chapter 3 in Progress in Nuclear Physics, Editor O. R. Frisch, Pergamon Press, volume 7 (1959) 90-120

[17] Zeman J. *Reactor Physics I.*, ČVUT 2003 (in Czech)

[18] Friedlander G. et al. *Nuclear and Radiochemistry*, J. Wiley & Sons, New York 1955

[19] Cugnon J. *Cascade models and particle production: A comparison*, University of Liège preprint ULG-PNT-91-6-G (1991); Particle Production in Highly Excited Matter, NATO Science Series B 303 (1993) 271-293. ISBN 0-306-44413-5

[20] Hołyński R. et al. *Multifragmentation of the Pb Projectile at 158 GeV/nucleon in Pb-Pb interactions*, Multifragmentation - Proceedings of the Int. Workshop XXVII on Gross Properties of Nuclei and Nuclear Excitations. Hirschegg, Austria, January 17-23, 1999. Edited by Feldmeier H et al. GSI Darmstadt (1999) 128-134

[21] Adair R. K. *Nuclear Potential Well Depth*, Phys. Rev. 94 (1954) 737-8

[22] Ledoux X. et al. *Spallation Neutron Production by 0.8, 1.2, and 1.6 GeV Protons on Pb Targets*, Physical Review Letters 82 (1999) 4412-5

[23] Titarenko Yu. E. et al. *Experimental and computer simulation study of the radionuclides produced in thin $^{209}Bi$ targets by 130 MeV and 1.5 GeV proton-induced reactions*, Nuclear Instruments and Methods in Physics Research A 414 (1998) 73-99

[24] Michel R. et al. *Cross sections for the production of residual nuclides by low- and medium-energy protons from the target elements C, N, O, Mg, Al, Si, Ca, Ti, V, Mn, Fe, Co, Ni, Cu, Sr, Y, Zr, Nb, Ba and Au*, Nuclear Instruments and Methods in Physics Research B 129 (1997) 153-193

[25] Enqvist T. et al. *Isotopic yields and kinetic energies of primary residues in 1 A GeV $^{208}Pb$+p reactions*, Nuclear Physics A 686 (2001) 481-524

[26] Geissel H. et al. *The GSI projectile fragment separator (FRS): a versatile magnetic system for relativistic heavy ions*, Nuclear Instruments and Methods in Physics Research B 70 (1992) 286-297

[27] Armbruster P., Benlliure J. *Basic Nuclear Data at High and Intermediate Energy for Accelerator-Driven Systems*, NUPECC – Nuclear Science: Impact, Applications, Interactions [http://www.nupecc.org/iai2001/report/A6.pdf]

[28] Cugnon J., Volant C., Vuillier S. *Nucleon and deuteron induced spallation reactions*, Nuclear Physics A 625 (1997) 729-757

[29] Borne F. et al. *Spallation neutron spectra measurements Part I: Time-of-flight technique*, Nuclear Instruments and Methods in Physics Research A 385 (1997) 339-344

[30] Martinez E. et al. *Spallation neutron spectra measurements Part II: Proton recoil spectrometer*, Nuclear Instruments and Methods in Physics Research A 385 (1997) 345-353

[31] Friedman F. L., Tobocman W. *An Approximate Wave-Mechanical Description of Deuteron Stripping*, Phys. Rev. 92 (1953) 93-100

[32] Liu L. C., Thaler R.M. *Electrodisintegration of the deuteron in nuclear reactions*, Phys. Rev. C 41 (1990) 2940-2

[33] Ridikas D., Mittig W. *Neutron production and energy generation by energetic projectiles: protons or deuterons?*, Nuclear Instruments and Methods in Physics Research A 418 (1998) 449-457

[34] Tolstov K. D. *Aspects of Accelerator Breeding*, JINR Dubna preprint 18-89-778 (in Russian)

[35] Hilscher D. et al. *Neutron production by hadron-induced spallation reactions in thin and thick Pb and U targets from 1 to 5 GeV*, Nuclear Instruments and Methods in Physics Research A 414 (1998) 100-116

[36] Dementyev A. V., Sobolevsky N. M., Stavissky Yu. Ya. *Neutron yield from extended lead target under incident protons of 0.1 to 100 GeV*, Nuclear Instruments and Methods in Physics Research A 374 (1996) 70-72

[37] Wagner V. et al. *Neutron Production in Spallation Reactions*, Report UJF-EXP-96/03 of NPI AS CR PRI in Řež (1996) (in Czech)

[38] Firestone R. B. *Table of Isotopes*, 8th Edition, John Wiley & Sons, New York, 1998

[39] Letourneau A. et al. *Neutron production in bombardments of thin and thick W, Hg, Pb targets by 0.4, 0.8, 1.2, 1.8 and 2.5 GeV protons*, Nuclear Instruments and Methods in Physics Research B 170 (2000) 299-322

[40] Lott B. et al. *Neutron multiplicity distributions for 200 MeV proton, deuteron, and $^4$He-induced spallation reactions in thick Pb targets*, Nuclear Instruments and Methods in Physics Research A 414 (1998) 117-124

[41] Barashenkov V. S., Nucl. Part. Phys. 9 (1978) 781

[42] Vasilkov R. G., Yurevich V. I., Proc. 11th Meeting of Int. Collaboration on Advanced Neutron Sources ICANS- 11 KEK, Tsukuba, Japan, October 22-26, 1990, KEK Report 90-25 vol. 1 (1991) 340

[43] Akopyan A. G., Kolmichkov N. V., Kuzin A. V., Atomn. Energ. 75 (1993) 219

[44] Heilbron J. L., Seidel R. W., Wheaton B. R. *Lawrence and His Laboratory: A Historian's View of the Lawrence Years*, 1996 Web Publication [http://www.lbl.gov/Science-Articles/Research-Review/Magazine/1981/]

[45] Vasilkov R. G. et al., *Neutron Multiplication in Uranium Bombarded by 300-660 MeV Protons*, Atomnaya Energiya 48 (1978) 329-335 (in Russian)

[46] Voronko V. A. et al. *Energy spectra of neutrons generated by relativistic nuclei in extended lead target*, Atomic Energy 71 (1991) 1028-1030

[47] Mukaiyama T. *Omega programme in Japan and ADS development at JAERI*, Proceedings of an Advisory Group meeting held in Taejon, Republic of Korea, 1-4 November 1999

[48] Carminati F. et al. *An energy amplifier for cleaner and inexhaustible nuclear energy production driven by a particle beam accelerator*, CERN report CERN/AT/93-47(ET)

[49] Rubbia C. et al. *Conceptual design of a fast neutron operated high power energy amplifier*, CERN report CERN/AT/95-44 (ET)

[50] Degweker S. B. et al. *The Physics of Accelerator Driven Sub-critical Reactors*, Workshop on physics of accelerator driven sub-critical system for energy and transmutation, University of Rajasthan, India, January 23-25, 2006

[51] Lawrence G. *Transmutation and Energy Production with Power Accelerators* [http://accelconf.web.cern.ch/AccelConf/p95/Articles/fpd/fpd03.pdf]

[52] Borcea C. et al. *Results from the commissioning of the n_TOF spallation neutron source at CERN*, Nuclear Instruments and Methods in Physics Research A 513 (2003) 524-537

[53] Andriamonje S. et al. *Experimental determination of the energy generated in nuclear cascades by a high energy beam*, Physics Letters B 348 (1995) 697-709

[54] Abánades A. et al. *Results from the TARC experiment: spallation neutron phenomenology in lead and neutron-driven nuclear transmutation by adiabatic resonance crossing*, Nuclear Instruments and Methods in Physics Research A 478 (2002) 577-730

[55] Leray S. et al. *Spallation neutron production by 0.8, 1.2, and 1.6 GeV protons on various targets*, Phys. Rev. C 65 (2002) 044621

[56] Billebaud A. et al. *Prompt multiplication factor measurements in subcritical systems: From MUSE experiment to a demonstration ADS*, Progress in Nuclear Energy 49 (2007) 142-160

[57] Rubbia C. *The TRADE Experiment: state of the project and physics of the spallation target*, PHYSOR 2004 Topical Meeting, Chicago, USA, April 25-29 2004

[58] Ciavola G. *The TRASCO High Power Proton Source and its LEBT*, Proceedings of the 2002 LINAC Conference Gyeongju (Rep. of Korea) 18-22 August 2002

[59] Aït Abderrahim H. *MYRRHA: A multipurpose accelerator driven system for research & development*, Nuclear Instruments and Methods in Physics Research A 463 (2001) 487-494

[60] Gentil E. Le et al. *Exclusive measurements on $^{56}Fe+p$ at 1 A Gev with the SPALADIN setup at GSI*, Nuclear Instruments and Methods in Physics Research A 562 (2006) 743-6

[61] Persson C-M. et al. *Analysis of reactivity determination methods in the subcritical experiment Yalina*, Nuclear Instruments and Methods in Physics Research A 554 (2005) 374-383

[62] Leray S. *HINDAS High-Energy Programme: Main conclusions and implications for spallation neutron sources*, Proceedings of the International Workshop on Nuclear Data for the Transmutation of Nuclear Waste. GSI-Darmstadt, Germany, September 1-5, 2003, ISBN 3-00-012276-1

[63] Westmeier W. et al. *Transmutation experiments on $^{129}I$, $^{139}La$ and $^{237}Np$ using the Nuclotron accelerator*, Radiochimica Acta 93 (2005) 65

[64] Wan J. S. et al. *Transmutation of $^{129}I$ and $^{237}Np$ using spallation neutrons produced by 1.5, 3.7 and 7.4 GeV protons*, Nuclear Instruments and Methods in Physics Research A 463 (2001) 634-652

[65] Adam J. et al. *Investigation of cross-sections for the formation of residual nuclei in reactions induced by 660 MeV protons interacting with natural uranium targets*, Proceedings of the International Workshop on Nuclear Data for the Transmutation of Nuclear Waste, GSI-Darmstadt, Germany, September 1-5, 2003, ISBN 3-00-012276-1

[66] Adam J. et al. *Investigation of formation of residual nuclei in reactions induced by 660 MeV protons interacting with the radioactive $^{237}Np$, $^{239}Pu$, $^{129}I$*, Proceedings of the International Conference on Nuclear

Data for Science and Technology - ND 2001, Tsukuba, October 7-12, 2001. Journal of Nuclear Science and Technology (2002) 272-5

[67] Pronskikh V. S. et al. *Study of 660 MeV proton-induced reactions on* $^{129}I$, Intern. Conf. on Nuclear Data for Science and Technology ND 2004, Santa Fe, New Mexico, 26 September - 1 October 2004, AIP conference proceedings 769 (2005) 1047-50

[68] Gustov S. A. et al. *Design Status and Future Research Programme for a Sub-critical Assembly Driven by a Proton Accelerator with Proton Energy 660 MeV for Experiments on Long-lived Fission Products and Minor Actinides Transmutation (SAD)*, 7th Information Exchange Meeting on Actinide and Fission Product Partitioning and Transmutation, 14-16 October 2002, Jeju, Republic of Korea

[69] Shvetsov V. et al. *The Subcritical Assembly in Dubna (SAD)-Part I: Coupling all major components of an Accelerator Driven System (ADS)*, Nuclear Instruments and Methods in Physics Research A 562 (2006) 883-886

Gudowski W. et al. *The Subcritical Assembly in Dubna (SAD)-Part II: Research program for ADS-demo experiment*, Nuclear Instruments and Methods in Physics Research A 562 (2006) 887-891

Barashenkov V. S., *Targets for Accelerator-Driven System SAD*, Pisma v Zhurnal Fizika Elementarnykh Chastits i Atomnogo Yadra 131 (2006) 101104 (in Russian); Physics of Particles and Nuclei Letters 3 (2006) 131133

[70] Krivopustov M. I. et al. *First experiments on transmutation studies of* $^{129}I$ *and* $^{237}Np$ *using relativistic protons of 3.7 GeV*, Journal of Radioanalytical and Nuclear Chemistry 222 (1997) 267-270; JINR Dubna preprint E1-97-59

[71] Krivopustov M. I. et al. *First experiments with a large uranium blanket within the installation "energy plus transmutation" exposed to 1.5 GeV protons*, Kerntechnik 68 (2003) 48-54

[72] Krivopustov M. I. et al. *Investigation of Neutron Spectra and Transmutation of* $^{129}I$, $^{237}Np$ *and Other Nuclides with 1.5 GeV Protons from the Dubna Nuclotron Using the Electronuclear Installation "Energy plus Transmutation"*, JINR Dubna preprint E1-2004-79

[73] Katovský K. et al. *Transmutation of $^{238}Pu$ and $^{239}Pu$ using neutrons produced in target-blanket system "Energy plus Transmutation" bombarded by relativistic protons*, Proceedings of the IYNC2004 conference, Canadian Nuclear Society, 2005

[74] Zhuk I. V. et al. *Investigation of energy-space distribution of neutrons in the lead target and uranium blanket within the installation "Energy plus Transmutation" exposed to 1.5 GeV protons*, JINR Dubna preprint P1-2002-184 (in Russian)

[75] Zhuk I. V. et al. *Determination of spatial and energy distributions of neutrons in experiments on transmutation of radioactive waste using relativistic protons*, Radiation Measurements 31 (1999) 515-520

[76] Zamani M. et al. *Neutron yields from massive lead and uranium targets irradiated with relativistic protons*, Radiation Measurements 40 (2005) 410-414

[77] Chultem D. et al. *Investigation of fast neutron spectra of the installation "Energy plus Transmutation" at the 1.5 GeV proton beam of the Nuclotron*, JINR Dubna preprint P1-2003-59 (in Russian)

[78] Manolopoulou M. et al. *Studies on the response of 3He and 4He proportional counters to monoenergetic fast neutrons*, Nuclear Instruments and Methods in Physics Research A 562 (2006) 371-9

[79] Wagner V., Kugler A., Filip C., Kovář P. *Experimental Study of Neutron Production in Proton Reactions with Heavy Targets*, Proceedings of Experimental Nuclear Physics in Europe Facing the Next Millennium Conference - ENPE99, Seville, Spain, June 21-26 1999

[80] Kugler A., Wagner V., Filip C. *Experimental Study of Neutron Fields Produced in Proton Reactions with Heavy Targets*, Proceedings of the $3^{rd}$ International Conference on Accelerator Driven Transmutation Technologies and Applications - ADTTA'99, Prague (Průhonice), 7 - 11 June, 1999

[81] Henzl V. et al. *Transmutation of $^{129}I$ with High Energy Neutrons Produced in Spallation Reactions Induced by Protons in Massive Target*, Proceedings of the International Conference on Nuclear Data for Science and Technology - ND 2001, Tsukuba, October 7-12, 2001. Journal of Nuclear Science and Technology 2 (2002) 1248-51

[82] Henzl V. et al. *Experimental study of high energy neutrons produced in spallation reactions induced by protons in massive target and transmutation of* $^{129}I$, Contributions of the AccApp/ADTTA'01 meeting in Reno, November 2001

[83] Henzl V. et al. *Study of* $^{129}I$ *Transmutation by High Energy Neutrons Produced in Lead Spallation Target*, Proceedings of the International Workshop on Nuclear Data for the Transmutation of Nuclear Waste GSI-Darmstadt, Germany, September 1-5, 2003, ISBN 3-00-012276-1

[84] Krása A. et al. *Experimental Studies of Spatial Distributions of Neutron Production Around Thick Lead Target Irradiated by 0.9 GeV Protons*, Proceedings of the International Workshop on Nuclear Data for the Transmutation of Nuclear Waste, GSI-Darmstadt, Germany, September 1-5, 2003, ISBN 3-00-012276-1

[85] Krása A. et al. *Neutron Production in Spallation Reactions of 0.9- and 1.5-GeV Protons on a Thick Lead Target - Comparison of Experimental Data and MCNPX Simulations*, International Conference on Nuclear Data for Science and Technology 2004, Santa Fe, New Mexico, 26th September-1st October 2004. AIP Conference Proceedings, Volume 769 (2005) 1555-9

[86] Majerle M. et al. *Experimental Studies of Transmutation of* $^{129}I$ *by Spallation Neutrons using JINR Dubna Phasotron*, in Proceedings of the XVII International Baldin Seminar on High Energies Physics Problem, Dubna, Russia, September 27 - October 2, 2004. Relativistic Nuclear Physics and Quantum Chromodynamics vol. II (2005) 135-140

[87] Wagner V. et al. *Experimental Studies of Spatial Distributions of Neutrons Produced by Set-ups with Thick Lead Target Irradiated by Relativistic Protons*, in Proceedings of the XVII International Baldin Seminar on High Energies Physics Problem, Dubna, Russia, September 27 - October 2, 2004. Relativistic Nuclear Physics and Quantum Chromodynamics vol. II (2005) 111-116

[88] Krása A. et al. *Neutron Production in Spallation Reactions of 0.9 and 1.5 GeV Protons on a Thick Lead Target Comparison between Experimental Data and Monte-Carlo Simulations*, JINR Dubna Preprint E1-2005-46

[89] Majerle M. et al. *MCNPX benchmark tests of neutron production in massive lead target*, Proceedings from International Topical Meeting

on Mathematics and Computation, Supercomputing, Reactor Physics and Nuclear and Biological Applications - M&C 2005, Palais des Papes, Avignon, France, September 12-15, 2005, on CD-ROM, American Nuclear Society, LaGrange Park, IL (2005)

[90] Majerle M. et al. *Experimental studies and simulations of spallation neutron production on a thick lead target*, NPDC 19 – New Trends in Nuclear Physics Applications and Technology. Pavia (Italy) September 5-9, 2005; Journal of Physics: Conference Series 41 (2006) 331-339

[91] Krása A. et al. *Comparison between experimental data and Monte-Carlo simulations of neutron production in spallation reactions of 0.7-1.5 GeV protons on a thick, lead target*, NPDC 19 – New Trends in Nuclear Physics Applications and Technology. Pavia (Italy) September 5-9, 2005; Journal of Physics: Conference Series 41 (2006) 306-314

[92] Wagner V. et al. *The Possibility to Use "Energy plus Transmutation" Setup for Neutron Production and Transport Benchmark Studies*, Workshop on physics of accelerator driven sub-critical system for energy and transmutation, University of Rajasthan, India, 23-25 January 2006; PRAMANA - Journal of Physics 68 (2007) 297-306

[93] Křížek F. et al. *The study of spallation reactions, neutron production and transport in a thick lead target and a uranium blanket during 1.5 GeV proton irradiation*, Czechoslovak Journal of Physics 56 (2006) 243-252

[94] Svoboda O. et al. *Neutron Production in Pb/U Assembly Irradiated by Protons and Deuterons at 0.7–2.52 GeV*, in Proceedings of the International Conference on Nuclear Data for Science and Technology ND2007, Nice, France, 23-27 April 2007, pp. 1197-1200

[95] Majerle M. et al. *MCNPX simulations of the experiments with relativistic protons directed to thick, lead targets*, Nuclear Instruments and Methods in Physics Research A 580 (2007) 110-3

[96] Krása A. et al. *Neutron Emission in the Spallation Reactions of 1 GeV Protons on a Thick, Lead Target Surrounded by a Uranium Blanket*, JINR Dubna Preprint E15-2007-81

[97] Majerle M. et al. *Monte Carlo studies of the Energy plus Transmutation system*, JINR Dubna Preprint E15-2007-82

[98] Svoboda O. *Determination of the neutron distribution in an assembly composed of a lead target and a uranium blanket irradiated by a proton beam with the energy of 0.7 GeV*, Diploma thesis, FNSPE CTU in Prague, Czech Republic (2006) (in Czech)

[99] Křížek F. *The study of spallation reactions, neutron production and transport in the targets that are suitable for neutron production in transmutations*, Diploma thesis, Faculty of Mathematics and Physics, Charles Iniversity in Prague, Czech Republic (2004) (in Czech)

[100] Jungclas H. et al. *A mobile helium-jet transport system for on-line spectroscopy of short-range spallation products*, Nuclear Instruments and Methods 137 (1976) 93-8

[101] Prael R. E., Lichtenstein H. *User Guide to LCS: The LAHET Code System*, LANL report LA-UR-89-3014 (1989)

[102] Briesmeister J. F., Editor. *MCNP – A General Monte Carlo N-Particle Transport Code Version 4B*, LANL report LA-12625-M (1997)

[103] Pelowitz D. B. et al. *MCNPX Users's manual. Version 2.5.0*, LANL report LA-CP-05-0369 (2005)

[104] Hendricks J. S. et al. *MCNPX, VERSION 2.6.C*, LANL report LA-UR-06-7991 (2006)

[105] Ferrari A. et al. *FLUKA: a multi-particle transport code (program version 2005)*, CERN 2005-10 (2005), INFN/ TC_05/11, SLAC-R-773

[106] Radiation Shielding Information Center *HETC Monte Carlo High-Energy Nucleon-Meson Transport Code*, ORNL Report CCC-178 (1977)

[107] Coleman W. A., Armstrong T. W. *The Nucleon-Meson Transport Code NMTC*, ORNL Report 4606 (1970)

[108] Cugnon J., Volant C., Vuillier S. *Improved intranuclear cascade model for nucleon-nucleus interactions*, Nuclear Physics A 620 (1997) 475-509

[109] Dementyev A. V., Sobolevsky N. M. *SHIELD universal Monte Carlo hadron transport code: scope and applications*, Radiation Measurements 30 (1999) 553-557

[110] Barashenkov V. S. *Monte Carlo simulation of ionization and nuclear processes initiated by hadron and ion beams in media*, Computer Physics Communications 126 (2000) 28-31

Barashenkov V. S., *CASCADE/INPE code system*, Atomnaya Energiya 87 (1999) 283-286 (in Russian); Atomic Energy 87 (1999) 742-4

[111] Gudima K. K., Mashnik S. G., Toneev V. D. *Cascade-exciton model of nuclear reactions*, Nuclear Physics A 401 (1983) 329-361

[112] Gudima K. K., Mashnik S. G., Sierk A. J. *User manual for the code LAQGSM*, LANL Report LA-UR-01-6804 (2001)

[113] Furihata S. *Statistical analysis of light fragment production from medium energy proton-induced reactions*, Nuclear Instruments and Methods in Physics Research B 171 (2000) 251-8

[114] Agostinelli S. et al. *GEANT4a simulation toolkit*, Nuclear Instruments and Methods in Physics Research A 506 (2003) 250-303

[115] Niita K. et al. *High-energy particle transport code NMTC/JAM*, Nuclear Instruments and Methods in Physics Research B 184 (2001) 406-420

[116] Azhgirey I. L. et al. *The future development of the MARS program for the electromagnetic cascades simulation in the energy range up to 20 TeV*, IHEP Protvino preprint 93-19 (in Russian)

Azhgirey I. L., Talanov V. V., *MARS program package status*, in: Materials of the 17th Workshop on the Charged Particles Accelerators (RUPAC-2000), vol. 2, Protvino, Russia (2000) 184-7 (in Russian)

[117] Bersillon O. et al. *TIERCE: A code System for particles and Radiation Transport in Thick targets*, in Proceedings of Second Conference on Accelerator-Driven Transmutation Technologies and Applications, 37 June 1996, Kalmar, Sweden (1997) 520-6

[118] Duarte H. *Particle production in nucleon induced reactions above 14 MeV with an intranuclear cascade model*, Physical Review C 75 (2007) 024611

Duarte H. *The nonelastic reaction code BRIEFF and its intranuclear cascade BRIC*, in Proceedings of the International Conference on Nuclear Data for Science and Technology ND2007, Nice, France, 23-27 April 2007

[119] Bielajew A. F. *Fundamentals of the Monte Carlo method for neutral and charged particle transport*, University of Michigan, 2001 [http://www-personal.umich.edu/ bielajew/MCBook/book.pdf]

[120] Waters L. S. et al. *MCNPX Users's manual. Version 2.1.5*, LANL report LA-UR-99-1995 (1999)

[121] Bertini H. W. *Low-Energy Intranuclear Cascade Calculation*, Physical Review 131 (1963) 1801

[122] Yariv Y., Fraenkel Z. *Intranuclear cascade calculation of high energy heavy ion collisions: Effect of interactions between cascade particles*, Phys. Rev. C 24 (1981) 488-494

[123] Boudard A. et al. *Intranuclear cascade model for a comprehensive description of spallation reaction data*, Phys. Rev. C 66 (2002) 044615

[124] Pienkowski L. et al. *Hot nuclei in reactions induced by 475 MeV, 2 GeV* $^1H$ *and 2 GeV* $^3He$, Physics Letters B 336 (1994) 147-151

[125] Trebukhovsky Yu. V. et al. *Double-Differential Cross Sections for the Production of Neutrons from Pb, W, Zr, Cu, and Al Targets Irradiated with 0.8-, 1.0-, and 1.6-GeV Protons*, Yadernaya Fizika 68 (2005) 416 (in Russian); Physics of Atomic Nuclei 68 (2005) 315

[126] Prael R. E., Bozoian M. *Adaptation of the Multistage Pre-equilibrium Model for the Monte Carlo Method (I)*, LANL Report LA-UR-88-3238 (1998)

[127] Gudima K. K., Ososkov G. A., Toneev V. D. *Model for Pre-Equilibrium Decay of Excited Nuclei*, Yad. Fiz. 21 (1975) 260 (in Russian); Sov. J. Nucl. Phys. 21 (1975) 138

Mashnik S. G., Toneev V. D. *MODEXthe Program for Calculation of the Energy Spectra of Particles Emitted in the Reactions of Pre-Equilibrium and Equilibrium Statistical Decays*, JINR Dubna preprint P4-8417 (1974)

[128] Dresner L. *EVAP-A Fortran Program for Calculating the Evaporation of Various Particles from Excited Compound Nuclei*, ORNL Report ORNL-TM-196 (1962)

[129] Junghans A. R. et al. *Projectile-fragment yields as a probe for the collective enhancement in the nuclear level density*, Nuclear Physics A 629 (1998) 635-655

[130] Barish J. et al. *HETFIS High-Energy Nucleon-Meson Transport Code with Fission*, ORNL Report ORNL-TM-7882 (1981)

[131] Atchison F. *Spallation and Fission in Heavy Metal Nuclei under Medium Energy Proton Bombardment*, Meeting on Targets for Neutron Beam Spallation Sources, Kernforschungsanlage Jülich GmbH (1980) 17-46

[132] Chadwick M. B. et al. *Cross-Section Evaluations to 150 MeV for Accelerator-Driven Systems and Implementation in MCNPX*, Nuclear Science and Engineering 131 (1999) 293-328

[133] Koning A. J. et al. *New Nuclear Data Evaluations for Ca, Sc, Fe, Ge, Pb, and Bi Isotopes*, International Conference on Nuclear Data for Science and Technology 2004, Santa Fe, New Mexico, 26th September-1st October 2004. AIP Conference Proceedings, Volume 769 (2005) 422-5

[134] *An Introduction to the ENDF Formats*, LANL report LA-UR-98-1779 (1998) [http://t2.lanl.gov/endf/title.html]

[135] Chadwick M. B. et al. *Physics models and nuclear data evaluations for enhanced Monte-Carlo transport*, LANL report LA-UR-00-3601 (2000)

[136] Fukahori T. *Historical overview of nuclear data evaluation in the intermediate energy region*, International Conference on Nuclear Data for Science and Technology 2004, Santa Fe, New Mexico, 26th September-1st October 2004. AIP Conference Proceedings, Volume 769 (2005) 47-52

[137] Leray S. et al. *Validation of high-energy nuclear models: State-of-the-art and perspectives*, Nuclear Instruments and Methods in Physics Research A 562 (2006) 806-9

[138] van der Meer K. et al. *Spallation yields of neutrons produced in thick lead/bismuth targets by protons at incident energies of 420 and 590 MeV*, Nuclear Instruments and Methods in Physics Research B 217 (2004) 202-220

[139] Ishibashi K. et al. *Measurement of neutron-production double-differential cross sections for nuclear spallation reaction induced by 0.8, 1.5 and 3.0 GeV protons*, Journal of Nuclear Science and Technology 34 (1997) 529-537

[140] Meigo S. et al. *Measurements of neutron spectra produced from a thick lead target bombarded with 0.5- and 1.5-GeV protons*, Nuclear Instruments and Methods in Physics Research A 431 (1999) 521-530

[141] Meigo S. et al. *Measurements of Neutron Spectra Produced from a Thick Tungsten Target Bombarded with 1.1 and 2.3 GeV/c Protons and $\pi^+$ Mesons*, 1999 Symposium on Nuclear Data (JAERI-Conf 2000-005), Nov. 18-19, 1999 at Tokai Establishment of JAERI

[142] Takada H. *Nuclear medium effects in the intranuclear cascade calculation*, Journal of Nuclear Science and Technology 33 (1996) 275-282

[143] Yoshizawa N. et al. *Development of high energy transport code HETC-3STEP applicable to the nuclear reaction with incident energies above 20 MeV*, Journal of Nuclear Science and Technology 32 (1995) 601-7

[144] Koning A. J., Hilaire S., Duijvestijn M. C. *TALYS: Comprehensive Nuclear Reaction Modeling*, International Conference on Nuclear Data for Science and Technology 2004, Santa Fe, New Mexico, 26th September-1st October 2004. AIP Conference Proceedings, Volume 769 (2005) 1154-9

[145] Young P. G., Arthur E. D., Chadwick M. B. *Comprehensive nuclear model calculations: theory and use of the GNASH code*, in Proceedings of the IAEA Workshop on Nuclear Reaction Data and Nuclear Reactors, ICTP Trieste, Italy, April 15May 17, 1996 (World Sci. Publ. Co., Singapore, 1998) 227-404

[146] Broeders C. H. M. et al. *ALICE/ASH - Pre-compound and evaporation model code system for calculation of excitation functions, energy and angular distributions of emitted particles in nuclear reactions at intermediate energies*, Report Forschungszentrum Karlsruhe FZKA 7183 (2006)

[147] Uhl M., Strohmaier B. *Computer code for particle induced activation cross sections and related quantities*, IRK report No. 76/01, Vienna (1976)

[148] Herman M. et all. *EMPIRE: Nuclear Reaction Model Code System for Data Evaluation*, Nuclear Data Sheets 108 (2007) 2655-2715

[149] Han Y. *Calculations and analysis of n + $^{50,52,53,54}$Cr reactions in the $E_{\mathrm{n}} \leq 250$ MeV energy range*, Nuclear Physics A 748 (2005) 75-111

[150] Koning A. J., Hilaire S., Duijvestijn M. C. *TALYS-1.0 A nuclear reaction program*, User manual, December 21, 2007

[151] Broeders C. H. M., Konobeyev A. Yu., Mercatali L. *Global Comparison of TALYS and ALICE Code Calculations and Evaluated Data from ENDF/B, JENDL, FENDL, and JEFF Files with Measured Neutron Induced Reaction Cross-sections at Energies above 0.1 MeV*, Journal of Nuclear and Radiochemical Sciences 7 (2006) pp. N1-N4

[152] K. H. Beckurts, K. Wirtz *Neutron Physics*, Springer-Verlag, New York (1964)

[153] Krivopustov M. I. et al. *About the First Experiment on Investigation of $^{129}I$, $^{237}Np$, $^{238}Pu$, $^{239}Pu$ Transmutation at the Nuclotron 2.52 GeV Deuteron Beam in Neutron Field Generated in U/Pb-Assembly "Energy plus Transmutation"*, JINR Dubna preprint E1-2007-7

[154] Krivopustov M. I. et al. *Investigation of neutron generation and transmutation of $^{129}I$, $^{237}Np$, $^{238}Pu$, $^{239}Pu$ at the experiment using the U/Pb-assembly irradiated with 1.60 GeV deuterons*, JINR Dubna preprint E1-2008-54

[155] Kovalenko A. D. et al., *LHE in Images* [http://lhe.jinr.ru/english/img_01.htm]

[156] Smirnov A. A., Kovalenko A. D. *Nuclotron - Superconducting Nuclei Accelerator at LHE, JINR (Design, Operation and Development)*, Particles and Nuclei, Letters 6 (2004) 11-40 (in Russian)

[157] Vokal S. *Review of experiments on the nuclotron December 2004*, Acta physica slovaca 54 (2004) 493-523

[158] Toneev V. *The NICA/MPD Project at JINR (Dubna)*, Proceeding of the Critical Point and Onset of Deconfinement - 4th International Workshop July 9 - 13, 2007 Darmstadt, Germany, arXiv:0709.1459v2 [nucl-ex]

[159] Berger M. J. et al. *Stopping-Power and Range Tables for Electrons, Protons, and Helium Ions* [http://physics.nist.gov/PhysRefData/Star/Text/contents.html]

[160] Wan J. S. et al. *Monitor Reactions in Al-Foils for High Energy Proton Beams Bombarding a Thick Target*, Nuclear Instruments and Methods in Physics Research B 155 (1999) 110-115

[161] Aleksandrov Yu. V. et al. *(P,X) Reactions Cross Sections in Aluminium at Medium Energy Protons*, Nuclear phenomenology and neural networks - Conference on Nuclear Spectroscopy and Nuclear Structure, Moscow, 1996;

Aleksandrov Yu. V. et al. *Production Cross Section For Radioactive Nuclides In Copper Target Bombarded by 660 MeV Protons*, ibid.;

[162] Michel R. et al. *Nuclide Production by Proton-Induced Reactions On Elements ($6 \leq Z \leq 29$) in the Energy Range from 800 to 2600 MeV*, Nuclear Instruments and Methods in Physics Research B 103 (1995) 183-222

[163] *Experimental Nuclear Reaction Data (EXFOR/CSISRS)* [http://www.nndc.bnl.gov/exfor]

[164] Alfassi Z.B. et al. *Activation Analysis I., II.*, CRC Press 1990. ISBN 0849345839, 0849345847

[165] Audi G. et al. *The NUBASE Evaluation of Nuclear and Decay Properties* Nuclear Physics A 624 (1997) 1-124

[166] Uwamino Y. et al. *Measurement of neutron activation cross sections of energy up to 40 MeV using semimonoenergetic p-Be neutrons*, Nuclear Science and Engineering 111 (1992) 391

[167] Chadwick M. B. et al. *ENDF/B-VII.0: Next Generation Evaluated Nuclear Data Library for Nuclear Science and Technology*, Nuclear Data Sheets 107 (2006) 29313060 [http://www.nndc.bnl.gov/exfor/endf00.htm]

[168] Kim E. et al. *Measurements of Neutron Spallation Cross-Sections of $^{12}C$ and $^{209}Bi$ in the 20- To 150 MeV Energy Range*, Nuclear Science and Engineering 129 (1998) 209

[169] Frána J. *Program DEIMOS32 for gamma–ray spectra evaluation*, Journal of Radioanalytical and Nuclear Chemistry 257 (2003) 583-587

[170] De Corte F. *The k0-standardization method. A move to the optimization of neutron activation analysis*, Ryksuniversiteit Gent: Facultei Van de Wetenschappen 1986

[171] Hubbell J.H., Seltzer S. M. *Tables of X-Ray Mass Attenuation Coefficients and Mass Energy-Absorption Coefficients*, National Institute of Standards and Technology, Gaithersburg, MD (2004) [http://physics.nist.gov/xaamdi]

[172] Hnatowicz V. *Handbook of Nuclear Data for Neutron Activation Analysis. Evaluation of Gamma-Ray Spectra*, Czechoslovak Atomic Energy Commission, Nuclear Information Centre, Prague 1986

[173] Majerle M. et al. *Neutron detection techniques in spallation experiments*, JINR Dubna Preprint, to be published

[174] Dietrich F. S. et al. *Proton reaction cross sections measured in the BNL/AGS E943 experiment*, Proceedings of Accelerator Applications 2000 Conference, Washington, November, 2000 (American Nuclear Society, Lagrange Park, IL), p. 293

[175] Trzaska M. et al. *Excitation of the $\Delta$(1232)-Resonance in Proton-Nucleus Collisions*, Zeitschrift fuer Physik A 340 (1991) 325

[176] Vasilkov R. G. et al., *Neutron yields and thermal neutron fluxes in a lead-water system bombarded by high energy protons*, Atomnaya Energiya 25 (1968) 479

[177] West D., Wood E., Can. J. Phys. 49 (1971) 2061

[178] Fraser J.S. et al., Phys. Canada 21 (1965) 17;

Fraser J.S. et al., in: Proc. Ann. meeting of the Canadian Assoc. of Physicists, Vancouver, 10 June 1965

[179] Zucker M. S. et al. *Spallation Neutron Production Measurements*, Nuclear Science and Engineering 129 (1998) 180-6

[180] Lone M. A. et al. *Total neutron yields from 100 MeV protons on Pb and $^7$Li targets*, Nuclear Instruments and Methods 214 (1983) 333

[181] Ryabov Yu. V., Matushko G. K., Slastnikov V. N. *Measurement of the average neutrons yield from 250 MeV protons absorbed in a lead target*, Zeitschrift für Physik A 311 (1983) 363